Counting statistics of electron transfer in a single quantum dot

Von der Fakultät für Mathematik und Physik
der Gottfried Wilhelm Leibniz Universität Hannover
zur Erlangung des Grades
Doktor der Naturwissenschaften
Dr. rer. nat.
genehmigte Dissertation
von

Nandhavel Sethubalasubramanian

2016

Referent: Prof. Dr. Rolf J. Haug
Korreferent: Prof. Dr. Jürgen König

Tag der Promotion: 14.12.2016

Abstract

Electron transport in nanostructures has been a very active topic of research for over last few decades and is still actively investigated across different materials and very new device types. This research has been fuelled by the necessity to understand microscopic physical phenomena in the transport processes, as the device dimensions continuously decrease. As the device dimensions get very small, quantum mechanical effects tend to dominate electron transport behavior. Quantum dots or single electron transistors are among the smallest possible devices which could be fabricated in the laboratory and using them the transport processes could be finely investigated in controlled conditions of an experimental setup. The inherent quantum mechanical nature of electron transport in these devices gives it less of a deterministic but more of intrinsically probabilistic behavior. This thesis draws on this inspiration to fabricate and investigate single electron transistors as charge transport devices and uses statistics of the probabilistic charge transport to understand the microscopic transport behavior of these devices.

The probabilistic nature of electron transport basically arises through very small currents flowing through the very thin channel barriers, whose resistance could be much larger than the quantum of $h/e^2 \simeq 26$ kΩ (with e being the unit charge and h being the Planck's constant). Using these high-resistance barriers formed across a junction of low capacitance regions in series, offers single electrons to suffer Coulomb blockade due to each electron being able to interact with another electron. In large conductors this interaction is always averaged and the current flow does not carry information of this interaction, while in a very small conductor, this interaction becomes visibly important and this aspect of electron transport allows only single electron to charge or discharge the device at a time, giving rise to switches in the current magnitude as measured capacitively through a quantum point contact.

These current switches carry information on possible electron correlations happening across the channel barrier. We use the tool of full counting statistics to investigate the probability $P(N,t)$ to measure the number N of electrons crossing the barrier in time t. This zero frequency charge correlation statistic is used to estimate the moments and cumulants of the probability distribution. This work in particular makes use of a recent technique of studying factorial cumulants which are studied to provide information about microscopic physical phenomena of Coulomb interactions during the transport process. The factorial cumulants are shown to oscillate as function of time (in our experimental analysis) when the electron correlations are present in the measured current while they do not oscillate when electron interactions had not occurred. We further investigate the distributions of electron waiting-times, when the energetics of the device allow two electron states to be occupied at the quantum dot and we infer whether the waiting times for certain tunneling processes carry memory of interactions from previous state across the tunneling barriers.

Keywords: Factorial cumulants, Electron interactions, Electron correlations

Kurzzusammenfassung

Der Elektronentransport durch Nanostrukturen ist seit mehreren Jahrzehnten ein sehr aktives Forschungsthema und wird auch heute aktiv in einem breiten Materialspektrum untersucht. Diese Forschung wurde angetrieben durch die Notwendigkeit, mikroskopische physikalische Phänomene in den Transportprozessen zu verstehen, da die Systemgrösse elektronischer Bauteile sich kontinuierlich verringert. Werden die Systemabmasse sehr klein, können quantenmechanische Effekte das elektronische Transportverhalten dominieren. Quantenpunkte oder Einzelelektronentransistoren sind kleinstmögliche Systeme, die im Labor hergestellt werden können. Unter Verwendung dieser können diese Transportprozesse in kontrollierten Bedingungen in einem Versuchsaufbau untersucht werden. Durch die inhärente quantenmechanische Natur des Elektronentransports in diesen Systemen ist dieser weniger deterministisch, sondern zeigt vielmehr intrinsisch probabilistisches Verhalten. Im Rahmen dieser Arbeit wurden daher Einzelelektronentransistoren hergestellt und untersucht. Es werden Statistiken des probabilistischen Ladungstransportes verwendet, um das mikroskopische Transportverhalten dieser Systeme zu verstehen.

Die probabilistische Natur des Elektronentransports zeigt sich grundsätzlich in sehr kleinen Strömen, die durch Kanalbarrieren fliessen, deren Widerstand viel grösser als die Widerstands-Quanteneinheit $h/e^2 \simeq 26$ kΩ (mit der Elementarladung e und dem Planckschen Wirkungsquantum h) sein kann. Durch diese Barrieren und dazwischenliegende Bereiche mit geringer Kapazität in serieller Konfiguration erfahren einzelne Elektronen Coulomb-Blockade aufgrund der Wechselwirkung der Elektronen untereinander. Während in grossen ausgedehnten Leitern der Stromfluss aufgrund von Mittelung keine Information bezüglich dieser Wechselwirkung trägt, wird diese in einem sehr kleinen Leiter wichtig und sichtbar. Durch diese Eigenschaft des Elektronentransportes kann das System mit nur jeweils einem einzelnen Elektron geladen oder entladen werden. Die Änderung der Elektronenzahl führt zu sprunghaften Änderungen des Stromes durch einen kapazitiv angekoppelten Quantenpunktkontakt.

Diese Stromänderungen beinhalten Informationen über mögliche Elektronenkorrelationen über die Kanalbarrieren hinweg. Wir verwenden das Werkzeug der Full Counting Statistics, um die Wahrscheinlichkeit $P(N, t)$ zu untersuchen, eine Anzahl von N der Elektronen in der Zeit t zu messen, die die Barriere passieren. Diese zero-frequency Ladungskorrelationsstatistik wird verwendet, um die Momente und Kumulanten der Wahrscheinlichkeitsverteilung abzuschätzen. Insbesondere wird in dieser Arbeit ein aktuelles Verfahren verwendet faktorielle Kumulanten zu untersuchen, um Informationen über mikroskopische physikalische Phänomene hervorgerufen durch Coulomb-Wechselwirkungen während des Transportprozesses zu erhalten. Es wird gezeigt, dass die faktoriellen Kumulanten als Funktion der Zeit oszillieren (in unserer experimentellen Analyse), wenn Elektronenkorrelationen im gemessenen Strom vorhanden sind und nicht oszillieren, wenn keine Wechselwirkungen zwischen den Elektronen stattgefunden haben. Zudem wird die Verteilung der Wartezeiten der Elektronen für den Fall, dass die Besetzung zweier Elektronenzustände des Quantenpunktes energetisch erlaubt ist, untersucht, um zu folgern, ob die Verteilungen Memory-Effekte des zuvor besetzten Zustandes enthalten.

Schlagworte: Factorial kumulanten, Elektron-Wechselwirkung, Elektronenkorrelationen

Contents

List of Figures

Nomenclature

2DEG	2-Dimensional Electron Gas
AC	Active current
AFM	Atomic Force Microscope
BW	Band width
DC	Direct current
DOS	Electronic Density of States
FCS	Full Counting Statistics
GF	Generating Function
LAO	Local anodic oxidation
MBE	Molecular Beam Epitaxy
QD	Quantum Dot
QPC	Quantum Point Contact
SEM	Scanning Electron Microscope
SET	Single electron transistor
α	Asymmetry of tunneling process
$\langle\zeta\rangle$	Average of variable ζ
k_B	Boltzmann's constant
μ_B	Bohr magneton
C	Capacitance

Λ	Characteristic function
μ	Chemical potential
χ	Counting field
z	Counting field of a generating function
C_r	Cumulant of order r
$\langle\langle n^m \rangle\rangle$	Cumulant of order m for total events n
$S(z,t)$	Cumulant generating function, at counting field z and time t
I	Current
ω_c	Cyclotron frequency
$E_n(\overrightarrow{k})$	Dispersion energy for electrons, in the band n
n_m	Electron density of the system m under consideration
E_c	Energy at bottom edge of conduction band
g^*	Effective electron Lànde g-factor
m_e	Effective mass of electron
F_m	Factorial cumulant of order m
F	Fano factor
$f_{L/R}$	Fermi function at Left or Right lead
E_F	Fermi energy
λ_F	Fermi wavelength
ν	Filling factor of Landau levels
Δf	Frequency bandwidth
G	Generating function
$G(z,t)$	Generating function, at counting field z and time t
l_B	Magnetic length

$\overrightarrow{B}$	Magnetic field
τ	Mean Tunneling time interval
M	Moment of function
$\langle n^m \rangle$	Moment of order m for total events n
$\mu_r(x)$	Moment of order r, of variable x
$\overrightarrow{p}$	Momentum operator
I_{amp}	Noise current at the input of amplifier
V_{amp}	Noise voltage at the input of amplifier
C_m	Normal cumulant of order m
N	Number of unit charges, until specified otherwise
h	Planck's constant
U	Potential
$P(N,t)$	Probability of N charges, transferred in time t
$\mathcal{G}$	Quantized conductance
R_{qpc}	Quantized resistance of QPC
m_0	Rest mass of electron
$S(0)$	Shot noise at zero frequency
S_f	Shot noise at finite frequency f
g_s	Spin degeneracy of an electron
T	Temperature of the system
Tr	Transmission probability
R_{xy}	Transverse / Hall resistance
Γ	Tunneling rate
Γ_L	Tunneling rate across the left barrier of quantum dot

Γ_R	Tunneling rate across the right barrier of quantum dot
Γ_D	Tunneling rate at the detector
q	Unit electronic charge
V	Voltage
$W(\tau)$	Waiting time distribution for time τ
$\overrightarrow{k_x}$	Wave vector in direction x

1 Introduction

Development in today's electronics is happening through retrenching of semiconductor devices into nanometer dimensions with newer technologies and applications. The ITRS roadmap into the region of 10nm and below 10nm dimensions does envisage it necessary to understand thoroughly many plaguing physical phenomena of static leakages, quantum tunneling, thermal issues due to dynamic power density that are not just harder to predict and manage but also add to the costs of sustaining the economics of electronics consumption in the long run for the industry.

The quantum mechanical dynamics of the major charge carriers (electrons in further discussion) get paramount importance in the nanoscale dimensions due to the much quantified (small) number of electrons becoming present at these scales in the devices. Fundamental research work in understanding precisely these aspects have resulted in investigation of single-electron devices (transistors) which are also expected to allow us to understand if a quantum-information device for future information processing could also be designed and enabled successfully using the knowledge so gained from the study. Both the wave and particle nature property of electrons are interesting to this end as the wave nature allows probing of the information through resultant wave interferences and particle nature allows transmitting this information in a discrete way to be better inferred and recorded. This thesis, in a similar vein, tries to study time dependent tunneling aspects of electrons in single-electron transistors (or quantum dots) at energy configurations of the electrons, where their behaviors are less random, more controllable (i.e., at conditions of extremely low operating- temperatures and noise at the device) and also allow investigation of microscopic information such as presence or absence of interferences through the analyses of noise patterns evolving as discrete events through the device.

Fabrication of nano devices on high-quality grown crystals of GaAs host material are essential to the understanding of the dynamics of carrier transport through those structured nano devices. Molecular beam epitaxy (MBE)

technique is used to grow high quality crystalline heterostructure which is a sandwich of precisely controlled laid (and band-gap engineered) materials (with similar lattices) on the host material of GaAs, which confine the carriers spatially in a 2-dimension (similar to a single Graphene sheet or an ultra thin metal layer) and therefore affords fabrication of nano-structures on the surfaces (top-clad layer of the heterostructure) to enable further spatial confinement of the carriers through electrostatics, into 1- or 0- dimensions and offering the possibility to control the flow of the charge carriers. The surface nano-structuring is carried through lithography techniques of Atomic-Force Microscopy and Scanning-Electron Microscopy. The surface structures are basically lateral- or metalized top- gates. Application of a potential at these gates, causes an electrostatic confinement of electrons into 1- or 0- dimensions, below the surface along the plane of the 2-dimensional confinement of the engineered heterostructure. These confinements act like electron waveguides and the charges moving through this confinements display a quantized transport behavior which forms the basis of all further investigations.

The devices so created are operated at temperatures of few hundred milli Kelvin to lessen randomness (Brownian motion behavior) of electrons witnessing themselves at higher temperatures (than the cooler operating temperature) with no features of their behavior dynamics (hence showing a white spectral feature) and since electrons tunneling through a confined waveguide have an associated noise pattern to them (and hence a distinct feature), which is called as shot-noise, it is essential to operate the devices (and the electrons moving therein) at energy configurations where this observation gets successful.

Since the study of quantum dynamics entails wave nature of the charge carriers, the length scales though, in the nano dimensions need be such that,

$$l_{\mathrm{es}} \ll l_D \ll l_{\mathrm{dph}} \ll l_{\mathrm{ies}}$$

with l_{es} being the 'elastic scattering length', l_D being the 'device length', l_{dph} being the 'dephasing length' and, l_{ies} the 'inelastic scattering length'.

This makes the carriers ballistic within the lengths of the devices which still being smaller than the 'dephasing or decoherence length' allows any electron-electron interactions to also become part of end observation in an

experiment. Further, the inelastic scattering length which is also the mean length for the carrier to lose its energy to the environment while reaching an equilibrium state, and this energy being k_BT (k_B being the Boltzmann's constant, T being the temperature), it is essential to have a low T as possible and keep the transport a non-equilibrium (or close to equilibrium through a finite bias) phenomena, which allows one to investigate the transport features over a longer time period. The low temperatures also allow ground state occupation of the charge carriers which offers a simplistic noise picture of ground state carriers' transport behavior than also possibly due to the higher energy excitations of the carriers which could also be studied provided the simplistic picture has been thoroughly examined.

This work essentially studies shot-noise behavior of carriers through nano-structured device using single quantum dot (quantum dot being a zero-dimensional confinement of charge carriers with discrete energy states offered through both physical confinement and low temperature) in a single-electron tunneling device configuration and operation. The idea of operating quantum dots in single electron transport configuration is enabled through weakly coupling the single quantum dot with the charge reservoirs. This weak coupling is strictly enabled through keeping the resistance of the coupling channel within few integral multiples of $1/G_Q$ (G_Q being the quantum of conductance). This is also called 'Coulomb blockade' regime, where the integral multiple is possible due to Coulomb force blockade [1] of the next charge, withholding it to pass through the channel since the energy cost of this process needs to be larger than single quantum of $e^2/2C$ energy (C being the capacitance of the dot owing to its geometry and electrostatic configuration with other gates, and this remains nearly constant for the designed structure), which necessarily needs to be larger than any external bias energy and temperature of the charge, wanting to undertake the transport, hence quantizing the whole transport process through the channel.

Study of shot-noise is quite different from the study of an averaged current that is usually measured from an electronic device since, the averaged current is an average over all the microscopic transport events carried out through the device, the microscopic dynamics (of charge transport) gets obscured or perhaps lost in the process. Studying the frequency spectrum of the noise would be a standard way to understand the time evolution of the noise (and has been carried out for some time now [2]), the, process of

correlated transport, electron-electron interactions would not be so evident in the frequency spectral analysis of the charge transport noise. Shot noise studies have been carried to understand sub-Poissonian behavior of single electron tunneling [3] and fractional-charge tunneling [4, 5] in fractional quantum Hall regime.

Probing of noise fluctuation becomes possible through an integrated 'charge detector' which is again a 1-D confined channel capacitively coupled with the quantum dot, which makes it sensitive to any charge fluctuations at the quantum dot, and show up as fluctuation in its own channel current. This fluctuation is read out for charge fluctuations happening at the quantum dot-weakly coupled-reservoir system.

The discussion of the aforementioned different length scales, even through the quantum mechanical approach of investigating charge transport process, inherently makes the whole process less deterministic and more statistical in nature. The statistical analyses essentially captures the fluctuations within charge transport and higher order correlations in the DC frequency limit or finite frequency limit, which are collectively termed into full counting statistics (FCS) [2]. This work focuses on DC frequency limit current correlators of orders going beyond the first two namely the mean current and the noise (through higher order moments and cumulants) by studying the probability distribution $P(N, t)$ of counted N charges, travelling through the 'quantum dot' in time t. Characterizing the origin of the fluctuations, this distribution could be Gaussian or Poisson, whose variance, skewness from the asymmetric tails of the distribution, the sharpness of the center of the distribution and further orders could provide us with distinct information to distinguish the nature of the whole transport process. Further, the FCS follows the idea that the cumulant for the measured transport process is the sum of all the cumulants of the sub-processes which are also independent to each other.

FCS through the calculation of 'factorial' cumulants further offers us to investigate 'discrete' [6, 7] sub-processes that otherwise do not show up in normal cumulants since normal cumulants are worked upon continuous variables or quantities [8]. Factorial cumulants of orders > 1, tend to be zero, for Poisson distribution, and the shift from pure Poisson process becomes evident with non-zero factorial cumulants with orders > 1, while the normal cumulants of orders > 2 are non-zero for Poisson processes and zero for Gaussian processes.

Chapter 2 briefly introduces us to the idea of mesoscopic transport phenomena in semiconductors, takes through shortly to magneto-transport experiment to understand behavior of electrons at magnetic fields and then discusses the idea of full counting statistics and its advantage in understanding charge transport as discrete processes over just measuring the average currents.

Chapter 3 briefly introduces us to the idea of technology of crystal growth, nano fabrication techniques, particularly the fabrication of hybrid nanostructures, the necessity of putting through right processing steps in optical lithography, AFM lithography and SEM lithography. These processing steps also needed to be optimized for efficient and electrically correctly working device. The efficiency parameters were in reducing the number of total steps in getting this done, usage of AFM and SEM tools concurrently to aid in correct hybrid structure and optimizing wet chemical processes to promote very good ohmic contacts. The chapter also discusses the use of Palladium element in the ohmic contact process which was necessary to have a reliable process for getting maximum working ohmic contacts which was not always achievable through the Ge/Ni/Au eutectic process of making ohmic contacts. The chapter further discusses the experimental procedure for the electron counting process.

Chapter 4, discusses the procedural techniques of collecting and analyzing the counting signal corresponding to charge fluctuations through the quantum dot-QPC (quantum point contact) system. The data processing steps which involve converting raw current switching signal into a meaningful waiting time distribution data which then are processed to yield moments and cumulants.

Chapter 5, discusses all the results of applying full counting statistics through normal cumulants and factorial cumulants on the distribution data obtained through counting experiment. The factorial cumulants analysis is discussed in the scheme of non-linear transport where a high-bias is available at the dot offering more than single occupation level for the electron to occupy and the resultant 3-level states due to 2 electron transport (not co-tunneled) through the dot-QPC system. The analyses of 2 occupation state data, through calculation of factorial cumulants provide us with new information on particle interactions which were not possible with the normal cumulants.

Chapter 6, gives the concluding remarks on the current understanding of our experiment and the results, and puts forward further ideas which could be investigated to improve upon and extend the understanding of current results.

Appendices A through D, further offers new and optimized details on lithography techniques, recipes, nano-fabrication errors, ohmic contact issues and, also proposes an idea to improve the signal-to-noise ratio for future counting experiments. Appendix E discusses on understanding and derivation of rates from waiting time distribution. Appendix F discusses further the time evolution of factorial cumulants, in a very high dot bias situation.

2 Theoretical Overview

2.1 Motivation

This chapter briefly discusses the underlying concepts of dynamics of electron transport through nanostructures. The idea of statistical investigation techniques of cumulants on electron transport dynamics that has been employed in this work, would be briefly discussed, which will also be a prologue to the later discussion on Full Counting Statistics in Chapter 5.

2.2 Nano - Mesoscopic systems

Nano-dimensional semiconductor devices permeate every day to day life today. Unlike the classical physics of microscopic transport which guided most device behaviors until the dimensions started to get below few hundreds of nanometers, the necessity for understanding mesoscopic behavior through the quantum mechanical dynamics of charges and atoms in the transport process, has become a very important area of study in the last two decades.

Mesoscopic regime brings in new physical properties which can be vastly different from those of the bulk systems. Mesoscopic regime could ideally be characterized when the length of the device approaches the Fermi wavelength [9] $\lambda_F = h/\sqrt{2m_e E_F}$ where, m_e, E_F are mass of electron and the Fermi energy, of the material system of the device (where then the wave nature of an electron becomes significant). The nomenclature of quantum confinement or size quantization is used to describe the situation when the length scales in the bulk material gets squeezed in either or all of the length dimensions and, the typical lengths where the size quantization occurs, are within few factor multiples of λ_F. In the homogeneous bulk, electrons are free to move in all three directions but while confined to less than three directions, it gives rise to new device characteristics which are put into many useful applications and, as well to understand many other physical phenomena.

The Fermi wavelength discussed before varies with the electron densities in the material system for different dimensions, for spin degeneracy 2, as [9],

$$\lambda_{\mathrm{F}} = \begin{cases} 2^{3/2}\left(\dfrac{\pi}{3n_{3\mathrm{D}}}\right)^{1/3}, \text{for bulk system} \\ \left(\dfrac{2\pi}{n_{2\mathrm{D}}}\right)^{1/2}, \text{for 2D systems} \\ \dfrac{4}{n_{1\mathrm{D}}}, \text{for 1D system} \end{cases} \tag{2.1}$$

with the electron densities, $n_{3\mathrm{D}}$, $n_{2\mathrm{D}}$ and $n_{1\mathrm{D}}$ respectively at corresponding dimensions.

The energy level for a homogeneous solid could be represented as function of wavevector $\overrightarrow{k}$ in all the three dimensions as $E_{\mathrm{subband}}(k_x, k_y, k_z)$. With a z-direction confinement of length L_z (and forming a box), the allowed values of k_z would be $n_z\pi/L_z$ ($n_z = 1, 2, \cdot\cdot$, being the subband index,) [10] and the energy levels would be $E_{\mathrm{subband}}(k_x, k_y, k_z)$ with the restricted k_z values. This pertains to formation of a quantum well with electrons moving only in the x-y plane. Materials can be band-engineered to yield this kind of quantization and they are referred to as 2 dimensional electron gas or a 2DEG system.

For the bulk (3 dimensions) the energy dispersion relation for GaAs material system is highlighted in Fig. 2.1, and obtained from the following relation as [10];

$$E(\overrightarrow{k}) \approx E_{\mathrm{c}} + \frac{\hbar^2(k_x^2 + k_y^2 + k_z^2)}{2m_e} \tag{2.2}$$

where, E_{c} and m_e are constants of band gap and conduction band effective mass respectively.

For a quantum well with quantum confinement in the z-direction we will have, with 1D subbands (labeled as p) and each with 2D dispersion relation as [10],

$$E_p(k_x, k_y) \approx E_c + {n_z}^2\varepsilon_z + \frac{\hbar^2(k_x^2 + k_y^2)}{2m_e} \quad \text{with} \quad \varepsilon_z = \frac{\hbar^2\pi^2}{2m_c L_z^2} \tag{2.3}$$

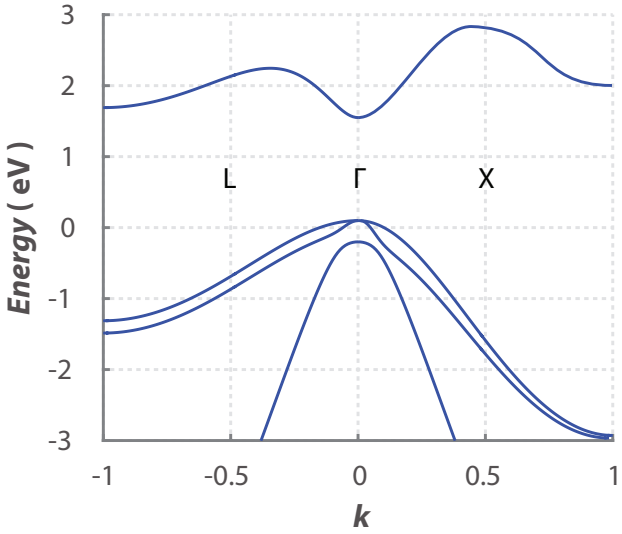

Figure 2.1: Energy dispersion relation curves as 'illustration' for bulk GaAs. Energy calculated is for Conduction band effective mass m_e of $0.12m$ from sp^3s^* model described in [10] and Conduction band edge (band gap) E_c of 1.55eV (at 0 K temperature).

The value ε for discussion, assumes the electrons are confined in an infinite potential of narrow width L_z, and in applying the above idea into the engineering of a 2DEG material system, the value of L_z is very small (narrow) such that for the box confinement to be called as a quantum well, the energy difference (ΔE) from the discrete levels corresponding to k_z is $\ll$ the thermal energy k_BT, with k_B being the Boltzmann constant and, T the temperature. This condition gives a bound state to the electron with a finite potential well and we will see below, the idea is constructed in all the three directions to give discrete energy states for electrons, to occupy and become maneuverable, in a quantum device.

A very small z-confinement (of few nm), for GaAs with m_e of $0.07m_0$ (m_0 being the rest mass of electron) at near absolute zero temperature, would

yield a large energy separation ε_z (of few hundred meV) and shows stronger effects of size quantization, which is highly desirable to study material properties at microscopic level.

Continuing with the above idea, for a quantum wire with quantum confinement in both y, z directions, with 2D subbands and each with 1D dispersion relation, we will have,

$$E_{q,p}(k_x) \approx E_c + {n_y}^2\varepsilon_y + {n_z}^2\varepsilon_z + \frac{\hbar^2 k_x^2}{2m_e} \quad \text{with} \quad \varepsilon_y = \frac{\hbar^2\pi^2}{2m_c L_y^2} \tag{2.4}$$

where n_y and n_z are the subband indices (positive integers $1, 2, \cdot\cdot$). For a system confined in all three directions, we will have a system like an atom, called a quantum dot, with,

$$E_{j,q,p} = E_{n_x,n_y,n_z} \approx E_c + \frac{{n_x}^2\hbar^2\pi^2}{2m_c L_x^2} + \frac{{n_y}^2\hbar^2\pi^2}{2m_c L_y^2} + \frac{{n_z}^2\hbar^2\pi^2}{2m_c L_z^2} \tag{2.5}$$

The energy $E(\overrightarrow{k})$ quantization through subbands is experimentally observable through the quantity of density of states which measures the energy eigenstates per unit volume of the confinement in any of the three dimensions of the energy range. If $E(\overrightarrow{k}) = E_c + (\hbar^2 k^2)/(2m_e)$ is the parabolic energy dispersion relation with effective mass m_e, the density of state (DOS) is obtained as,

$$D(E) = \frac{d(\text{total states with energy} \leq E)}{dE} \tag{2.6}$$

and we obtain the different DOS values for the different confinement situations as [10–12];

$$D(E)_{3\text{D}} = [L_x L_y L_z]\left[\frac{m_e}{2\pi^2\hbar^3}\right][2m_e(E - E_{\text{c}})]^{1/2} \tag{2.7}$$

$$D(E)_{2\text{D}} = [L_x L_y]\left[\frac{m_e}{2\pi\hbar^2}\right] \tag{2.8}$$

where, for the 2D situation, the $D(E)$ rises abruptly and becomes constant for higher energy values, and additional steps are observed for further 2D subbands at higher energies.

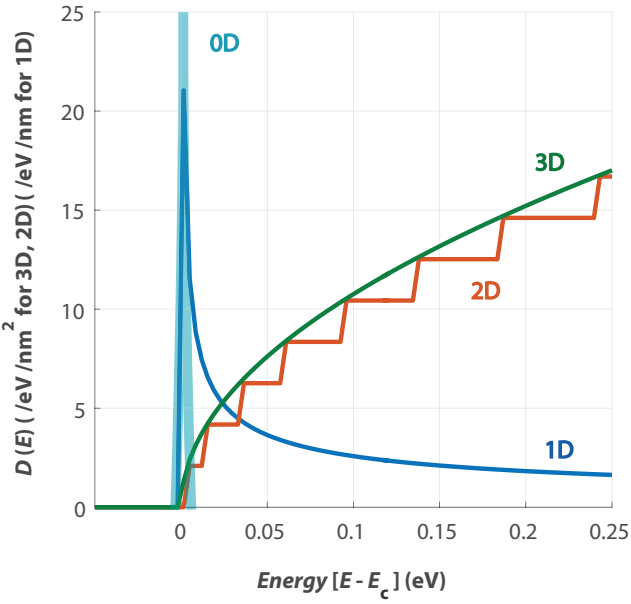

Figure 2.2: DOS calculated for 3D, 2D (confined along z direction), 1D (confined along y, z direction) cases using equations 2.7 - 2.10, with 0D case superimposed for illustration. For calculation, x, y, z lengths were respectively 1, 1, and 10 nm [10].

$$D(E)_{1\mathrm{D}} = [L][\frac{m_e}{\pi\hbar}]\left[\frac{1}{2m_e(E-E_\mathrm{c})}\right]^{1/2} \tag{2.9}$$

$$D(E)_{0\mathrm{D}} = 2\delta(E-E_\mathrm{c}) \tag{2.10}$$

while for 0D situation, the DOS is the discrete Dirac function at each subband where E_c is due to carriers confined from all three dimensions in the conduction-band and the states are just available at these discrete energies with no k-space around, while a pre-factor of 2 is accounted for spin degeneracy. For 3D, 2D and 1D respectively, we see the density of

states, dependence varies as $E^{1/2}$, E^0 and $E^{-1/2}$ respectively. The DOS for different size quantization are highlighted in Fig. 2.2.

While the observable quantity in a device, the conductance, is dependent on DOS as discussed above, the number of subbands (or modes) are another factor in studying the conductance of nanostructures. This idea of 'number of mode' becomes relevant when the device dimensions are smaller or similar to the mean free path of the electrons. In understanding the 1D channel which are also called as Quantum Point Contacts (QPCs), which form an essential role in the nano devices we fabricate, we would briefly look into the idea of modes as another foundational principle in quantum transport.

If we look into the current through a quantum wire (from energy dispersion relation of Eq.2.4), we have current I defined as [10],

$$I = -q \int \frac{dk_x}{2\pi} \frac{1}{\hbar} \frac{\partial E_\nu(k_x)}{\partial k_x} = \frac{-q}{h} \int dE_\nu \tag{2.11}$$

We see the current to be quantized in q/h for unit energy E_ν, for a particular subband or mode ν. For a two-terminal quantum wire, with the left and the right sides being at chemical potentials of μ_1 and μ_2 respectively, the current for the first mode ν would then be,

$$I = \frac{-q}{h}(\mu_1 - \mu_2) = \frac{q^2}{h} \cdot V \tag{2.12}$$

with V therefore being the potential difference between the two ends.

Figure 2.3 illustrates the development of quantized conductance profile with energy, with the unit quantization being q^2/h. Chemical potential is the equilibrium state between the higher energy DOS of occupied and lower energy DOS of unoccupied states. This definition is very useful for temperatures > 0 in the Fermi-Dirac distribution (since at T $= 0$, $\mu = E_f$) and will be regularly referred in discussions in the thesis. The discussion on number of modes would again be discussed further in the chapter.

2.2.1 Magnetic effects in 2D mesoscopic systems

This section briefly discusses 2D mesoscopic systems under influence of magnetic fields of comparatively weaker (for extracting electron density and

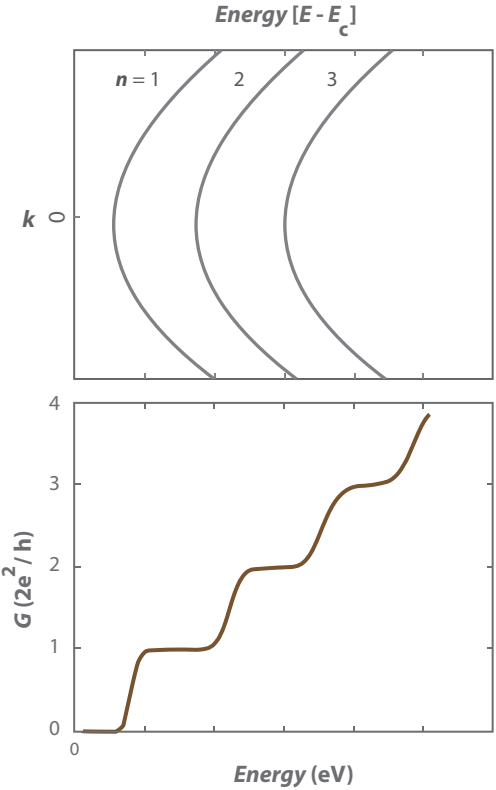

Figure 2.3: Saddle shape schematic of quantized conductance $\mathcal{G}$ as a function of mode density (number of subbands) taking part in a transport process. The top graph illustrates the energy dispersion for the lowest conduction-band subbands.

infer quality of fabricated samples) and stronger (for a further theoretical overview) field strengths.

We would briefly look into non-relativistic Dirac equation to understand electrons under influence of external magnetic field. In the solid, though the electron velocities are not high, the electrons suffer weak relativistic effects from the electric fields at the nuclei (and the dispersion relation for

this relativistic electrons, take the form $E^2(\overrightarrow{k}) = {m_0}^2c^4 + c^2\hbar^2k^2)$. With a non-relativistic lowest-order approximation, the presence of magnetic field $\overrightarrow{B}$ yields the Pauli equation as ([10]),

$$(E - m_0c^2)\psi = \left[\phi + \frac{(\overrightarrow{p} + q\overrightarrow{A})^2}{2m}\right][\hat{\mathbf{1}}]\psi + \mu_B \overrightarrow{\sigma} \cdot \overrightarrow{B}\psi \tag{2.13}$$

where, $\overrightarrow{p}$ is the momentum operator, $\mu_B = q\hbar/2m$ is the Bohr magneton, $\overrightarrow{B} = \overrightarrow{\nabla} \times \overrightarrow{A}$ ($\overrightarrow{A}$ being the vector potential) and, the second term on the right hand side being the Zeeman term, ϕ the scalar electric potential, $\hat{\mathbf{1}}$ the identity matrix and, σ the Pauli spin matrices.

The electrons quantized in the z-direction under external magnetic field in perpendicular to the $x - y$ plane direction, take up cyclotron orbits which is referred to as Landau quantization. The second term from Eq. 2.13, could be mapped into a harmonic oscillator as

$$\omega \rightarrow \omega_c = \frac{eB}{m} \tag{2.14}$$

which yields the cyclotron frequency ω_c and taking spin degeneracy into the picture, we obtain for the $x - y$ plane, the energy eigenvalue as,

$$E_n = \hbar\omega_c\Big(n - \frac{1}{2}\Big) + g^*\mu_B B,\, n\, =\, 1, 2, \cdot\cdot \tag{2.15}$$

with, g^* being the effective electron Lànde g-factor. The state E_n forms the nth Landau level. The Landau level degeneracy per unit area per energy level is therefore given as,

$$D(E) = \frac{g^*}{2\pi l_B^2}[\delta(E - E_n)] \tag{2.16}$$

where, $l_B = \sqrt{\hbar/eB}$ is the magnetic length which corresponds to the extent of the quantizing magnetic field. Figure 2.4 illustrates the DOS for Landau quantized 2DEG system.

The energy spectrum of electron transport through a 2DEG, under an external perpendicular magnetic field, would display quantum Hall effect as shown in Fig. 2.5. From the figure, the Hall voltage which is inversely proportional to the electron density ($R_{xy} = B/(n_e \cdot e)$, with n_e being the electron density and, R_{xy} being the Hall resistance), is measured and the

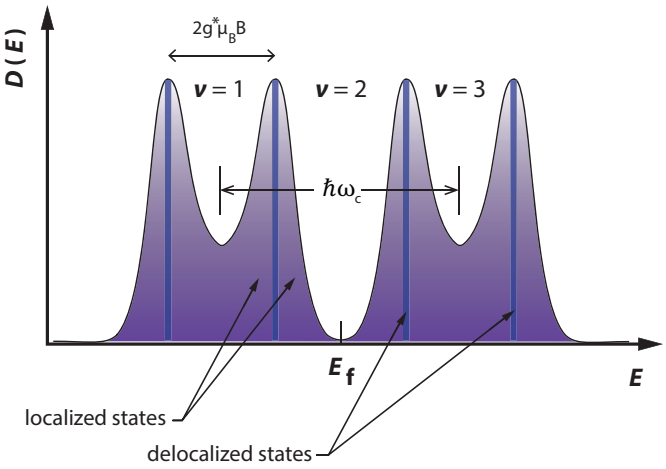

Figure 2.4: Illustration of DOS with spin degeneracy lifted (in strong magnetic field) for each Landau level. The δ function for the energy is broadened at the bottom from the non-ideal situation of conduction-band fluctuations.

mobility ($\vartheta \propto 1/(R_{xx} \cdot e \cdot n_e)$) of electrons are determined. Mobility values give a good indication into the quality of our samples. A comparatively higher mobility value indicates samples with low impurities and scatterers at the 2DEG space.

The measurement of Fig. 2.5 was done with an increasing longitudinal (x-direction) voltage at liquid He temperature (4K). At this temperature, the onset of Hall plateau visibly starts at considerable higher magnetic field ($\approx$ 3T) due to larger thermal fluctuations. The Hall voltage plateaus, show a certain constant Hall resistance values of h/ne^2 with the factor $1/n$ signifying Hall resistance quantization with the fully filled Landau level n.

The quantized quantum Hall measurements ([13]) also suggest that localized states (Fig. 2.4) which are predominantly due to disorder and impurities, do not contribute to Hall resistance.

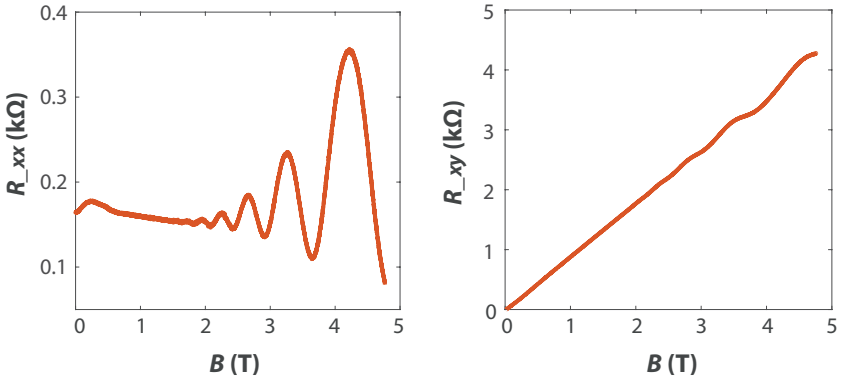

Figure 2.5: Longitudinal (R_{xx}) and Hall (R_{xy}) resistances measured using a hall bar at 4.2 K temperature, to study the quality (electron density and mobility) of the fabricated heterostructure sample discussed in Chapter 3. The Hall bar used in the measurement is illustrated in Fig. 2.6.

The Landau levels at the Fermi energy are usually partially occupied and this degree of filling (filling factor) of Landau levels is given as (for spin degeneracy of $g_s = 2$)[[9]],

$$\nu = \frac{g_s E_F}{\hbar\omega_c} \equiv \frac{hn_e}{eB} \tag{2.17}$$

As the magnetic field increases, energies of Landau levels change with their position within the boundary plane of the Hall device (actual case of real devices with finite dimensions). At the boundary edges, the Landau levels cross Fermi energy and it has been shown through self-consistent calculations [14] that, the delocalized states form compressible metallic-like conducting strips while the localized states form incompressible strips which are non-conducting (a very simplistic picture though, since tunneling through incompressible strips and fractional quantum Hall effects are outside the purview of this thesis). The number of these strips are proportional to the number of fully occupied Landau levels from the inside of the planar boundary of the device. The metallic-like strips form the edge channels where the partially filled Landau levels always get redistributed with electrons

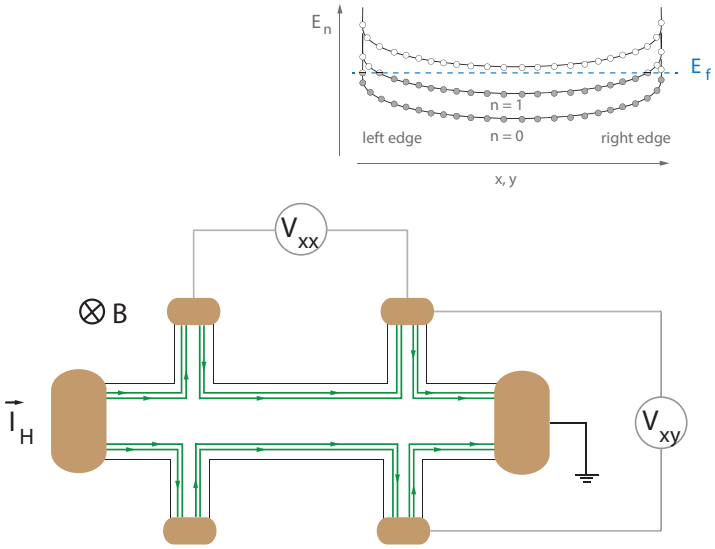

Figure 2.6: Hall measurement through 2DEG. The Hall resistance is obtained from V_{xy} measurement while driving a current I through the x direction. The fully occupied Landau levels form the edge channels (close to the device boundary shown in green). The inset shows the fully and partially occupied Landau levels from the inside of the $x-y$ plane of the sample, rise in energy at the edges of the sample boundary, giving rise to metallic-like channels at the edges for the electron transport, at higher magnetic fields.

and get pinned to the Fermi energy. At $k_BT \ll \hbar\omega_c$ (with electron thermal energy much less than the Landau separation), the electrons in the edge channels scatter elastically and the channel gets ballistic (one dimensional) in nature [15, 16]. The oscillations in the longitudinal resistance R_{xx} (Fig. 2.5), called as Schubnikov-de Haas oscillations are the result of Fermi level pinning in between the Landau levels, with bulk becoming non-conducting (rising the resistance). The transverse (Hall) resistance R_{xy} plateaus are the quantized transverse Hall conductance of value $\nu e^2/h$ (defined in Eq. 2.17). As the ballistic nature of transport makes the electrons to follow the

direction of higher to lower potential (as shown through directed green lines in Fig. 2.6), the current gets directly related to the transmission probability $Tr_{jk}(B)$ of 1D channels [16] with, the current injected into the kth Landau level from the left reservoir being transmitted as a fraction as,

$$I = \frac{e}{h} \sum_{j=1}^{j=M} T_{jk}[\mu_{\text{left}} - \mu_{\text{right}}] \tag{2.18}$$

where, $\mu_{\text{left}} - \mu_{\text{right}} = eV$. We would further have the total transmission probability being summed over all incident channels as,

$$Tr = \sum_{j=1,k=1}^{j=M,k=N} Tr_{jk} \tag{2.19}$$

with, M being the total DOS at the contacts and N being the number of edge states ($M \gg N$). Equation 2.18 (using Eq. 2.19) could hence be approximated to yield a Hall resistance value which is always $(1/T)(h/e^2)$. The factor here denoted by the transmission probability is another point of view of looking at the quantization process explained above.

2.3 Quantum Dots and Electron Transport

Extending the confinement in all the three directions, forming a quasi 0 D density of state system, a 2DEG space could be converted into an island like pool of electrons. The dimensions of this island in each direction are within few multiples of the Fermi wavelength length. This configuration mimics that of an atom and hence this pool of electrons is also referred to as an 'artificial atom' or a quantum dot. The confinement while possible through band-engineering of materials, 2DEGs (where the z-confinement is already achieved through band engineering, to yield electron movement only in the $x-y$ plane) are used along with lateral/top gates, to electrostatically isolate regions of interest in the $x-y$ plane and at the same time create electrostatically-tunable barriers in the $x-y$ plane.

Figure 2.7 highlights the formation of a quantum dot in a 2DEG. The S and D are the electron reservoirs (Source and Drain) connected to the quantum dot through lateral barriers which can allow tunneling or flooding of electrons between the dot and the reservoirs through electrostatic-tuning

of the barrier gates (schematically in the figure, the tuning influences the width of the channel between the dot and the reservoir). In a typical device (with quantum dot) operation, the lateral barriers are tuned to couple the reservoirs weakly (the barrier being less wide) with the dot and this leads to countable number of electrons transiting across the barrier. The scale of this weak coupling is in the orders of few tens of micro electron Volts (across each barrier). The figure also shows an additional gate V_g, which is purely capacitively coupled to the dot through a Schottky barrier. This barrier in effect allows tuning of the energy levels on the quantum dot through capacitive coupling of V_g potential with that of the quantum dot. This tuning is essential in bringing in available energy states in the quantum dot within the electrochemical potential difference of the two reservoirs, so as to enable controlled transport of electrons across the quantum dot.

Electrons are hence added or removed through the quantum dot by a careful tuning of both the lateral barriers along with the capacitively coupled gate in a simple two-terminal device as shown in the schematic of Fig. 2.7. Earlier experiments [17] has shown atom like properties of quantum dots with the energies, needed to add electrons into a dot revealing a shell like structure for a two-dimensional harmonic potential. This is in spite of quantum dots being much larger than real individual atoms. In subsequent sections we will explore the dynamics and the effects of these discrete states effecting through electron transport through the quantum dot.

2.3.1 Electrostatic picture of quantum dot

Transport of electrons across the barrier introduces Coulomb interactions between electrons in the dot and the reservoirs and this introduces different charge dynamics of which the phenomena of Coulomb blockade is further discussed in this section. From Fig. 2.7, the quantum dot forms a 2-terminal device with the source and drain tunnel junctions and a capacitively coupled gate voltage V_{g}, and this device could be aptly called a single-electron transistor (SET). Electrostatically the tunneling barrier are represented with capacitances of C_{s} and C_{d} respectively.

From the equivalent circuit model of the SET, we can theorize the quantum dot potential due to the whole device to be,

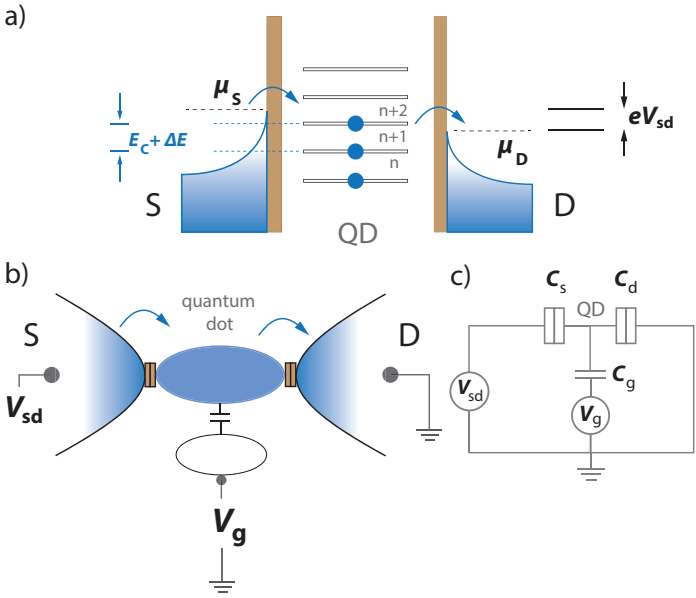

Figure 2.7: (a-b) Quantum dot (QD) schematic in a simple two-terminal device, the 0-D confinement is achieved through the use of S (Source, at electrochemical potential μ_S) and D (Drain, at electrochemical potential μ_D) electrostatic barriers (ohmically connected to electron reservoirs) laterally on the 2DEG. V_g is another lateral gate which is capacitively connected to the quantum dot and provides to tune the energy levels in the quantum dot with reference to the electrochemical potentials of the lateral gates (S and D); Fig. (a) illustrates the discrete energy states at the QD, available within the potential difference of eV_{sd} provided by the source and drain contacts; Fig. (b) schematize the electrical model of the SET circuit, with the quantum dot connected in series with the different gates; while Fig. (c) represents an equivalent circuit model of the SET device.

$$U_{\text{dot}} = U_N + \sum_{j}^{k} \frac{C_j}{C} V_j \tag{2.20}$$

where, U_N is the actual dot potential due to Ne charges and C the dot's capacitance owing to its geometry and that due to all other junctions (or leads) at the dot, with C_j and V_j are the capacitances and voltages at the junction j. The energy at the quantum dot with N number of charges, can therefore be defined as,

$$E(N, N_{(\text{at junctions and gates})}) = \int_{0}^{Ne} U_{\text{dot}}(q)dq = \frac{(Ne)^2}{2C} + (Ne)\sum_{j}^{k} \frac{C_j}{C} V_j \tag{2.21}$$

If we consider the electrochemical potential energy difference required to add an extra electron into the quantum dot, we would need to derive the Eq. 2.21 with respect to N (from classical thermodynamics). The effective energy therefore to put an additional electron into the SET device could be further approximated as [1],

$$E(N, N_{\text{g}}) = \frac{e^2}{2(C_{\text{s}} + C_{\text{d}} + C_{\text{g}})}(N - N_{\text{g}})^2 \tag{2.22}$$

where, N is the existing total number of electrons in the quantum dot, and $N_{\text{g}} = (C_{\text{g}}V_{\text{g}})/e$ is the number of electrons at the quantum dot, due to the influence of actual V_{g}, the gates controlling the capacitive and the tunnel junctions. The factor $E_{\text{C}} = e^2/2C_{\Sigma}$ with $C_{\Sigma} = C_{\text{s}} + C_{\text{d}} + C_{\text{g}}$, is the magnitude of charging energy that would take to alter the electronic state of the quantum dot (only) by an unit quantity (electron) for a given N and N_g.

Since a tunnel junction is characterized by its conductance or resistance, for the correct operation of the SET, it is necessary that, $E_{\text{C}} \gg k_B T$ (i.e., the thermal energy of an electron needs to be much lower than the charging energy and hence the SET is operated at very low temperature T), where k_B is the Boltzman's constant and, the tunnel conductance $\mathcal{G}_{\text{t}}$ is $\mathcal{G}_{\text{t}} \gg 1/R_{\text{t}} = 2(e^2)/h$, providing sufficient transmittance to the single electron either from the dot or the reservoir at the leads through the junction. The

factor 2 is due to spin degeneracy. The tunneling time scale at the junction would be, $\Delta t = R_{\mathrm{t}}C$ (C being the dot's capacitance) [1] which is obtained through Heisenberg's uncertainty relation of, $\Delta E \Delta t = E_{\mathrm{C}} R_{\mathrm{t}} C \gg \hbar$. The quantization of conductance which is conserved in the short and narrow constriction of the tunnel junction were first observed in GaAlAs-GaAs heterostructures [18, 19]. Equation 2.12 could therefore be generalised for N channels as,

$$I = \frac{q^2}{h} \cdot N \cdot V \tag{2.23}$$

where, $V = (\mu_{\mathrm{s}} - \mu_{\mathrm{d}})/q$, $N = k_{\mathrm{F}} \cdot (\text{width of the junction})/\pi$, which happens when the Fermi energy E_{F} ($E_F = \hbar^2 k_{\mathrm{F}}^2 / 2m^*$, m^* being the effective electron mass) at the tunnel barrier is overcome as the width of the junction is increased allowing increase in N. This quantized conductance happening through the tunnel junction could be recalled from Fig. 2.3. The conductance steps in the figure, show a smoother evolution as the channel is opened up through leveraging the gate voltage. This smoothness is a quantum mechanical dependence on the continuous function of energy. This dependence is given by the Landauer formula

$$I = \frac{\mathcal{G}_{\mathrm{Q}}}{e} \sum\nolimits_n \int\limits_{E \to \mu} dE T_n(E)[f_{\mathrm{L}}(E) - f_{\mathrm{R}}(E)] \tag{2.24}$$

where, $f_{\mathrm{L,\,R}}(E)$ is the Fermi function for the left and right side of the junction and $\mathcal{G}_{\mathrm{Q}} = 2e^2/(2\pi)\hbar$ being the quantized conductance value (the subscripts of $\mathcal{G}_{\mathrm{T}}$ and $\mathcal{G}_{\mathrm{Q}}$ ideally give the same idea but used differently to denote different nomenclature within the context of discussion). This is the quantized quantum of conductance flowing through the channel. The rest of the expression (without the $\mathcal{G}_{\mathrm{Q}}$) form the so called modes (with T_n being the quantity to identify the total number of modes), which in very simple terms forms the channel number, and this increases with the channel width, as the channel gets more subbands and so more energy levels for the charges to occupy. This channel number is also highlighted in Fig. 2.3 as a multiple of the quantized value $\mathcal{G}$.

The charging energy is however a classical quantity in nature which since is $\propto 1/C$ can have a vanishing value for a larger dot area signifying a larger capacitance. However, the charging energy is also influenced by the dynamics of electron-electron interactions, screening and correlation

effects across the tunnel junctions and hence offers an additional quantum mechanical dimension into the transport phenomena. An approach called as 'constant interaction model', allows one to explain the experimental data in better detail than the model described above. It would be necessary to include the discrete energy level spacing, which gets well defined for the quantum dot as a function of the dot's geometry, along with the capacitance model. The spin degeneracy resolved discrete single particle level spacing at the dot, can be obtained from the 2DEG DOS definition of $m^*/\pi\hbar^2$ states per unit dot's area A, and is given as,

$$\Delta E \approx \frac{\pi\hbar^2}{m^* A} \tag{2.25}$$

For the constant interaction (CI) model, the single particle discrete states also depend on the magnetic field $\overrightarrow{B}$ as $E(\overrightarrow{B})$, which depend on the characteristic confinement potential (the external gate voltages here). As long as the interaction energies between particles are much smaller than the confinement energy (case of very low magnetic fields, B < 1T), the CI model is successfully used [1, 20]. At higher magnetic fields, the idea of singlet-triplet transitions for multiple electron occupied situations in the quantum dot, with the Darwin-Fock (DF) energy definition is utilized, where the non-constant Coulomb interactions are well described. For a quantum dot in a parabolic confinement of $V(r) = 1/2(m^*\omega_0^2 r^2)$ [21–23], the DF energy spectrum is given as,

$$E_{n,l,s} = (2n + |l| + 1)\hbar\Omega - \frac{1}{2}l\hbar\omega_c + sg^*\mu_B B \tag{2.26}$$

$$\text{with, } \Omega = \sqrt{\omega_0^2 + \frac{1}{4}\omega_c^2}$$

n, is the radial quantum number

$l = -n, -n+2, \cdot\cdot, n-2, n$; is the angular momentum number

$$s = \pm\frac{1}{2}$$

$\omega_c = eB/m^*$, is the cyclotron frequency, $\quad m^* = 0.0067m_0$

The DF spectrum evolves with distinctly spaced levels from zero magnetic field, into a complicated level crossings at higher magnetic fields. At higher

magnetic fields this happens as the electrostatic confinement reduces and levels coalesce with the free electron Landau levels with constant quantum number $n + (\mid l \mid - l)/2$ [23] (the effects angular momentum quantum number playing dominant part, due to its large values, and hence large energy values).

2.3.2 Transport through a quantum dot

Figure 2.8 shows the influence of charging energy on electron transport through the quantum dot. This way of depicting is the practice to infer various parameters affecting electron transport through the dot. As the coupling between the dot and the leads through the tunnel junction gets weaker, Coulomb blockade sets in where, owing to Coulomb repulsion, the energy state occupation within the dot stays constant till the occupied state gets empty again. This is highlighted in the region of 1 and 2 in the schematic of the figure. The actual electrochemical potential needed to add an electron in the $n+1$ state would be that at the n state plus $E_{\mathrm{C}} + \Delta E$. When this additional energy is below the electrochemical potential of the left lead μ_L, it ideally implies the top state in the dot is occupied and a Coulomb blockade prevails across the left lead, while if this energy is still larger than the electrochemical potential of the right lead μ_R, the electron in the top occupied state, in the quantum dot jumps into the right lead. Across the vertical axis in the figure, for the incrementing charge states of N, $N+1$ and so on, being energetically degenerate, we observe electron occupation at the quantum dot, switch between N and $N+1$ and thereby causing a current flow through the quantum dot. The case of $V_{sd} = 0$ is highlighted to show how change of electron number by 1 and not any more due to Coulomb blockade, causes current flow while V_G is increased slowly.

From Fig. 2.8 the plot (a) shows the points of degeneracy for electrons in the quantum dot and as well the regions of Coulomb blockade (white region) within the diamond structure. The diagram also shows the evolution of the parabolic energy states of Eq. 2.22, where the points of crossings are the degenerate points of electrons (encircled in orange) which are energetically degenerate on the vertical axis while the occupation degeneracy increases on the horizontal axis (on either side of 0 V_{sd}). The colored regions adjacent to white region, appropriately suggest the regions of gate and source-drain potentials where the energetics or the occupation degeneracy stays stable (otherwise a Coulomb blockade region) in the quantum dot; with N being

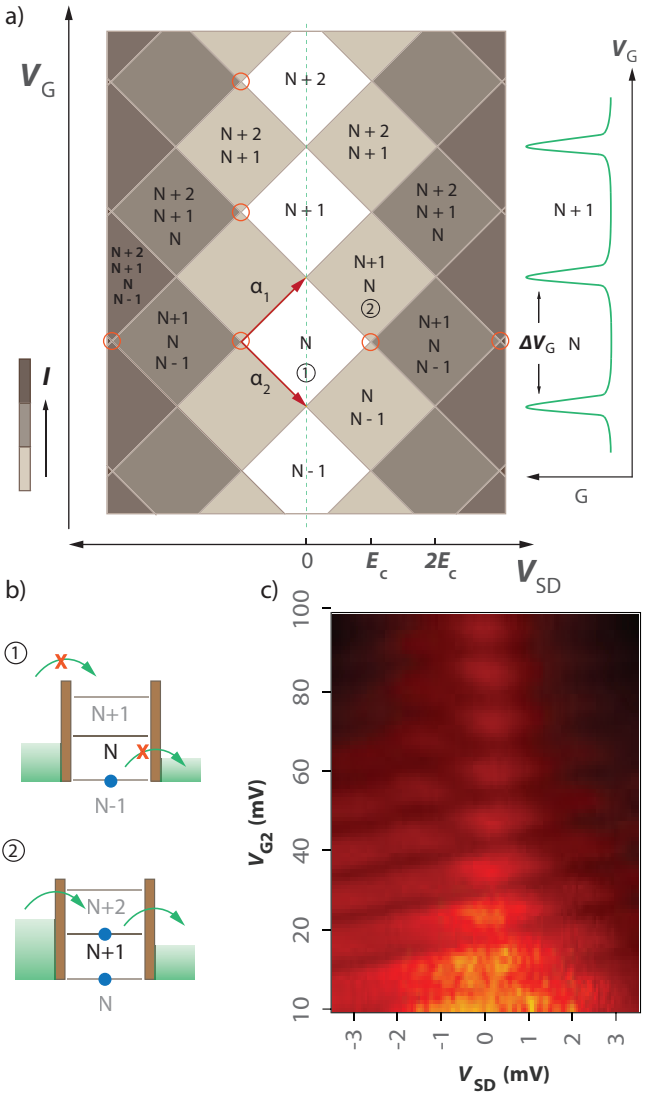

Figure 2.8: Schema of charge stability regions shown in terms of differential-conductance, measurable at the quantum dot for given gate voltage and source-drain biases. Plot (a) schematizes the actual experimental measurement shown in plot (c). See text for further explanation.

the actual number of electrons in the dot. Plot (b) from the figure highlights schematically the Coulomb blockade and tunneling process happening at the respective positions. Plot (c) shows the charge stability diagram from actual measurements from the SET device discussed in this thesis (the 'black' lines are regions of high current ($\sim$ nA) and regions of 'red' / 'yellow spots' are Coulomb blockade regions though still experimentally detectable very-negligible current ($\sim$ few hundred pA) flows through the device).

The transport henceforth occurs, while there is a coupling of filled energetic states in both of the reservoirs (through the tunnel junction) with the empty state of the quantum dot. For a two terminal device of Fig. 2.7, continuing from the electrostatics picture, when there is a coupling between E_N state at the dot, with 'source' reservoir (transport happening in the direction of source to drain), Eq. 2.22 and the equivalent circuit model (from Fig. 2.7) could be inferred to give,

$$E_N + \frac{e}{C_\Sigma}(C_\mathrm{G}\, V_\mathrm{G} + C_\mathrm{S}\, V_\mathrm{SD}) = \mu_\mathrm{D} + eV_\mathrm{SD} \tag{2.27}$$

yielding,

$$\begin{aligned} V_\mathrm{G} &= \frac{C_\Sigma - C_\mathrm{S}}{C_\mathrm{G}} V_\mathrm{SD} + \frac{C_\Sigma}{eC_\mathrm{G}}(\mu_\mathrm{D} - E_N); \\ \alpha_1 &= \frac{C_\Sigma - C_\mathrm{S}}{C_\mathrm{G}} \quad \text{as the positive slope of } (\partial V_\mathrm{G}/\partial V_\mathrm{SD}); \\ \alpha_2 &= -\frac{C_\mathrm{S}}{C_\mathrm{G}} \quad \text{as the negative slope of } (\partial V_\mathrm{G}/\partial V_\mathrm{SD}), \\ &\text{while the drain is in resonance with the } E_N \text{ state} \end{aligned} \tag{2.28}$$

and the slopes yield the ratio of the 'gate' capacitance $C_G = e/V_G$ and the 'total' capacitance C_Σ as $(\alpha_1 - \alpha_2) = C_\Sigma/C_G$, which is also one of the inferable quantities through plotting the figure of Fig. 2.8. The slopes become characteristic of the junctions involved in the transport. The idea of involvement of multiple level occupation states during transport which is shown in dark brown region of Fig. 2.8, would be further discussed in the context of high source-drain bias situation in Chapter 5.

At higher temperatures or bias voltages the lowest excited state with energy spacing of $\simeq \Delta E$ from the ground states also comes in the probable occupation states for the electron to occupy in the transport process through the

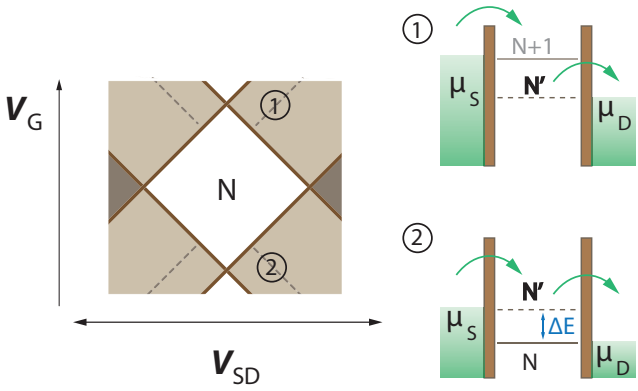

Figure 2.9: Excited state spectroscopy schematic of tunneling process through the quantum dot. In relation to charge stability diagram of Fig. 2.8, the dotted lines in this figure, show the first excited state transport spectrum, which the electrons can occupy, in addition to the ground state represented as 'solid' line. (1) Shows the first excited state (N') at the dot in resonance with the electrochemical potential of the Drain; (2) shows the first excited state at the dot in resonance with the electrochemical potential of the Source.

dot. This gives rise to a non-linear transport spectrum where the differential conductance peak spectrum also show adjacent slope formation as shown in dotted lines of Fig. 2.9. The dotted lines are less prominent in the transport spectrum compared to the ground state lines. The availability of this excited state in the transport window, also gives rise to the possibility of co-tunneling through the dot, though inelastically while the dot is at non-zero bias situation. Since the dot is coupled to the reservoirs and the environment (non-adiabatically), the excited states also have a finite lifetime τ_Γ and owing to this, the discreteness of the excited state spectrum gets broadened by $\simeq \hbar/\tau_\Gamma$ and gives a possibility of excited state continuum with energy $\simeq \Delta E \ln(\Delta E \tau_\Gamma/\hbar)$ [2].

Considering N charges at a given moment of time at the quantum dot, the probability for an electron transfer to occur in a unit time is given by the

rate $\Gamma(N)$ from/to the given state N which could classically be represented as [2],

$$\begin{aligned}\Gamma &= \frac{I}{q} \\ &= \frac{q\mathcal{G}V}{q^2} \\ &\equiv \frac{\mathcal{G}}{e^2}\int dE f(E)(1-f(E-\Delta E)) \\ &= \frac{\mathcal{G}}{e^2}\frac{\Delta E}{\exp\left(\Delta E/k_B T\right)-1}\end{aligned} \tag{2.29}$$

with the tunneling time being $\Delta t = 1/\Gamma$, while this equation also explains the rate at finite temperature.

Since this rate brings a certain probability for an electron to transfer in unit time, which is not a constant value, owing to reasons of dot occupation, dot-reservoir coupling, finite temperature, and conductance quantization; we have here a certain probabilistic dynamics into the transport process. For the dot then, the probability change per unit time would be obtained as [2],

$$\begin{aligned}\frac{dp(N,t)}{dt} = \\ -(\Gamma_F(N)+\Gamma_T(N))p(N,t)+ \\ \Gamma_F(N-1)p(N-1,t)+\Gamma_T(N+1)p(N+1,t)\end{aligned} \tag{2.30}$$

where, Γ_{F} and Γ_{T} are the rates from 'outgoing' and 'incoming' electron from/to the dot, from both directions (reservoirs). The rates remain constant for a given 'dot' and 'gate' voltages.

The above equation forms the Master equation for the probability distribution of the single electron transport. A stationary solution could be obtained for this equation by setting $dp/dt = 0$ and the condition of the probability of being in all possible states $\Sigma N p(N) = 1$. Generalizing the above form quantum mechanically, for any charge state of the dot, if $\Gamma_{(\alpha,\beta)}$ be the rate respectively from initial state α to final state β, then from Fermi Golden

rule definition of rate between an initial state to a final state, we would have,

$$\frac{dp(\alpha)}{dt} = -\sum\nolimits_{\beta} \Gamma_{\alpha\to\beta} p(\alpha) + \sum\nolimits_{\beta} \Gamma_{\beta\to\alpha} p(\beta) \tag{2.31}$$

where, the first group on the right-hand side, signifies the average 'outgoing' current $I_{\text{out-going}}$ from the dot, and the second group, the average 'incoming' current $I_{\text{in-coming}}$ into the dot. The transport is therefore influenced by the straightforward changes in the probability distribution $p(N,(\alpha,\beta))$. If there are no fluctuations in the states, while many states are involved in the transport process, for an energy difference of ΔE, δ_s level spacing energy, we will have $\Delta E \delta_s$ discrete states involved in the transport process which would then yield an average rate,

$$\langle \Gamma \rangle = \frac{\mathcal{G}}{e^2} \delta_s \tag{2.32}$$

2.4 Statistical analysis of transport phenomena

2.4.1 Averaged current

The average flow of electrons $\langle q \rangle$ that cross the tunnel junction from dot into the reservoir during the time Δt could be identified, as an average current $\langle I \rangle$ ($\langle q \rangle = \langle I \rangle \Delta t$) which has been the most primary measurable quantity at any device. In this section we will briefly observe how this quantity is not totally sufficient to study transport at energetics much smaller than the thermal energy at the small dimensions. Study of electron flow in a non-averaging measurement process would rather be more informative to get to know any microscopic dynamics better than purely an averaged measurement process yielding the current. For a brief moment, if we can imagine electrons participating in the averaged current, being countable individually (and so being determinable in a non-averaging measurable way) over the period of the same time Δt, we would have a picture of their distribution over this time period as shown in Fig. 2.10 which schematizes how this process also generates certain statistical information just from the probabilistic nature of the transport, as discussed from Eq. 2.29. We shall see how this statistical picture evolves with the measurement parameters that are experimentally possible.

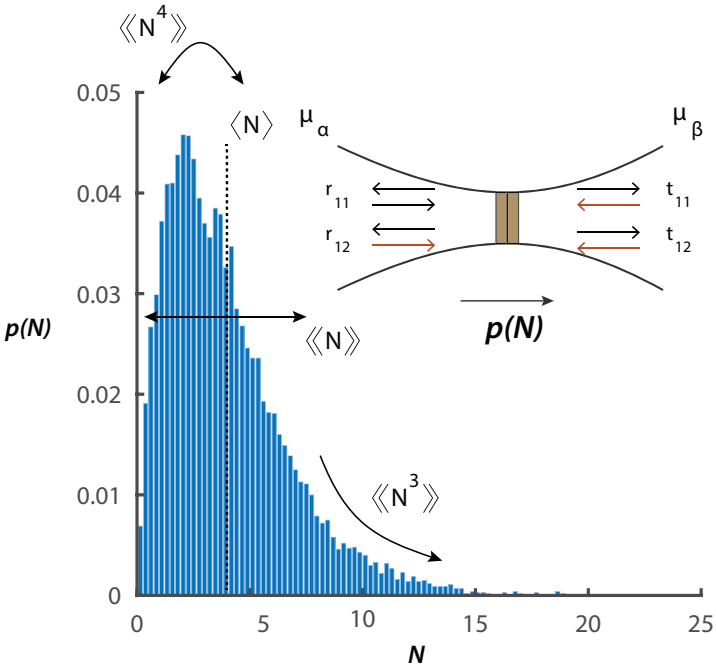

Figure 2.10: Counting statistic of a random event with 10000 total counts, with the degree of freedom (mean) equalling 4 and, a non-symmetric tail at either side of the mean. The y-axis shows the frequency or the distribution of the total events in a short interval of Δt, also suggesting a mean count of 4 within this short interval. The first four cumulants are also schematized (for the 3rd cumulant, the arrow figuratively means the behavior of the tail on both sides). The inset shows a two terminal, simple waveguide with a tunnel junction connecting two reservoirs at the ends (at potentials μ_α and μ_β, α and β being the corresponding reservoirs). The junction is also the scattering region for the electronic wave functions from either side, with reflection r and transmission t amplitudes of individual wave functions schematised for two channels, while also suggesting that, both the reflection and transmission is happening at the first channel from the left side.

We shall look at the averaged current through the collective mechanism of individual transiting electrons using one or more channels at the junction and this methodology would also help us to pick and understand the microscopic (non-averaging) information easily as we go on to discuss noise and higher order statistics later in the section. Considering this way, the electron transport across a junction could be identified with a waveguide picture, but, the real fabricated devices are far from an ideal waveguide picture and studying electron transport through this system would be quite inaccurate.

To enable a better understanding, an approach of using 'scatterers' at the junction (a non-ideal waveguide) allows one, to formulate all the elastic scattering phenomena happening at the junction, given that, the junction is at very low temperature and the scatterers are quantized entities. A scattering matrix approach [24–29], offers the possibility of deriving the currents using the Landauer-Büttiker formalism with the transport described by transmission eigenvalues derived from the scattering matrix. In this formalism the interactions follow fermionic statistics which forbid double occupation of Fermi wave functions in the same state. For a brief theoretical treatment, the average current is taken as [2],

$$\begin{aligned}\langle I\rangle &= 2e\Sigma_n \int_0^{\inf} \frac{dk_x}{2\pi} v_x(k_x)(1-R_n(E))[f_\alpha(E)-f_\beta(E)] \\ &= \frac{e}{\pi}\int_0^{\inf} dE \mathrm{Tr}[tt'][f_\alpha(E)-f_\beta(E)] \end{aligned} \tag{2.33}$$

where, $R_n(E) = \Sigma_n \mid r_{nn'} \mid^2$ is the reflection probability for the wave function getting reflected from all channels n' into channel n. v_x is the velocity of the wave function, with k_x being the wave vector for any transport channel n at energy E_n defined as $k_x = \sqrt{2m^*(E-E_n)/\hbar}$. The transmission probability is given as $\mathrm{Tr}[tt'] = \Sigma_n(tt')$ where t is the transmission matrix responsible for the transmission through the scattering region (reflection and transmission is schematized in Fig. 2.9). The trace of this matrix gives the transmission eigenvalues whose sum can be denoted as T_p. Evaluating the transmission eigenvalues over the Fermi sphere (summing up over all transmission probabilities) at low temperatures, yields the conductance value of [2],

$$\mathcal{G} = 2_s \frac{e^2}{(2\pi)\hbar} \sum_p T_p(\mu) \tag{2.34}$$

$$\text{or } \langle I \rangle = \frac{\mathcal{G}_\mathcal{Q}}{e} \sum_p \int dE T_p(E)[f_\alpha(E) - f_\beta(E)]$$

which is the Landauer formula [30] also discussed earlier in the context of quantized conductance in Eq. 2.24. For a wave function at the scattering region (junction) given by the potential,

$$V(x,y) = V_0 - \frac{1}{2}m^*\omega_x^2 x^2 + \frac{1}{2}m^*\omega_y^2 y^2 \tag{2.35}$$

with V_0 being the electrostatic potential at the junction, the transmission probability is expressed as [31],

$$Tr_p = \frac{1}{1 + e^{(-\pi\varepsilon_n)}} \tag{2.36}$$

with,

$$\varepsilon_n = \frac{2[E - \hbar\omega_y(n + \frac{1}{2}) - V_0]}{\hbar\omega_x} \tag{2.37}$$

for $n = 0, 1, 2, \cdots$. When $\varepsilon_n = 0$ the transmission probability Tr_p approaches value 1. Tr_p yields the stepped conductance of Fig. 2.3 wherein, the width of the transition junction is given by $\hbar\omega_x$ and the separation of the steps is given by $\hbar\omega_y$ and well defined steps occur when $\omega_y \geq \omega_x$. The expression in Eqs. 2.33, 2.34, helps to understand the averaged current in terms of transmission possibility at the junction and integrable over energy.

2.4.2 Shot Noise in preference to averaged current

Since we have now got the expression of the average current through the junction, we have a similar situation in an experimental setup, wherein the measured current is in fact an averaged value over a long period of time. This averaged current does not always give enough information on the many processes that get profound at mesoscopic, ballistic transport and low temperature scales. An electron transfer at a junction is a stochastic process (since we now know the scattering process across channels at the junction as

the dominant reason for this stochastic process) and the number of electrons traversing through the junction at a time Δt is a random phenomena. The study of this stochastic process can however yield much more information than the averaged current alone.

At higher energies the stochastic nature of transport arises from the unavoidable temporal fluctuation or noise which Schottky described across a vacuum diode as an irregular 'pattern' whose mean-squared current value was determined as [32, 33],

$$\langle I^2 \rangle_{\Delta f} = 2eI\Delta f = S_f \Delta f \tag{2.38}$$

where, Δf is the frequency range of probing the current from the diode; $S_f = 2eI$ is the 'white' spectral density or the 'shot noise'. "The noise is the signal" [34] informed that this noise could be used as an additional information other than the measurable averaged current, about the transport process. The contributions towards noise comes from two distinct processes [35]; first, the occupation probabilities of the reservoirs fluctuates with the slightest temperature fluctuations, known as the 'thermal noise' and second the discreteness or the 'granularity' discussed by Schottky which is called the 'shot noise' or in certain ways also the 'partition noise' in parlance relevant to our discussion of single junctions or barriers. The shot noise, has a flat power spectrum at lower frequencies, while the noise increases linearly with current (for large bias voltage $eV \gg k_B T$) [36]. Thermal noise is one, which is always from the occupation probability fluctuations between F occupied Fermi state and $1 - F$, the unoccupied Fermi states, and the fluctuations behave like $\langle (n - \langle n \rangle)^2 \rangle$ with, n being the occupation number in the occupied Fermi state. Thermal noise however reduces to the minimum experimentally possible as $T \to 0$. Partition noise is accounted by the fact that the particle nature of the electrons allows them to get either reflected or transmitted through the junction (or barrier) and hence the random fluctuations in the path partitioning in itself creates this noise behavior. Partition noise is however present even at zero K temperatures.

In semiconductors, the granular nature of electronic behavior (not strictly in the 'particle' sense) can arise through the electron-hole pair creation and annihilation [36, 37], and fluctuating the charge number while giving a Lorentzian whose spectral density is like,

$$S_f \propto \frac{\tau}{1 + f^2\tau^2} \tag{2.39}$$

with τ being the time constant between detection of each charge (electron). This Lorentzian also behaves as,

$$S_f \to \frac{1}{f} \tag{2.40}$$

at low frequencies (close to single digit values in Hz), which is appropriately called $1/f$ noise. If the measurement process is done at higher frequencies, the $1/f$ component ideally vanishes and what is left is what is described in Eq. 2.38, referred to as the shot noise. In classical system the shot noise is not observable due to the self averaging [38, 39] of independent current fluctuations where the suppression is of the order of l_{in}/L ($l_{in} \ll L \gg l_{el}$) where l_{in} is the inelastic mean free path, l_{el} is the elastic mean free path and L is the sample length. In mesoscopic systems however, $L < l_{in}$ (case of ballistic transport), and the shot noise gets profound. In diffusive mesoscopic systems, shot noise is predicted to be $(1/3)^{\text{rd}}$ of value suggested in Eq. 2.38 [39] and in ballistic case, for $L < l_{el}$ the shot noise can still vanish if the transmittance at the junction is unity.

In a fermionic system, the Pauli principle allowing at most an electron in a wave packet, the electron flow through a junction gets regulated through certain minimal overlap of wave packets (or tight packing) and the shot noise can get highly reduced [35, 40–42]. This reduction however is not visible in the averaged current if that is the only measurable quantity in a device. The idea of noise hence takes further importance to study any quantum nature of electronic interactions, which could be better studied through noise correlation studies for example in an interferometer like device. Mesoscopic Mach-Zehnder type interferometric experiments [43–45] have investigated via shot noise measurements, origins of phenomena like 'dephasing' from sensitive measurements in quantum Hall effect regime through single edge state and closed geometry transport. The averaged current values could not yield that information.

From Eq. 2.38, the time $\Delta\tau$ is distributed as a Poissonian (discussed further below), and hence gives the measure of the shot noise as purely from uncorrelated events. The current and spectral density are here equivalent. However, if the junction [18, 19] has a transmittance of unity (due to all

occupied channels), the shot noise for temperature $k_BT \ll eV_{sd}$ and energy independent transmission probabilities Tr_p's, would ideally be [28, 41, 46],

$$S_{f=0} = 2\frac{e^2}{h}|eV_{sd}|\sum_{p=1}^{N} Tr_p(1 - Tr_p) \tag{2.41}$$

Here if, $I_p = (2e^2/h)V_{sd}Tr_p$ is the current at the pth channel, a suppression of $1 - Tr_p$ happens in the shot noise, relative to the classical case from Eq. 2.38. Hence, at junctions where the presence of gate voltages can vary T_p, the shot noise (indicating the correlations of electrons due to Fermi statistics), will change with the maximum due to the top most channel having a transmission probability of 1/2. For a stationary process, at a finite frequency $f > 0$ the shot noise as a correlation function, takes the expression as [35, 47],

$$\mathbf{S}_f = \frac{1}{2}\int \mathrm{d}t\, e^{ift}\langle \Delta\hat{I}_\alpha(\tau)\Delta\hat{I}_\beta(0) + \Delta\hat{I}_\beta(0)\Delta\hat{I}_\alpha(\tau)\rangle \tag{2.42}$$

where, α, β are the corresponding reservoirs as shown in Fig. 2.10; operator $\Delta\hat{I}_\alpha(\tau)$ is defined as $\Delta\hat{I}_\alpha(\tau) - \langle\Delta\hat{I}_\alpha\rangle$. The diagonal elements in Eq. 2.42 are the noise spectral values and the non-diagonal elements correspond to current-current correlators between the reservoirs. At the reservoirs in equilibrium [38], the noise is primarily from an energy range of width of order k_BT at the Fermi level which subsequently gives rise to a current of $eK_BT/\pi\hbar$ from the reservoir. For the case of transmission $\sum T_p \ll 1$, Eq. 2.38 will yield shot noise, for current from either reservoir in a single channel, as,

$$S_f = 2e\frac{ek_BT}{\pi\hbar}\sum_p T_p\Delta f \tag{2.43}$$

and for the case of currents from both reservoirs, and evaluating expression for $\mathcal{G}$ from Eq. 2.34, we will further have,

$$S_f = 4k_BT\mathcal{G}\Delta f \tag{2.44}$$

(with $\mathcal{G}$ being e^2/h), is also known as the Thermal equilibrium noise or the Nyquist-Johnson noise. In a transport (reservoirs not anymore in equilibrium), the conductance and shot noise would be sum of separate contributions of Eq. 2.43 for each channel (with transmission being as, $\sum T_p \ll 1$)

which is ideally, $2k_BT\mathcal{G}$. Eq. 2.44 also shows that the conductance information is an equivalent to shot noise information in a measurement but then, it also does not provide any further information.

2.4.3 Fano factor

The definition of $S = 2e\langle I\rangle$ as discussed from Eq. 2.38, is also known as Poisson value of shot noise. This actually corresponds to Schottky's observation of uncorrelated arrival of charges with a distribution function of time intervals between arrival times of subsequent charges as,

$$P(\Delta t) = \frac{1}{\tau} e^{\frac{-\Delta t}{\tau}} \tag{2.45}$$

with, τ being the mean time interval between the charges. The Poissonian character becomes relevant when T_p is neither 0 or 1. As discussed earlier, Eq. 2.41 corresponds to $S = 2e\langle I\rangle$ in the limit of very low transparency $T_p \ll 1$. As we consider a non-interacting system, the shot noise is always suppressed within the limit of $S = 2e\langle I\rangle$. We note here that, at $T_p = 0$ i.e, for all closed channels and, $T_p = 1$ at all open channels, none contribute to shot noise, while, the maximal contribution is from channels with $T_p = 1/2$. The suppression of shot noise, or the measure of sub-Poissonian shot noise is called the Fano factor and is the ratio of Eq. 2.41 to $S = 2e\langle I\rangle$ (the actual shot noise to the Poissonian noise) which in a linear regime yields [35],

$$F = \frac{\sum_p T_p(1 - T_p)}{\sum_p T_p} \tag{2.46}$$

while, F takes values between zero (indicating all transparent channels) to value of 1 (Poissonian noise) or > 1 (for super-Poissonian noise). This short introduction on Fano factor is elaborated further in the next section.

2.4.4 Higher Order Statistics

For, N events observed in a given measurement, the probability function $P(N)$ of the distribution of those events could be quantified, by getting a measurement M repeated to $M_{\text{max.}}$ identically '$max.$' times, while taking M_N as the count at one measurement; we would then have a perfect count N, as $M_N/M_{\text{max.}}$. Considering this idea from an experiment of stationary

independent repeated set of N event of Fig. 2.10, we get an average count value of

$$\langle N \rangle = \sum_N NP(N) \tag{2.47}$$

and the variance which measures the amount of deviation from the average value, which also is the second cumulant as,

$$\langle\langle N^2 \rangle\rangle = \langle (N - \langle N \rangle)^2 \rangle = \sum_N N^2 P(N) - (\sum_N NP(N))^2 \tag{2.48}$$

From above, if $P(N)$ notes the probability for N counts, and $P(N-M)$ notes the probability for non N counts from the total of $max.$ counts in a given time, the probability of $P_N^{max.}$ can always be found by the convolution of the probabilities of $P(N)$ and $P(N-M)$. For mathematical convenience an expression of 'characteristic function' of the probability distribution could be utilised, which is expressed as [2],

$$\Lambda(\chi) = \sum_N P(N) e^{(i\,\chi\,N)} \tag{2.49}$$

Theoretically the logarithm of the characteristic function (of the counting field χ) also implies a sum over all transport channels, further suggesting that electron transfers in different channels and over different energy intervals are independent in nature [48]. Hence, the characteristic function allows to further process it mathematically to yield different quantities. The total probability distribution will then have a characteristic function of $\Lambda_{max.} = \Lambda_N(\chi)\Lambda_{N-M}(\chi)$ (the product of characteristic function of each event, with $\ln\Lambda(\chi)$ proportional to the duration of the measurement $\mathrm{d}t$). Differentiating '$\ln\Lambda(\chi)$', one time, twice, and further k times with respect to $i\chi$, while setting $\chi = 0$, will give the average, the variance, the kth cumulant of the distribution respectively.

If Γ is the rate of electron transfer through the junction, the probability of transferring an electron during a time $\mathrm{d}t$ would be $\Gamma \mathrm{d}t \ll 1$. The probability of no electron transfer would likewise be, $1-\Gamma \mathrm{d}t$. The characteristic function for a short interval would then be [2],

$$\Lambda_{dt}(\chi) = (1 - \Gamma \mathrm{d}t) + (\Gamma \mathrm{d}t) \exp(i\chi) \tag{2.50}$$

For a certain time Δt comprising of say j short intervals $\mathrm{d}t$, the characteristic function would be simply product of each short interval characteristic function (also that the transfer is non-interacting, and independent from each other short interval). The average number of transferred electrons would be given by $\langle N \rangle = \Gamma t$. Therefore the probability $P(k)$ for k electrons to get transferred through the junction during the time Δt would then be the inverse Fourier transform of the total product characteristic function [2] and is given as,

$$P(k) = \frac{\langle N \rangle^k}{k!} \mathrm{e}^{(-\langle N \rangle \Delta t)} \tag{2.51}$$

This equation is the Poisson distribution. Figures 2.11, 2.12 highlight an example of Poisson process where the $\langle N \rangle$ increases in an experiment for a same total count of electron transfers. The above discussed cases were clearly for $T_p \ll 1$ for one channel. From Fig. 2.12, the data lengths for plot B and C were taken to be 12 ms and 18 ms respectively. The data length is the total length of time the individual counts were measured. As the delta increases, we also see the average waiting time increases, highlighting the idea the more long time events are also counted. Very importantly the tails in the log form, show visibly the variations between the two distributions (discrete vs. continuous) and this idea is characterized in the discussion of factorial cumulants.

On the contrary, for transmission, $0 < T_p < 1$, we expect correlation (and therefore a non-fluctuating current through the junction), which for multi channel, finite temperature, will have a characteristic function as given by Levitov formula [2],

$$\ln \Lambda(\chi) = 2\Delta t \int \frac{\mathrm{d}E}{2\pi\hbar} \sum_p \ln \Big[1 + T_p(\mathrm{e}^{(i\chi)} - 1) f_L(E)[1 - f_R(E)] + T_p(\mathrm{e}^{(-i\chi)} - 1) f_R(E)[1 - f_L(E)] \Big] \tag{2.52}$$

where, f_L and f_R are the fermi distributions on left and right reservoirs. The logarithm since being a integral over energy, suggests electrons are transferred independently in each energy interval.

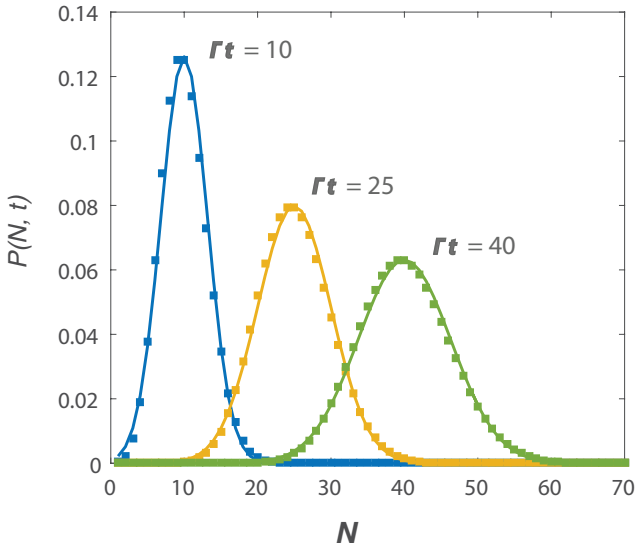

Figure 2.11: Figure highlights the (discrete) Poisson (squares) and (continuous) Gaussian (solid line) distribution for process with same total number of events. The mean and variance are same for both the distributions. The mean is $\langle N \rangle = \Gamma t$. The mean for the three examples increases linearly (in actual transport through a junction, for a constant transfer rate Γ, average time between two electron transfer t increases) while the distribution tail spreads (which in actual transport, highlights the majority likelihood time from all measured times, between two electron transfer also increases and spreads).

Upon differentiating Eq. 2.52 with respect to χ, $\chi = 0$, we can obtain the average, the second cumulant, the third cumulant of electron transfer in certain time Δt in the following equations as,

$$\langle N \rangle = \frac{2e\Delta t}{h} \int \mathrm{d}E T_p(E)[f_L(E) - f_R(E)] \tag{2.53}$$

which can be equated to Eq. 2.33, yielding the Landauer formula; the second cumulant being,

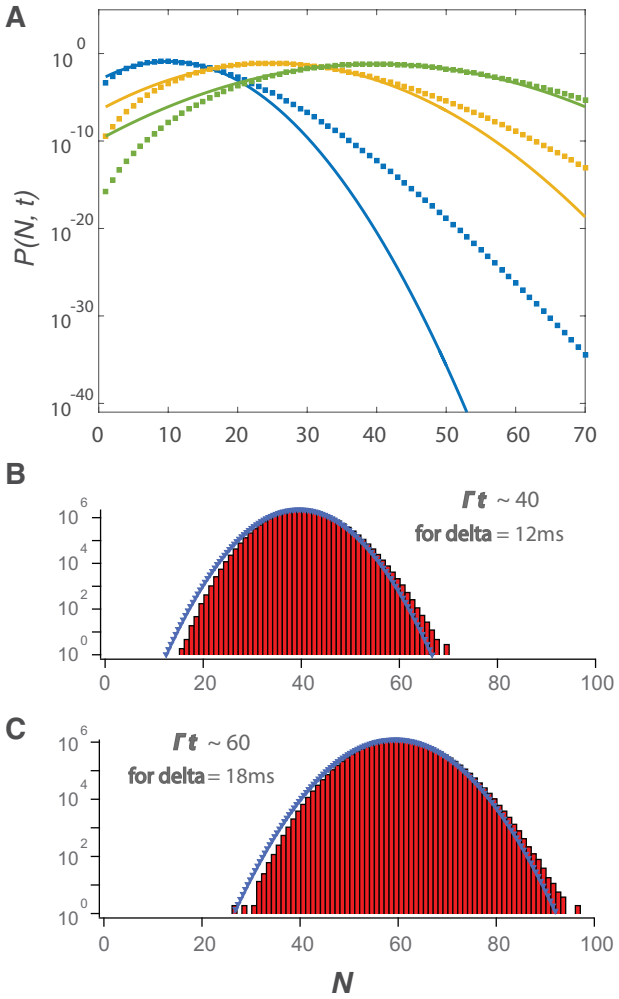

Figure 2.12: Figures highlight the idea as shown in Fig. 2.11 (in A) and from actual experiment data (B-C), in semilog plot with N being the actual events (in few µs units). The blue lines show the Gaussian fits. We observe how the Gaussian diverges at the tails from the Poisson distributed data which get better highlighted in the semilog plots.

$$\langle\langle N^2\rangle\rangle = \frac{2e^2\Delta t}{h}\int \mathrm{d}E\Big[T_p[f_L(1-f_L)-f_R(1-f_R)]+T_p(1-T_p)(f_L-f_R)^2\Big] \tag{2.54}$$

which at equilibrium condition of $f_L = f_R$, i.e., $V = 0$, where only the first term is non-zero, yields,

$$\langle\langle N^2_{eq.}\rangle\rangle = \frac{2e^2\Delta t k_b T}{\pi\hbar}\sum_p T_p = 2\mathcal{G}_\mathrm{Q}k_B T\Delta t \tag{2.55}$$

which also means that the second cumulant does not vanish at equilibrium unlike the first cumulant.

For the case of long measurement time (long Δt), the second cumulant could also be expressed by zero-frequency noise as,

$$\langle\langle N^2_{eq.}\rangle\rangle = \frac{\Delta t S(0)}{2} \tag{2.56}$$

where, $S(0) = 4k_B T\mathcal{G}$ is the equilibrium fluctuation-dissipation or the thermal noise discussed earlier.

At $eV \gg k_B T$ (at shot noise limit, thermal noise is minimum compared to large bias), the first term of Eq. 2.54 becomes zero (while the second term is non-zero), the second cumulant behaves as,

$$\langle\langle N^2_{eq.}\rangle\rangle = \frac{\Delta t S}{2}; \tag{2.57}$$

with,

$$S = 2e\mathcal{G}_\mathrm{Q}V\sum_p T_p(1-T_p)$$

and again, the Fano factor would be the ratio as,

$$F = \frac{S}{2e\langle I\rangle} \tag{2.58}$$

Having seen Fano factor defined in terms of Shot noise, the relation [2],

$$S(0) = 2\mathcal{G}\left[eVF\coth(\frac{eV}{2k_BT}) + 2k_BT(1-F)\right] \tag{2.59}$$

further relates Fano factor F, eV and, k_BT for a tunnel junction, a QPC (and also a diffusive junction).

At equilibrium condition of $V = 0$, the characteristic function of Eq. 2.52 becomes an even function of χ and all odd cumulants disappear. But in shot noise regime, the third cumulant is [2],

$$\begin{aligned}\langle\langle N^3\rangle\rangle &= e^2V\mathcal{G}_{\mathrm{Q}}\Delta t\sum_p T_p(1-T_p)(1-2T_p)\\ &= e^2\mathcal{G}_{\mathrm{Q}}\Delta t\sum_p T_p\Big[eV - 3T_p\xi(eV\xi - 2k_BT) +\\ &\qquad T_p^2(eV(3\xi^2-1) - 6k_BT\xi)\Big]\end{aligned} \tag{2.60}$$

with,

$$\xi = \coth(\frac{eV}{ek_BT})$$

which for $T \ll 1$ yields, $\langle\langle N^3\rangle\rangle = e^2\Delta t\langle I\rangle$. In the case of a SET following the master equation approach from Eq. 2.30, with barriers L and R and corresponding rates of Γ_L and Γ_R, at biases $k_BT \ll eV \geq E_{\mathrm{C}}$ (moderate bias offering Coulomb blockade of say 0 or 1 extra electron, while electron traversing from left to right direction), the average current, shot noise, Fano factor, third cumulant respectively get defined as, [2, 36, 49, 50]

$$\langle I\rangle = e\left[\frac{\Gamma_L\Gamma_R}{\Gamma_L+\Gamma_R}\right] \tag{2.61}$$

$$S = 2e\langle I\rangle\left[1-2\phi^2\right] \tag{2.62}$$

$$F = 1 - 2\frac{\Gamma_L\Gamma_R}{(\Gamma_L+\Gamma_R)^2} \tag{2.63}$$

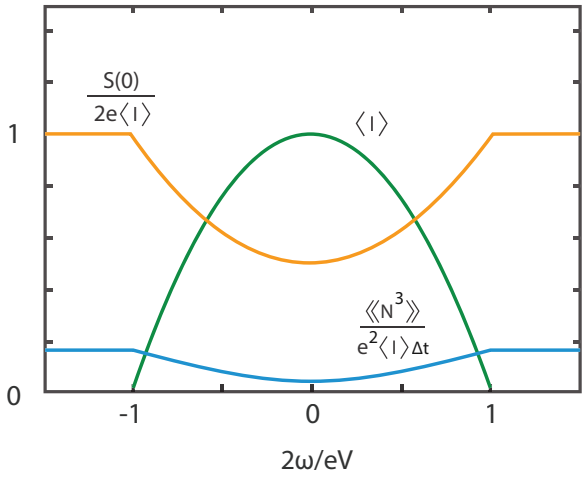

Figure 2.13: Schematised first three cumulants (from Ref. [2]) obtained from expressions in Eqs. 2.61, 2.62, 2.64, with noise and third cumulant normalized over mean current. The plot is schematized for a symmetric left and right tunneling barrier in a SET, with the current flow forming a single Coulomb diamond (current in a SET forming a single Coulomb diamond is discussed in Fig. 3.12 of Ref. [2]). The cumulants approach their individual Poisson limits at the boundaries where Coulomb blockade is observed at the Coulomb diamond ($eV \gg k_BT$), where the current becomes zero. $\omega \sim eE_c(1/2 - nq/e) - eV_{sd}$.

$$\langle\langle N^3\rangle\rangle = e^2 \Delta t \langle I\rangle \left[\frac{1}{6} - \phi^2 + 2\phi^4\right] \tag{2.64}$$

$$\text{with } \phi = \frac{1}{\left[\sqrt{\frac{\Gamma_R}{\Gamma_L}} + \sqrt{\frac{\Gamma_L}{\Gamma_R}}\right]}$$

Since, we would be more interested in the probability $P_\tau(N)$ of average number $\langle N\rangle$ of transferred charges through a junction in time interval τ, as this is the measurable quantity in our experiments, we can more simplistically have the first four cumulants as,

$$
\begin{aligned}
C_1 = \langle N \rangle &= \sum_N P_\tau(N) \\
C_2 = \langle\langle N^2 \rangle\rangle &= \langle (N - \langle N \rangle)^2 \rangle \\
C_3 = \langle\langle N^3 \rangle\rangle &= \langle (N - \langle N \rangle)^3 \rangle \\
C_4 = \langle\langle N^4 \rangle\rangle &= \langle (N - \langle N \rangle)^4 \rangle - 3\langle (N - \langle N \rangle)^2 \rangle^2
\end{aligned} \tag{2.65}
$$

where the C_2, C_3 and C_4 cumulants would physically be the width of $P_\tau(N)$ (the temporal fluctuations of the charges), skewness of the tails of $P_\tau(N)$ and sharpness of the peak of $P_\tau(N)$ respectively; and also the Fano factor as,

$$
F = \frac{S}{2e\langle I \rangle} = \frac{C_2(2e^2/\tau)}{2e(C_1 e/\tau)} = \frac{C_2}{C_1} \tag{2.66}
$$

where, considering that, the statistics of total charge $Q = eN$ transferring across the barrier (unidirectionally) in time τ, we would then have the average $\langle Q \rangle = \langle I \rangle \tau$ with, $C_1 = \langle N \rangle$ and, $C_2 = \langle\langle N^2 \rangle\rangle$. $\langle\langle Q \rangle\rangle \equiv \langle Q^2 \rangle - \langle Q \rangle^2 = s(0)\tau/2$, as shot noise at zero frequency yields the second cumulant [48]. This behavior is verifiable further from Eqs. 2.57 and 2.53 (and further making use of Landauer formalism in Eqs. 2.24 and 2.33) respectively.

Ideally, from the central limit theorem at times $\tau \gg \tau_0$ ($\tau_0 = q/I$ being the instantaneous value), the higher moments (and the cumulants) become increasingly dominated by the lower order moments and hence any irreducible parts of higher moments (or cumulants) that may contain any new information (time behavior), gets increasingly complicated to extract and understand, hence, our discussion of cumulants and moments have got restricted to the first few orders, still, the higher order cumulants could be recursively described as [51],

$$
C^k = M^k - \sum_{q=1}^{k-1} \binom{k-1}{q-1} C^k \cdot M^{k-q} \tag{2.67}
$$

with, C^k, M^k denoting the cumulants and moments of order k.

At weak tunneling rates the distribution is always a Poisson form [52] with the zero frequency spectral density S^k of the kth cumulant as,

$$S^k = \frac{\langle\langle N^k \rangle\rangle}{\tau} = e^{k-1} I \tag{2.68}$$

which is purely due to the dot junction. In experimental situations, this spectral density S also is a factor of the sample (and tunnel junction), the amplifier and the load noises which could be assumed to be uncorrelated [53]. This calls for an experimental setup which limits the thermal noises by cooling the sample to Helium temperatures and below, by limiting the amplifier noises by using very low input noise profile amplifiers and therefore forming the detector setup which is fast enough to resolve any individual charging processes.

Probing and understanding higher order correlations [54–57] in mesoscopic systems has led to much better understanding of quantum statistical, quantum mechanical phenomena [41, 42, 58–61] and further chapters will probe and discuss the technological aspects and the quantum statistical results so obtained to further enrich our understanding on mesoscopic electronic behaviors at low temperatures.

3 Technology of Nano device fabrication and operation

3.1 Motivation

This chapter discusses about the various techniques that were used to create nanostructures on 2-DEG wafers and hybrid nanostructure devices using both local-anodic-oxidation and electron-beam lithography techniques. The hybrid devices were attempted for the first time in this lab and many improvisations over existing techniques were established apart from few newer approaches to create an electrically correct working device. In addition, Appendix A, B, C sections further discusses on the recipes and process details.

3.2 Heterostructures - Theory and relevance to Quantum Devices

3.2.1 Heterostructures - delta doped

Heterostructures primarily have been used to create a lattice with isoelectronic and dopant ions employing Molecular Beam Epitaxy (stoichiometric growth) technique to grow layers of semiconductor materials. GaAs with Si as dopant impurity has been thoroughly studied for few decades and has been the choice of materials for this work. GaAs heterostructures are grown over GaAs substrate with primarily the buffer layer sufficing smooth growth surface, the group-III flux, the group-V flux, the dopant flux to bring in charge carriers, then restoring group-III flux overgrowing over the dopant atoms which act as the spacer region, then finally capping off with very thin GaAs again. The layer growth and dopant flux are precisely controlled processes while additional layers or superlattices are also grown

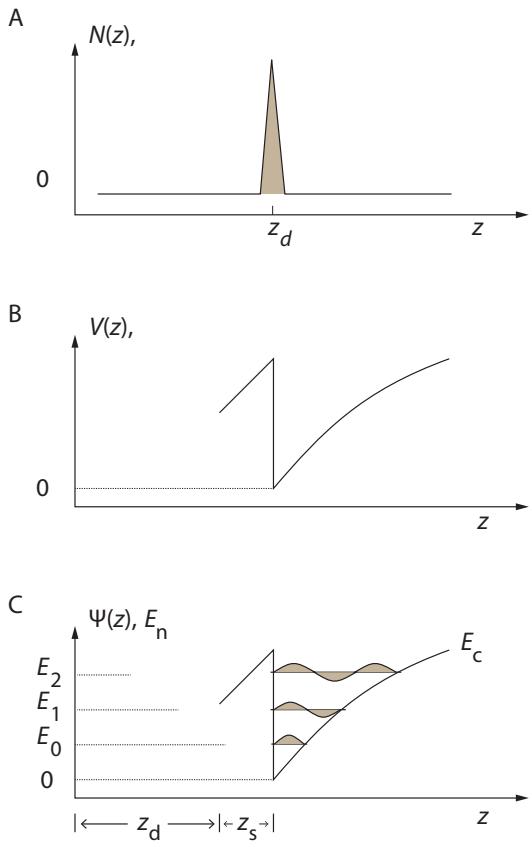

Figure 3.1: Schematic of A. delta-function doping distribution, B. Triangular (asymmetrically V-shaped) potential well created through a δ-function charge distribution, formed at a selectively δ-doped heterostructure, C. Energy levels with quantized charges in the (asymmetric) triangular potential well [62]. z_d, z_s are the depth of the beginning of δ doping and thickness of the spacer layer respectively.

for more superior quantization of majority carriers along the plane of charge transport.

Creating a doping profile with high concentrations and narrow distributions are advantageous for many device applications and, exploring newer physical phenomena employing precise gated control of carrier motion through the dense 2D plane. In III-V semiconductors, distinct positive and negative ion lattice sites allow either an anion or a cation sublattice planar distribution (ideally a single atomic layer) of the dopants. An ideal atomically flat epitaxially grown semiconductor will bear the doping atoms in its substitutional lattice sites while if the semiconductor surface is terraced or a thermally stimulated redistribution of dopant atoms happens after the doping process is finished, the doping profile will not be confined to a single atomic layer.

δ-function like doping profile minimizes the potential fluctuations arising from the random dopant distribution. Since, many characteristics of semiconductor devices depend on the potential fluctuations, for example, the mobility of the free carriers gets seriously affected by the potential fluctuations caused by the random distribution of any outlying dopants. These fluctuations get indeed minimized by the minimal scattering due to narrow profile of δ-doped distribution which has been also predicted to have as much as four times reduced elastic scattering [62].

Assuming a n-type semiconductor with a 2D donor density N_D, the donor distribution along the z-direction (perpendicular to the 2D donor plane) is given as [62];

$$N_D(z) = N_D\delta(z - z_d) \tag{3.1}$$

where z_d is the location of the plane of doping atoms. The doping profile is illustrated in the figure above. The electrostatic potential determined due to the dopant atom distribution, as determined through Poisson's equation would be;

$$V(x) = \begin{cases} -\frac{1}{2}\frac{eN_D}{\varepsilon}(z - z_d), & \text{for} \quad z \leq z_d \\ \\ +\frac{1}{2}\frac{eN_D}{\varepsilon}(z - z_d), & \text{for} \quad z \geq z_d \end{cases} \tag{3.2}$$

with e being the electronic charge. The schematic of Fig. 3.1 illustrates the potential to be linear to z while considering an even distribution of the dopant ions. The V-shaped potential well (though shaped asymmetrically in

the figure, it is still a good approximation for the δ-doped heterostructure) so formed classically allows electrons interact diffusively with the dopant ions and this creates a wider distribution of majority carrier concentration than the pure dopant ion distribution. Ideally, the spatial extent (which is of frequent interest since, most carriers occupy the ground state and its spatial extent is a good approximation of the spatial extent of the whole electron system) of this distribution could be twice of the Fermi screening length of the carriers [[63]]. Upon considering size-quantization of the electron gas, solving for Schrödinger and Poisson equations simultaneously (self-consistently using variational approach [[64]]), the spatial extent of the ground state wave function could be denoted as [[63]],

$$z_0 = 2\sqrt{\frac{7}{5}}\left(\frac{4}{5}\frac{\hbar^2}{e\xi 2m^*}\right)^{1/3} \tag{3.3}$$

where, $\xi = (1/2)eN_D/\varepsilon$. For example, if N_D is $10^{12}\mathrm{cm}^{-2}$, m^* is $0.067\mathrm{m}_0$, z_0 yields a value of 80 Å.

Further, the free carriers though ideally equal in density as that of the dopant ion concentration, will introduce certain amount of band bending right from the point of the plane of doping where it is still like a V-shaped potential discussed early. The band however gets flat farther from the doping plane which signifies presence of more neutral atoms in the region.

Ideally a δ-doped layer would be flat and confined to a single atomic layer and the scattering of free carriers on the ionized dopant atoms are non-existent. However realistically this is rarely possible. In GaAs, n-type δ-doping is introduced through Si donor atoms. Above a certain doping concentration $3 \times 10^{11} cm^{-3}$, the free electrons form a plane across the dopant profile and are free to move even at low temperatures without freezing out on the donor atoms [[63]] and in the direction perpendicular to the dopant layer, the electrons are confined to the Coulomb potential of the donor dopant layer. The V-shaped potential discussed above is smaller than the de Broglie wavelength of the electrons and hence the subbands (quantum states) extend well in the potential profile offering a very near two-dimensional planar profile with more than one populated subbands. Si in GaAs, has a very shallow donor level of 5.8 meV, unity sticking coefficient, and low diffusivity [[65]].

For probing transport properties of the majority carriers in δ-doped semiconductors under the influence of electric and magnetic fields, the microscopic quantities of 'mobility', 'scattering probability', 'scattering time', get directly influenced by the doping process of the semiconductor and the charge transport is a result of the net displacement of these carriers after several microscopic scattering events (not immediately considering a purely ballistic transport, where the scattering entities still play a role depending on the size of the device).

Let us briefly look into these scattering entities. The macroscopic (classical) scattering time to quantum scattering time (quantum lifetime) ratio for GaAs/AlGaAs system is between $5-20$ [66]. At low temperatures the ionized atom scattering gets more prominent over the acoustic and optical phonon scattering. During the elastic scattering process the quantum mechanical phase of the wave-function is conserved. And with a non-zero probability the carrier gets back to its original position, giving rise to weak localization in the absence of magnetic field [67]. The inelastic scattering time are much longer than the elastic scattering time. This inelastic scattering time is dominated by electron-electron scattering and Nyquist scattering which is the scattering of a single electron on the fluctuating potential of the rest of the moving electrons in the 2DEG. The carrier mobility is directly affected by the contributions of each of the scattering phenomena. In δ-doped structures the doping concentration also affects the effective mobility of the carriers through different occupations of the lower most subbands. Higher doping concentration brings in more populated subbands around the Fermi level, while with the higher filled subbands mobilities increase the higher one goes. Though within a higher subband the mobility reduces at higher doping concentration due to stronger confinement of electrons to the doping layer. This is also the case with higher subbands when the thickness of the doping layer is increased, the mobility decreases, as more electronic wave-functions overlap with the ionized scattering centers [62].

We can clearly deduce that, for mesoscopic experiments the idea of size-quantization in devices, using very low operating temperatures and good quality heterostructures are of paramount importance to observe pure physical effects from charge transport.

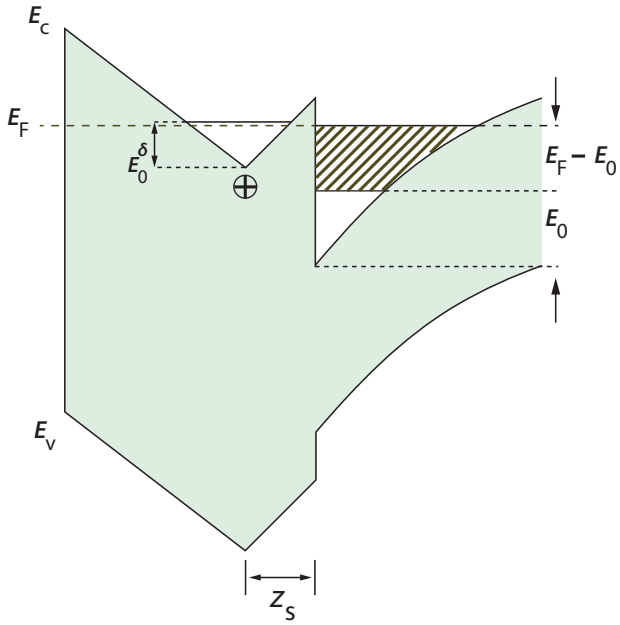

Figure 3.2: Schematic of energy band of a selectively δ-doped AlGaAs/GaAs heterostructure [62]. The δ-doping is selectively made at the wide-bandgap layer of AlGaAs (from the left hand direction of the figure) at a distance of z_d (also Ref. Fig. 3.1). A thin undoped spacer layer (AlGaAs, of thickness z_s) is used to improve the interface roughness between buffer GaAs and AlGaAs layer. This also indirectly improves the carrier mobility by preventing scattering of channel carriers from the ionized impurities (from the dopants). E_0 is the quantized energy of the lowest state of the 2DEG, $E_F - E_0$ is the degeneracy energy of the 2DEG, with E_F being the Fermi level, while $E_F \leq E_0^\delta$ to avoid any parallel conduction in the AlGaAs layer. E_0^δ, E_C and E_V respectively are the size-quantized energies at the δ-doped V-shaped well, the conduction band and the valence band of the heterostructure [63].

The formation of a flat and clean interface with GaAs (narrow-bandgap) and AlGaAs (wide-bandgap) alloys is highly enabled by the nearly matched lattice constants (though $Al_xGa_{1-x}As$, has a larger bandgap, with bandgap being direct for x $<$ 0.4). Figure 3.2 highlights the band diagram at this lattice junction. The band offsets at the interface particularly depend on

the value of x, while x being 0.3, the conduction band of $Al_{0.3}Ga_{0.7}As$ is pinned at 300 meV above that of GaAs [9]. At the interface a dipole interface (through quantum mechanical tunneling) gets build up due to band alignment between the two alloys [68] inducing band bending at the interface. The Si dopant atoms can either form a δ layer or bring in the majority carriers at the interface (modulation doping). While the lowest subband gets mostly populated through the V-type potential, the interface forms a near perfect 2-dimensional electron system offering high mobilities and the semiconductor environment offering a greater control over the mobilities and electron densities allowing large possibilities for controlled charge transport studies through the system. The GaAs/AlGaAs system ideally also provides to easily modulate the Al concentration where, varying the Al content results in varying (square, parabolic) quantum mechanical potentials of the wells so created adding to the different recipes of heterostructures systems to do charge transport studies. In summary, the δ-doping profile, enables a very high achievable free-carrier density and high free-carrier mobility.

One of the heterostructures probed in this work is schematised in Fig. 3.3.

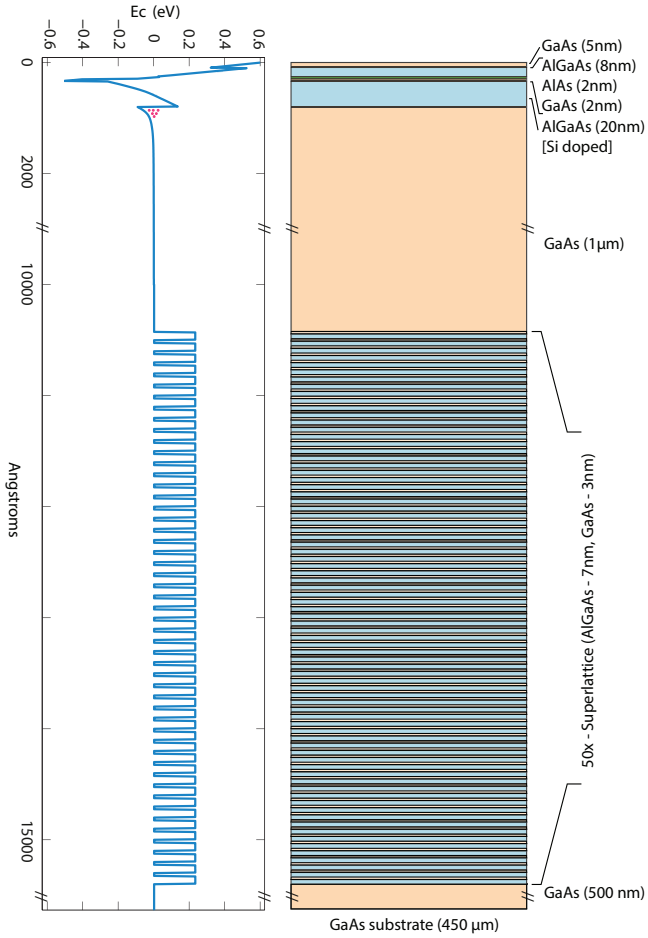

Figure 3.3: Bandstructure (E_C) plot and, grown layer-schematic of one of the shallow 2DEG heterostructure samples probed in this work. The conduction band potential E_C, has been solved using the 1D Poisson Solver [69, 70]. The superlattice was grown to enhance the mobility of electrons at the 2DEG, by reducing the influence of scatterers from the substrate. The 2DEG plane is situated at 37 nm below the surface of this sample. For this heterostructure, the electron density was determined to be $3 \times 10^{11}\text{cm}^{-2}$ and mobility of $1.84 \times 10^5\text{cm}^2/\text{Vs}$.

3.3 Preparation of mesa structure with Ohmic and Surface contacts

Optical lithography with wet chemical processing of the heterostructure surface offers the most practical approach to contact the planar 'carrier rich' region below the surface. Contacting was primarily done through e-beam evaporation of Ge/Au/Ni/Au metals on the mesa surface, and annealing the sample which further forms an eutectic alloy contact at the 2DEG through the surface. Additionally, Palladium based alloy contacts were also probed to test its efficacy in consistent right contact formation. Appendix A, describes the recipes used in the wet chemical processing of the surface and that used for ohmic contact laying using a) the standard eutectic alloy based on Ge/Au/Ni/Au metals and b) using Palladium alloys.

To provide for enough ohmic contacts and top gates in the hybrid structure, an optical mask was designed as shown in Fig. 3.4. Diagonal optical markers were created to facilitate inclusion of minimum of 128 sq. micron size square to enable first alignment scan of the central mesa area under the SEM. This was necessary to bring the number of processing step one further down in the making of the final hybrid structure. This area of 128 sq. micron was estimated after determining the minimum scan line-width of the SEM, the resolution limits of the positive resist (see Appendix A) used during optical lithography, extant of resist development (of certain thickness) at the minimum resolution without adversely affecting the surface of the mesa at the ohmic contact region (since optical markers and ohmic contact were exposed and developed in same steps) and, the stickiness of Gold (as an eutectic alloy) of thickness over 1 micron (since this was the thickness used at the ohmic contacts) without getting ripped off during many further cleaning cycles of the probe. Additionally many a times the last Au layer was made a bit thicker to provide for good bonding of Au wire with the chip carrier. The reason was that, after the annealing process during which the deposited metals at the ohmic contacting region, for an eutectic alloy, the surface Au layer also develops pin-holes of few micron dimensions. Presence of these pin-holes in large numbers were detrimental to a good bonding of Gold wire. This problem was overcome to a greater extent if not totally by increasing slightly the thickness of the final Au layer in the Ge/Au/Ni/Au deposition process. Further it would be been possible to add Ga into the deposition process so as to avoid taking up of Ga from the mesa surface during the annealing process for the formation of the alloy [71]. This wasn't

quite undertaken in this work though Palladium was investigated as an alternate choice for ohmic contacting process. Additionally, Palladium based process also allowed development of one recipe which worked at a lower annealing temperature. This low-temperature process is very important with the idea of minimising activating any impurity species which might otherwise interfere with transport process in the nano-structure (Appendix A for information on the recipe).

The diagonally placed markers were also designed to allow the developer solution to flow easily along the edges to give a sharp profile for a near accurate scan during the SEM step. It should be noted that the heterostructures used for the current work were the 'shallow' donor ones, with the 2DEG depth between 35 - 42 µm and the capping layer of GaAs of thickness of about 5 nm. If the wet chemical processing of the surface was not done rightly or if the mesa surface was not smooth even up to 1-2 nm, the 2DEG beneath used to get depleted at deep-low temperatures.

The above four steps were critically estimated largely through trial and error procedure. Appendix A, details the values which worked successfully for the samples.

Figure 3.4 shows the alignment of optical markers, the first SEM alignment marker, and the extended top-gate contact whose bonding pad was made larger as well enough isolated from adjacent ohmic bonding pads so as to prevent squishing of Gold (25 micron dia. bonding wire was used for bonding contacts to chip carrier pads) from the pads during any re-bonding activity and thus avoid any unnecessary shorts happening through the top-gate contact. The single mesa area (of about 25 sq. microns) with the extended ohmic and top-gate bonding pads and with optical markers occupied 1 sq. mm area and offered the possibility to have four such structures in a 4 sq. mm (20 contact pad) chip carrier. Care was also taken for the metal contact area to extend farther from the mesa edges (at the ohmic contact region) to avoid any increase of contact resistance during high magnetic-field experiments due to higher electron localization through their cyclotron orbits which otherwise could be disturbed with the metal contact extending into the substrate where the 2DEG had been etched away [9].

Figure 3.5 show the SEM images of markers done through optical lithography (Fig. 3.5-Left, also refer Fig 3.4 for the marker at 128µm from the mesa center) and SEM lithography (Fig. 3.5-Right) to lay the final structure.

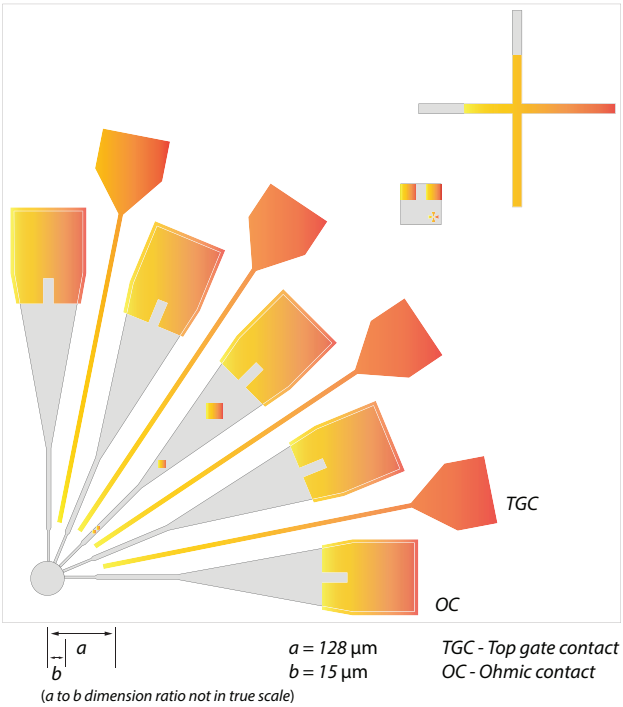

Figure 3.4: Schema of the designed optical -mask and -lithography regions (mesa as grey colored, optical markers and ohmic contacts as golden-red colored) used in the sample preparation. This mask offered possibility of 16 ohmic contacts and 16 top-gate contacts, while allowing four such structures in a 4 x 4 mm sample surface. The top-gates are electrically insulated from the 2DEG underneath the surface with resistances of few hundred MΩ (for sample densities discussed in the text) at room temperature. Ohmic contact (OC) metallization region extends over the mesa to avoid higher contact resistance at higher magnetic field experiments (see text). Top gate contacts (TGC) pads are bigger and farther than ohmic contact pads to allow convenient bonding. Markers (discussed in Fig. 3.5) placed at a distance from center allowed rapid positioning during SEM lithography process (see text).

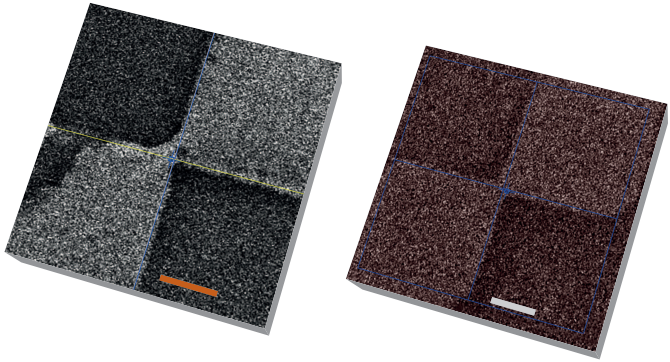

Figure 3.5: SEM scan image of differently laid markers, the left-image marker was laid through optical lithography, scale = 2µm; the right-image marker was laid through SEM lithography, scale = 500 nm; bright region is metal layer and, dark region is mesa surface. The left-image is the marker positioned at distance 'a' from mesa centre (ref. Fig. 3.4). The particular shape of markers, helped in accurate cross-hair positioning, which was also easier to create anticipating mechanical flow of developer solution on the resist, creating sharper inner edges, while also allowing enough surface area to stick on the mesa (see text) and all the while accurately aiding the hybrid lithography.

This distance from the mesa center, also accommodated the idea of the SEM scan line width to be consistently an integral multiple of lowest line width resolution offered by our SEM system. This distance offered a SEM scan area of 256µm which allowed consistent and repeatable quality of nanostructuring during SEM lithography with one process step less since the marker was already available through optical lithography. The SEM scan screen-shots of the markers in Fig. 3.5 have been particularly included in the discussion here to highlight the fact that, after two lithography and metal deposition steps (while this screen-shot was taken), the markers had not got any overlayed metal at their positions, underlying the idea of 'SEM scanning area enclosing the markers' and 'minimal scanning at minimum resolution for the set SEM aperture' was necessary to accurately reuse the markers for aligning the AFM and SEM lithography steps.

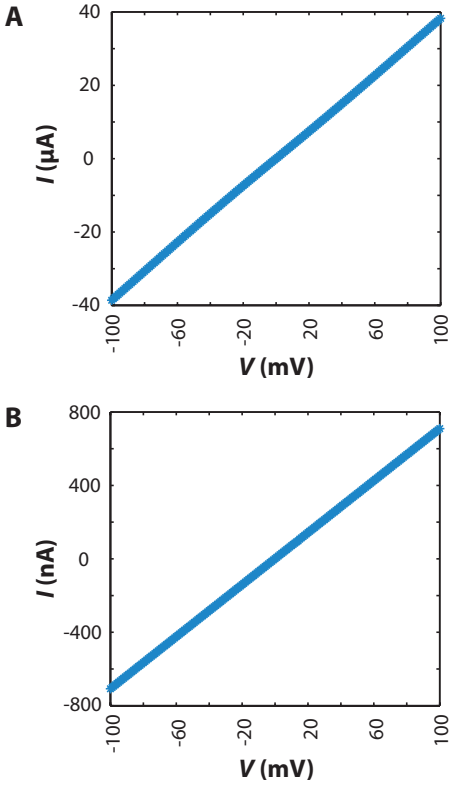

Figure 3.6: Ohmic behavior of Palladium alloy based ohmic contacts in AlGaAs/GaAs heterostructure samples (between two opposite contacts of the star structure discussed in the text) with two different electron densities (see text), with slopes of 141 kΩ (A, with low electron density) and 2.6 kΩ (B, with comparatively higher electron density), both at 4K temperatures.

For laying ohmic contacts, apart from the (now) standard eutectic alloy of Ge/Au-/Ni/Au based contacting process, Palladium (Pd) metal was investigated for laying contacts on n-GaAs [71–75] (see recipes investigated, in Appendix A). The Ge/Au-/Ni/Au eutectic alloy based ohmic contact had problems in ohmic contacting all the 16 ohmic contact region in the 16 x 16 star mesa structure used in this work, consistently. Pd metal alloy based contact offered a substantial alternative to provide maximum useable ohmic contacts in the 16 x 16 star mesa structure quite consistently. Figure 3.6 highlights the ohmic behavior for a very wide range of voltage (compared to what is usefully employed for quantum dots), in I-V curves of the ohmic contacts (at diagonal opposite ends) measured in the 16 x 16 mesa structure for two different shallow 2DEG heterostructures. The electron density for the 2DEG employed in sample A (Fig. 3.6-A) was $n = 3 \times 10^{11}\text{cm}^2$ and for sample B (Fig. 3.6-B) was $n = 4.5 \times 10^{11}\text{cm}^2$.

During the sample testing process, many shallow 2DEG heterostructures were investigated for optimum mobility and electron densities. In the initial set of wafer-lots it was observed that though the mesa surface was optically perfectly flat with clear RHEED (reflection high energy electron diffraction) spectrum for the prepared heterostructures, the samples constructed using these wafers did not conduct at 4K temperatures. They otherwise showed identical room temperature behaviors on measurements of resistivity. Their electrical conductivity worsened below from about 100 K temperature. Upon atomic force microscopy investigation of the sample surfaces, it was found that the samples had undulations with valleys and hills as shown in Fig. 3.7. The valley dips with about 2 nm dimension were very likely depleting the majority carriers at lower temperatures and showing higher resistivity subsequently. Upon careful investigation of the MBE growth process, it was found that the sample holder were harbouring micro (though optically visible) cracks and these supposedly created large temperature gradients on the wafer surface during growth process which finally resulted in atomically non-flat final surface. The problem was gone once the sample holders in the MBE were attended to.

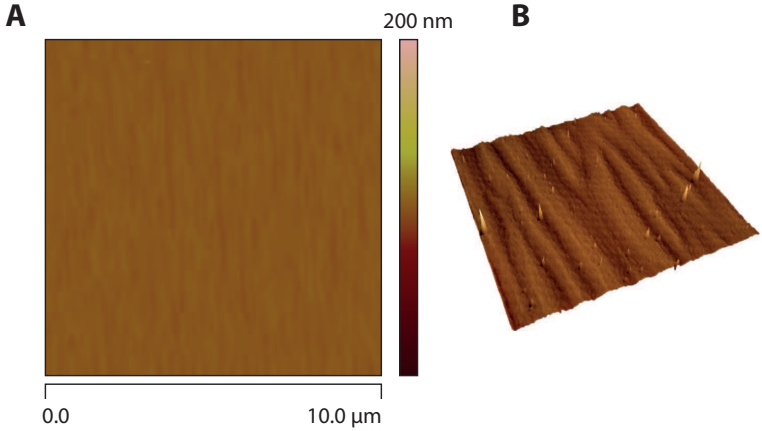

Figure 3.7: Surface undulations contributing to non-conducting samples at temperatures below 100K. A) 10 µm sq. area AFM scan of the sample surface with B) showing the same surface in a 2 µm sq. area scan. The valleys in both A and B have height range of between 1.5 nm to 2.7 nm.

3.4 Nanostructuring through AFM and SEM lithography

Since the invention of scanning tunneling microscopy (STM) by Binnig and Rohrer, at IBM in the mid-80s, [76], has heralded the probing of most material surfaces in the greatest detail as possible today [77, 78] where the scanning tips were terminated with a CO molecule to achieve a very high resolution of the probed complex organic molecule. STM probing techniques can be mechanically done through very sharp tips as in AFM by measuring the force between the tip and the surface, or the surface and just below the surface probed for LDOS (local density for states) by measuring the very small tunneling currents through the surfaces. STM tips can even pick and move atoms electrostatically as was shown by IBM's Don Egler in 1989.

AFM technique particularly, uses a very sharp (of the orders of few tens of nanometers uncoated tip radii, while for a coated tip the radius could

be in the order of few microns) tip, to mechanically scan a surface and build a surface profile of the scanned surface. The mechanical scanning either happens through continuous contacting the surface or by tapping the surface at high frequencies while progressing with the scan. The latter method usually provides for high tip life and scanning of softer surfaces. The scanning tip is held on to a cantilever with a very high Q-factor, piezo resistive (typically a lead zirconate titanate material) detector which reacts to small vibrations on the tip with an amplified resonant output. This is precisely detected using a reflected laser beam which then feeds the the beam scatter information to profile the scanned surface undulations. Further the feedback of the tip's z-movement is additionally determined through the cantilevers head control which ideally is programmed to create a certain controlled deflection of the cantilever in the z-direction, either in contact or tapping mode of scan enabling error free profiling of the surface through the tip.

Atomic force microscopy since the past decade, also has been used very successfully to create nanostructures on a 2D plane [79–87] using a certain technique called local anodic oxidation (LAO). LAO [88–90] uses a conducting tip in a contact mode wherein, an optimum potential difference (8-12 V DC) between the tip and the lithography surface, creates a chemical reaction locally which looks like [91–94];

At the GaAs surface;

$$2GaAs + 6H_2O + 12h+_{\text{hole}} \rightarrow Ga_2O_3 + As_2O_3 + 12H^+$$

$$6H_2O + 12h^+_{\text{hole}} \rightarrow 2O_2\uparrow + 12H^+$$

At the AFM tip:

$$12H_2O + 12e^- \rightarrow 6H_2\uparrow + 12OH^-$$

At the water meniscus:

$$12H^+ + 12OH^- \rightarrow 6H_2O$$

where h^+_{hole} are the positively charged holes on the GaAs surface. During the oxidation process at the tip and the surface, the H^+ and OH^- ions recombine to yield the Ga and As oxides on the surface. The oxide formation process at the surface also extends locally below the surface [95]

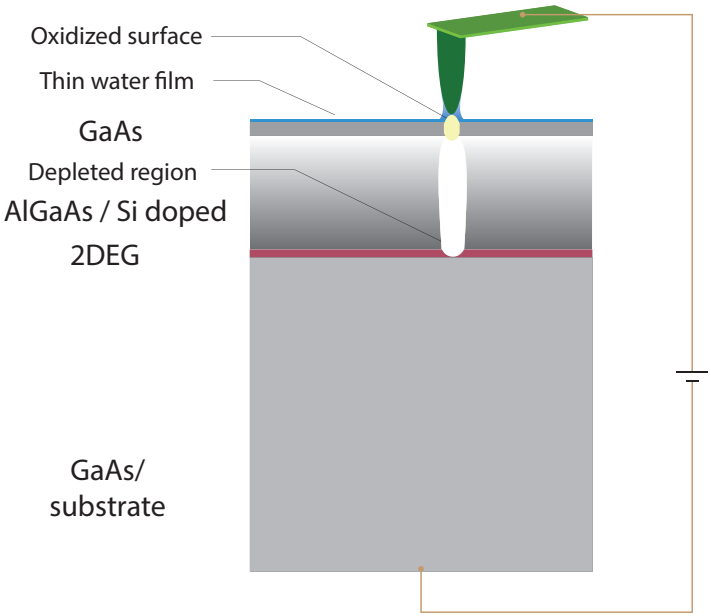

Figure 3.8: Simple schematic of local anodic oxidation using atomic force microscopy.

as shown in Fig. 3.8. The spacer region above the 2DEG subsequently gets electrostatically depleted of free electrons and since in a shallow 2DEG heterostructure, the 2DEG lies close to the surface with larger percentage of dopant ions still available closer to the surface, the depletion process easily extends to the 2DEG planar layer beneath the oxidised region. The oxide growth energetics can also be illustrated as [91, 96],

$$dh/dt \propto \exp -h/l_c \tag{3.4}$$

where, h is the oxide thickness at time t and l_c is a characteristic decay length depending on the anodisation voltage; hereby, implying that, the

scan rate, anodising voltage are equally important along with the loading force on the tip during the writing process.

The loading force on the tip also creates a trench locally at the spot of oxidisation and this acts in tandem to the oxidation process, in removing material below the surface and creating a stronger isolating barrier. The 2DEG beneath the oxidised region hence forms a barrier yielding resistances of up to few mega ohms at room temperature to non-conducting at liquid Helium temperatures, at up to few hundred millivolts. The oxide barrier capacitively insulates the two region it isolates. This capacitive isolation ideally depends on the extent of the oxidation (thickness and sub-surface depth profile which together form the oxide line aspect ratio) of the barrier. This capacitive isolation hence provides us a controlling gate for the flow of electrons below the surface at the 2DEG wherein, lower capacitive coupling to the other side of the barrier means the gate has less influence on the charge flow across the other side of the barrier and likewise, for higher capacitive coupled barrier, the gate potential has larger influence on the charges flowing across the other side of the barrier. The coupling across the barrier is influenced by the use of positive or a negative potential respectively on the other side of the barrier.

After the LAO structuring has been accomplished, using the SEM laid markers the structure is aligned in the final SEM lithography step for the top-gate structures. This technique follows the now very standard technique of using very thin polymer resist (Appendix A, for recipe) as the SEM scan mask, which is exposed, developed and metal is evaporated to form the final top-gated structure. The top gates formed with the SEM lithography also, capacitively couple with the 2DEG beneath the surface through a negative or a positive voltage at the gates. A negative voltage, ideally forms a barrier electrostatically just below the surface (at the gate) while likewise a positive voltage has an opposite behavior below the surface. This influence of formation of barrier is again used to create controlling gates for the electrons to flow across the other side of the barrier and controlling channels for the electrons to flow just below the gate.

From Fig. 3.9, we see two examples of the hybrid nanostructures engineered for this work. During experiments it was found that the quantum point contacts formed through the top-gate and the AFM oxide barrier, were very sensitive to the charges flowing across the other side of the barrier (through the quantum dots). This was probed at different temperatures

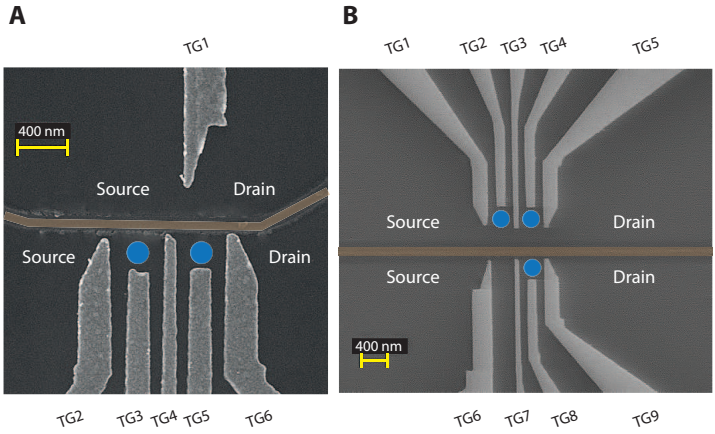

Figure 3.9: SEM images of two examples of hybrid-nanostructures probed in this work. The pale line marked for visibility, is placed on the trench (from AFM lithography, in the image) is the AFM nanostructured lateral barrier. TG refers to 'top gates'. Source and Drain contacts form the channels for the quantum dot and the quantum point contact to conduct through. For image A, the AFM line is less than 50nm away from the TGs forming the double dots, while the QPC TG is about 200nm away on the other side of the AFM line. For image B, for single dot side, the AFM line is again about 50nm away from the TGs, while double dot TGs are about 170nm away from the AFM line on the other side. The AFM barrier is of about 230nm wide (including the depletion widths) on both images.

from about 350 mK to up to 15 mK temperatures (in a dilution fridge). The hybrid structures investigated in this work could not be reliably used for the charge-counting experiments since the structures were very noisy in terms of the QD (quantum dot) current and QPC (quantum point contact) current, when probed at 400 mK to 15 mK temperatures. The noise has largely been attributed to the 2DEG which couldn't be done away for any appreciable measurements. About 20 different wafers were investigated for the right QPC and QD current behavior with simple nanostructures on few of them and with complex nanostructures on few of them.

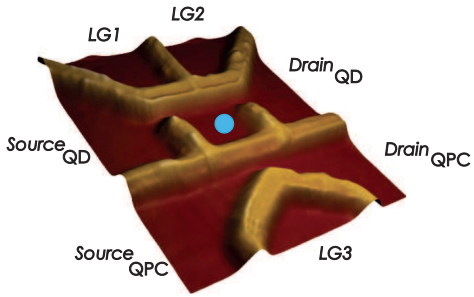

Figure 3.10: AFM image of nanostructure used for the results discussed in this thesis. The raised pale ridges are the oxidised barriers. LG refers to 'lateral gates'. Source and Drain contacts form the channels for the quantum dot (QD) and the quantum point contact (QPC) to conduct through. The size of the quantum dot at the centre is $\approx$ 300nm across.

Figure 3.10, shows a LAO nanostructured device done on a separate wafer from the former labs of M. Reinwald and, W. Wegscheider of University of Regensburg, (sample C021227B) [97].

The single electron transistor device, is formed with two barrier gates G1 and G2 which can electrostatically enclose the quantum dot (marked as blue disc in the image) while forming tunneling barriers across it. Source_{QD} and Drain_{QD} form the source and drain contacts for the quantum dot. A quantum point contact (QPC) is formed using the gate G3, which can electrostatically create a 1-dimension (1D) channel between the barriers of the quantum dot and the gate G3. The barrier formed through LAO creates a capacitive coupling of the two regions across the barrier and the extent of this capacitive coupling depends on the barrier-height to barrier-width ratio or the aspect ratio of the oxide line. A higher capacitive coupling would need a smaller width with a larger height, which is possible with very narrow AFM tips and good LAO technique (which depends dominantly on the variables of ambient humidity at the tip, operating temperature, tip writing speed, tip potential and, surface of the material apart from

hardware/software local parameters). The current flowing through the 1D QPC channel (across the source and drain contacts of the QPC) gets capacitively coupled to the charging and discharging process at the quantum dot (discussed again in the next chapter) and hence forms a very sensitive detector for the electron transport happening through the quantum dot and across its barriers. This sample had an electron density $4.59 \times 10^{15}\mathrm{m}^{-2}$ and mobility of $64.3\mathrm{m}^2/\mathrm{Vs}$ (at 4.2K). The diameter of the quantum dot disc (as determined, through the dot capacitance deduced from charge stability diagram discussed in the next chapter along with the physical dimension after subtracting for depletion region of the oxide lines from all sides) was found to be $\approx$ 250nm. The mean single level spacing was deduced to be $\Delta \approx 95\mu eV \geq k_B T$. With the disc of radii being $\simeq$ 125nm, we would have the total number of electrons occupying the quantum dot at equilibrium to be $\approx$ 225 electrons. The charging energy of the dot obtained from the charge stability plot of Fig. 2.8(bottom) is $\approx$ 1.2 meV. Our discussions on experiments and results will consider measurements from this device.

3.5 Experiment

For the experiments, a Helium-4 fridge with solenoid magnets for fields up to 13T was used. The temperatures achievable through this system was about 1.5K. An insert for Helium-3 circulation (using a turbo pump) with two line-of-sight coaxial lines (lab constructed, Manganin alloy wired with few hundred pico Farads capacitance each) was used to achieve temperatures up to 350 mK. Sample fixed on a chip-carrier is then mounted on the sample-rod with the coaxial channels and is vacuum sealed and thermally contacted in the He3 insert which is then fixed into the He4 VTI (variable temperature insert). Over few hours of cooling cycles with He3 and He4, a base temperature of about 350 mK was achieved around the sample. The coaxial lines provide a high-fidelity low current detection channel for the quantum point contact current measurements. And hence for sensitive detection of very low QPC currents, the QPC were always connected to the coaxial line.

Each HF line was wired with 'manganin' alloy wires, and the measured capacitance for each line was about 120 pF (the capacitances can significantly vary if the wire is not taut from end to end soldering), and the line

capacitance along with the switchboard BNC output in series was about 1nF. The QPC is not connected through the switchboard, but directly connects the HF SMD connection through a Femto current amplifier as discussed below.

From Fig. 3.11, a lock-in amplifier was used with a 13 Hz sinusoid signal to lock-in on the QD current, while the amplitude was maintained at 10 µV at non bias situation at the QD. The lateral gates were controlled using computer controlled DACs (DAC488HR). Each lateral gate input was filtered using a 1-10 Hz low pass filter. The output of the QPC was measured using a ultra low noise (input noise at 180 aA/$\sqrt{\text{Hz}}$) current amplifier (Femto Messtechnik GmbH). The bandwidth of the amplifier was 400 kHz with gains up to 10^{13} V/A.

The switch-box was additionally filtered for high frequency signals. Great care was taken to avoid ground loops forming due to different instrumentation sources, power supplies for the instruments, and vacuum and pumping systems. For the DACs and lock-in amplifier a separate power supply with isolated transformer was used. QD currents were amplified using Itahco DL1211 current amplifier and, this was connected to the isolated transformer power supply. The Keithleys for DC measurements were connected to a separate power supply since they had a constant high frequency power line signal generating from their power units. The Femto current amplifier was powered by a battery operated power supply. Proper terminations (50 ohms) were always provided on the coaxial lines. The QPC signal was digitised through Keithley (KUSB 3116) data acquisition board (500 kS/s at 16-bit resolution) and recorded in binary format.

Figure 3.12 shows the sample stick which held the sample, with provision for two high frequency LOS (line of sight) lines, inside the He3 insert, during the experiments. The turbo pump was attached at the opposite port from what is visible for the Fischer connectors. The use of turbo pump allowed comparatively lower base-temperature of $\sim 350mK$ at the sample, to be achieved during the cooling process, though the base temperature remained so for 2-3 hours. The calibration of the detector and counting experiments had to be performed within this time. Without the turbo pump, the base temperatures were slightly higher but the base temperature remained so for about 4-5 hours of operation. The extent of base temperature ideally depends on the amount of heat carried into the sample through all the cables, the high-frequency lines and insert assembly.

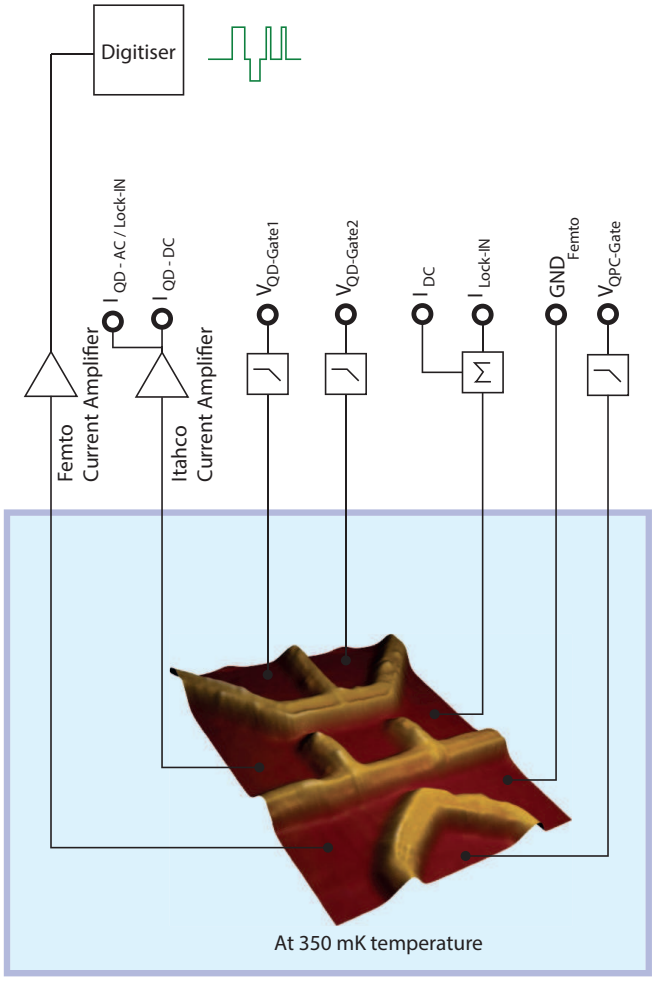

Figure 3.11: Measurement setup schema used for the counting experiment. The setup used He3 insert with a turbo pump, with the He3 insert sitting in a He4 wet-fridge from Oxford Instruments. $I_{\text{QD-DC/AC}}$ respectively describe AC and DC current components from the quantum dot (with the AC component separated through the Lock-IN, see text), $V_{\text{QD-Gate1/Gate2}}$ respectively describe the voltages at tunneling barrier gates, V_{QPC} is the QPC gate voltage, the Femto current amplifier reads the QPC current, which is further digitised and saved as binary data.

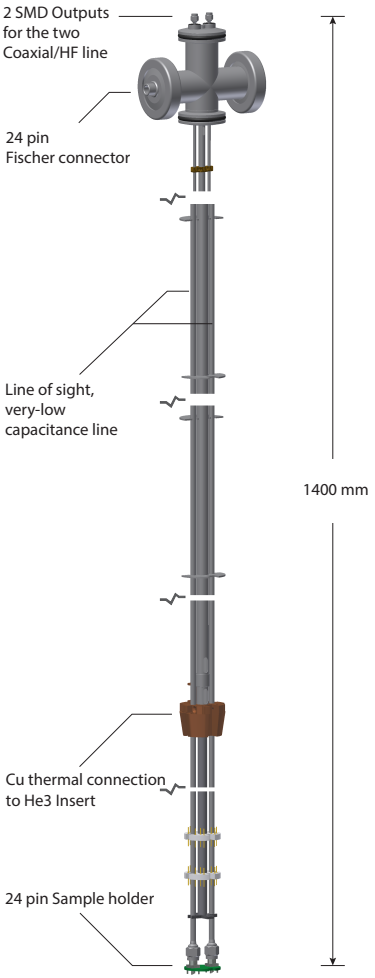

Figure 3.12: Measurement stick for holding the sample in the He3 insert, in the experiment setup. The high frequency line was critical to get very good signal to noise ratio for the QPC current, which otherwise couldn't be resolved enough to calculate higher moments, from signals using normal twisted pair copper line. The high frequency line is further discussed in the text. Thanks to Mr. Ronny Heuther for supplying with an original CAD image for this figure.

4 Experimental detection and counting process

4.1 Motivation

In this chapter we would discuss the techniques of experimentally detecting and counting of charges flowing through the quantum dot using a 'quantum point contact' and further, upon gathering the data, how the data is prepared for statistical analysis. The underlying algorithms to analyse the data towards estimation of normal cumulants and factorial cumulants are discussed in detail. Parts of text and figures would be similar to those presented in the publication tentatively titled, 'Factorial cumulants in conditional tunneling regime in a single Qauntum dot'.

4.2 Experimental detection of single charges using a Quantum Point Contact

After the quantum dot (SET) is set to its optimum operating point through appropriate voltages at the lateral gates (Fig. 3.11), where the left and the right gates are optimally open to allow discrete charge flow through the barriers, the charge on the quantum dot is detected non-invasively (not in strict sense) through a capacitively coupled quantum point channel. In physical terms the transmission of this 1D channel depends proportionally on the charge in the quantum dot with and the effective capacitance at the dot due to all other gates in operation. The potential difference between the two transmission coefficients in the QPC channel ($\delta T = T(N+1) - T(N)$) for the charge configurations of N and $N+1$ in the dot, however is very small [[2]], a measurable current of

$$\delta I = \mathcal{G}\delta T V \tag{4.1}$$

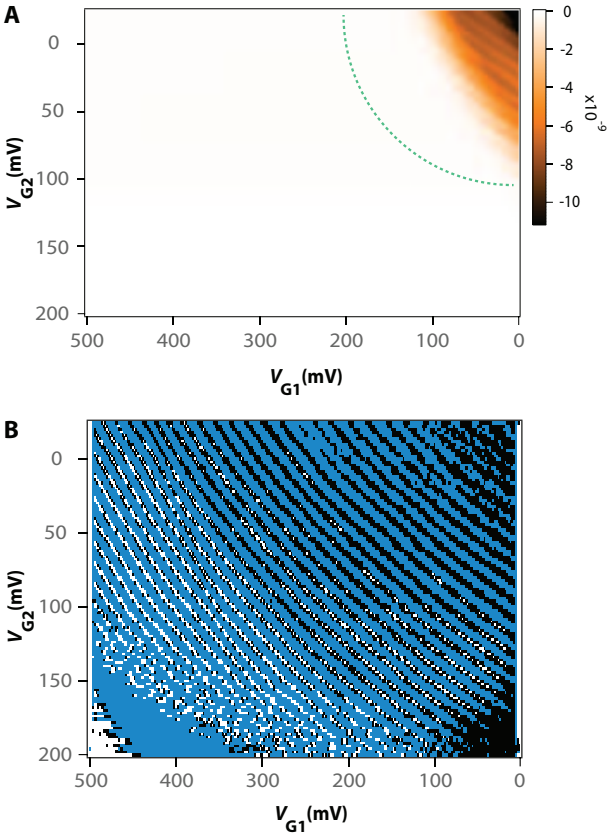

Figure 4.1: Top and bottom figure show the charge current so measured flowing through the SET with, the top figure showing what is detectable as the SET Current through the tunnel (Drain) junction (in few hundreds of nA), the bottom figure showing what is detectable as the QPC Current. The black dots in the bottom figure constitute the charge current (in few hundreds fA) wherein at the bottom-left part, the currents start from the pinch-off region of the QPC. VG1 and VG2 are the barrier gates of the SET (gates LG1 and LG2 from Fig. 3.10), are closed/opened in tandem slowly for the single charge measurements.

for a voltage of V across the channel, flows through the channel. While operating the channel close to the leading-edge of first conductance plateau, the QPC current gets highly sensitive for single electron changes at the dot. A very sensitive (preampliers with gain of above 10^{13} V/A) and fast measurement setup, is employed to measure this current. Figure 4.1 highlights (for the quantum dot in equilibrium) the changes in current that is detectable at the QPC and shown as black points in the lower graph which is however not-detectable as a dot current which is measured through the tunnel junction as the quantum dot $Source - Drain$ current as shown in the top graph. The region below the 'green' dotted line boundary shows no value when in fact the QPC has visibly measurable values in this region. Pioneering experiments [87, 98–103] had very much standardised the use of QPCs as charge detectors in resolving single electron transport process in quantum dots. Figure 4.1-B also highlights two regions in the lowest bottom corners. The left-bottom corner informs region of a nearly closed quantum dot, with few to none electrons tunneling through the barrier, while on the right most bottom corner, the gate G1, opens up totally and the dot is strongly coupled with the 'Source'. This quantum dot is usually operated in the region where just a single electron could be tunneled through while maintaining a certain positive bias to form a uni-directional current flow.

From the QPC data, we have for $q = 1.602 \times 10^{-16}$C, the capacitances at the barriers as,

$$C(G1) = \frac{q}{\delta V(G1)} = 16\,\text{aF}$$
$$C(G2) = \frac{q}{\delta V(G2)} = 6.56\,\text{aF}$$

for respective δVG1 and δVG2 of 10 mV and 24 mV. The values compared to earlier experiments of Fricke et. al [104] have differed, due to deteriorating gate barriers (through natural aging process of the oxide barriers).

We have to be aware that the visible change in QPC current happens with the whole QPC circuit in picture, which includes the SET's QPC, the connecting line's reactance, the amplifier input noise behavior. This detected current at the QPC is hence not inferred in isolation of the underlying detector circuit at play. We therefore would need to understand the noise of this

detector circuit at the input, and the detected current should be larger than the noise at the input of the detector, given as,

$$\delta I > 2\sqrt{2} \cdot \text{Noise current of the detector} \tag{4.2}$$

The RMS internal (referenced to) output noise current of the detector (the QPC circuit) from the (referenced to) input noises from the amplifier and the QPC (at the sample), would be [104]

$$I = \sqrt{\int_0^{BW} I_{\text{amp}}^2 d\omega + \int_0^{BW} 4\pi^2\omega^2 C^2 V_{\text{amp}}^2 d\omega + \int_0^{BW} \left[\frac{V_{\text{amp}}}{R_{\text{qpc}}}\right]^2 d\omega}$$

further yielding,

$$I = \sqrt{\frac{4}{3}\pi^2 C^2 V_{\text{amp}}^2 (BW)^3 + I_{\text{amp}}^2 (BW) + \left[\frac{V_{\text{amp}}}{R_{\text{qpc}}}\right]^2 (BW)}$$

where, V_{amp}, I_{amp} are respectively the voltage and current noise values ($/\sqrt{\text{Hz}}$) of the amplifier, BW the bandwidth of the amplifier, R_{qpc} is the quantized resistance of the QPC ($\sim 26\,\text{k}\Omega$) and, C is the capacitance of the measurement channel ($\sim 120\,\text{pF}$, see Chapter 3). The 400 kHz Femto current amplifier employed in our experiment at the QPC, along with the QPC, allowed QPC current sensitivities of the order of minimum of few nano Amperes.

In our experiment, the tunneling rate of the electrons across the 'Drain' junction was in the range of few to few tens of kHz (see Chapter 5 for discussion on rate values), which sufficed the quick measurement possible through the QPC channel.

There are further certain possibilities of sources of noise in a QPC current. Using QPC for charge detection also entails that its own operating state does not become a source of noise. Yuan et al. [105] discussed that, an ideal QPC wouldn't generate shot noise when electrons are not backscattered as they traverse the channel, unlike for, any ballistic channel which can be a shot noise generator too [106]. Further sources of QPC current noise could be from, electrons taking part in transport from several subbands at higher

temperature at the device, the fabricated channel being non-smooth at the edges causing non-adiabatic transition from 2D to 1D transport and, the presence of hot electrons at the channel.

The QPC channel formed through gate G3 (Fig. 3.10) and $Source_{\mathrm{QPC}}$, $Drain_{\mathrm{QPC}}$ channels are energised with a very small voltage across the channel. The experiment used a voltage of $\approx 100\,\mu\mathrm{V}$ to drive the channel. This small voltage is very important due to the backaction of the energy across the the QPC and the quantum dot circuits [107–117].

At low temperatures an energy exchange between the two circuits of 'quantum dot' and the 'QPC' is mediated through the interactions of interface acoustic phonons, and these phonons can pass through an electrostatic barrier between these two circuits, unlike electrons. The backscattering of an electron from the leads (with non-equilibrium state distribution) has an upper limit energy of $E^{Ph} = 2\hbar k_F v_s$, v_s being the velocity of sound of about $v = 5.3$ km/s, for longitudinal acoustic phonons in bulk-GaAs in [110] direction [118]; wherein only the phonons with momentum $\leq 2\hbar k_F$ are absorbed back by the electrons (owing to conservation of energy and momentum). On the other side, bias through the dot, also induces absorption of interface acoustic phonons at the detector circuit due to non-equilibrium conditions (from energy and momentum) again from the leads (necessitating a certain bias through a QPC to overcome these phonon) and at higher V_{sd} voltages, phonons from high energy electrons will have momenta $\geq 2\hbar k_F$, the momentum conservation allows only the perpendicular component to be significantly large which then propagates ballistically with mean-free path larger than the crystal dimensions [113, 119].

The QPC and dot bias values are set, with the above discussion in perspective for correct operation of the SET. QPC bias was however varied around $100\,\mu\mathrm{V}$ to correctly operate the QPC. The value varied owing to finding the right operating point which altered slightly between repeated cooldowns and the changing asymmerty of the gates (due to deteriorating oxide barriers). The QPC current after amplification were in the range of few hundred nA. We have discussed that the QPC is just able to differentiate the presence or the absence of charges in the quantum dot. QPC cannot differentiate the direction of tunneling process. It is henceforth essential to provide for a uni-directional electron transport mode of experimental investigation by biasing the quantum dot enough, allowing the tunneling process to be very clear in the single QPC current measurement.

4.3 Preparation of experimental data for statistical analysis

From the experiment discussed in the next chapter, an hour measurement of 'electron counting' saved in 16-bit binary format, yielded a file of about 3.5 GB and to process the entire data in a 32-bit machine (OS and Matlab) gets a bit tricky, even, a 64-bit OS wouldn't overcome limitations due to the processing software, Matlab which was of 32 bit during most of the data processing done for this thesis. This is not a problem when data file size is few MB long and a single program iteration can flawlessly perform the statistical calculations.

In the case of the 3+ GB size file, since the entire data could not be processed as a single variable, the data file was truncated at optimum lengths (so determined by being able to run the whole sets of calculations without any memory overflow), it was critical that the truncated parts matched since when this do not happen, the entire statistics get different and wrong.

Another further experiment discussed in the next chapter, from operating on 4040 files set of few MB size each, for different procedures (in a single iteration though), to identify the waiting times and to calculate different cumulants, equally required optimal management of memory resources and error checking at different stages.

Once the noise from the data were dealt with, to allow for further correct data interpretation, error checks of

1. for the truncated part, comparing the previous byte and the next byte of raw data, with the corresponding processed data at the point of truncation,

2. logically estimating that a 'waiting state' cannot be in more than one state at any instance, for each (truncated or full) set of data

3. programmatically, allowing for random optical cross-check of actual data points in the current trace, with the corresponding inferred length of 'waiting time'

were continuously performed at parsed data during calculations and saving the sum results.

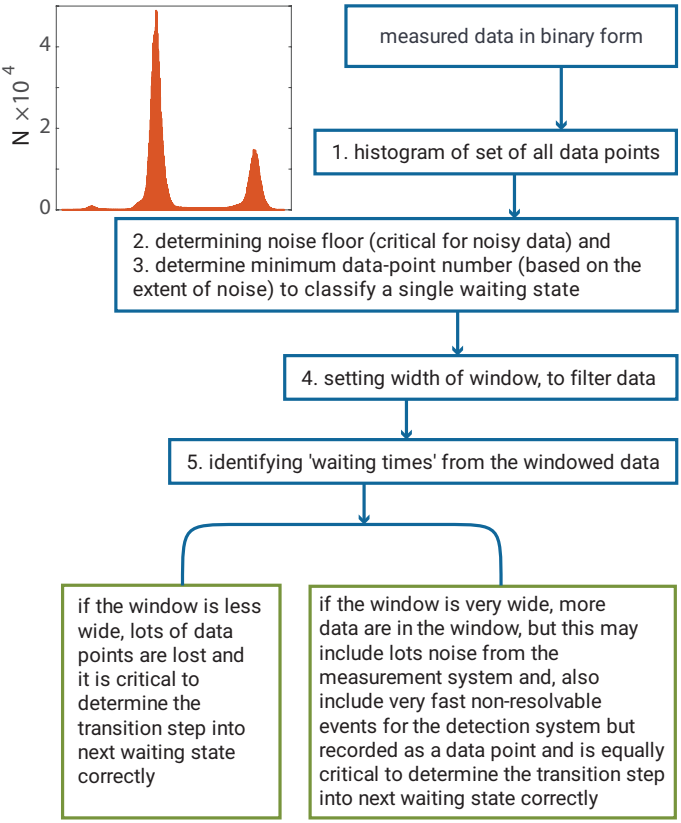

Figure 4.2: Simplified 'flow and relationship schema' for the procedure involved in determination of waiting times from the measured raw data. For set of data comprising of 4040 files, the whole process is totally automated with very optimal values for all parameters to isolate noise, set window filters, set minimum data points, to yield right output. The output is extensively checked upon, after calculations with random individual file processing. The step of 2 through 4, will be again further discussed in Chapter 5.

4.4 Process flow for estimation of statistical parameters

In addition to the brief scheme of data processing from Fig. 4.2, the following succinctly explains the algorithm steps;

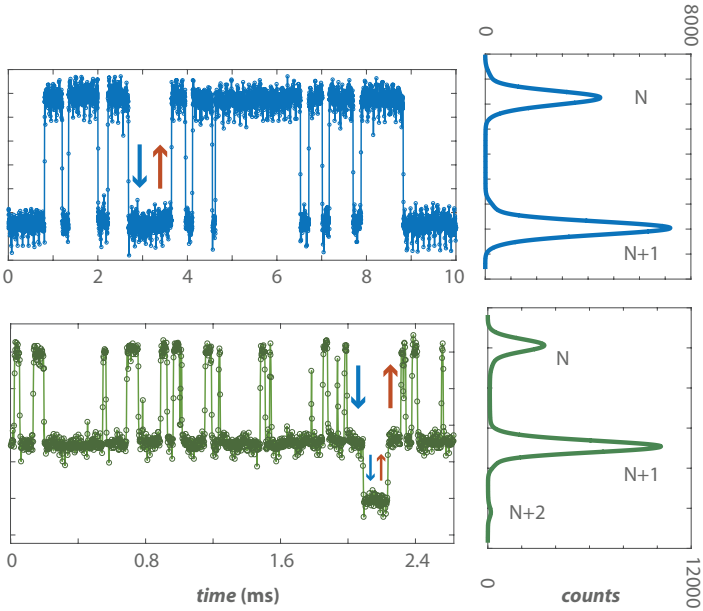

Figure 4.3: Current over time, traces of QPC measurements showing 2 and 3 energy levels of electron waiting state, with 'blue' and 'orange' arrows showing the tunneling in and out directions respectively. The distributions for each level on the right forms the process of identification of levels for each trace. For the bottom figure, with 3 level state distribution, we observe that for this particular trace, the distribution is very small for the state N+2 compared to the states of N, N+1, and the the distribution of N+2 state is very close to the noise floor, though the floor is very minimum.

1. The binary data is a current trace over time (Fig. 4.3). The data points however will have one or more than one range of values, with each range of value being distributed with a unique mean and variance

2. To identify the mean and the variances of the ranges, distribution of the whole set of data points are estimated for each file, and, in case the file size is very big, the distribution is taken along different chunks and compared for common mean and variances wherein a certain amount of tolerance for deviations is programmed out of long data observations and this takes care of any slight mismatch in the distributions between chunks along the whole long time trace

3. Once the distribution is fixed for the single data file, peak detection algorithm detect peaks from each distribution

4. From the identified peaks, the widths of the window boundaries on both sides of the peak are decided. Again, since one experiment involved changing the gate voltages while incrementing dot source-drain bias, the peaks of the distributions would always shift across each file and so the window edges. Also that the current traces would comprise of one, two or three levels creating, subsequent number of distribution peaks and windows. To automate the whole process of peak identification and windowing around the peaks, it necessitated, very sensitive and more controllable peak detection algorithm for this purpose (with about 6 controllable parameters whose tolerances had to be placed or varied according to the raw data)

5. Noise was issue in the experiment set involving thousands of files. While filtering process was involved (for the raw data, Savitzky-Golay method was used), it was very critical that the noise filtering process didn't alter the peak location more than certain set tolerance levels. Though, the noise filtering was not employed for all files, the files were always checked (programmatically) for the height of noise floor and if it exceeded set tolerance levels, the noise filtering process was automatically brought in

6. This point will be discussed in further detail in the next chapter, that, the choice of the window width around each peak was a critical choice in the final behavior of waiting time distribution at short time limits and that at short time limits, the limits of the detector bandwidth

become always visible where the distribution either shoots up or shoots down than the rest of the distribution

7. The above point is also due to the choice of one, two, or more than two individual data points being considered to count an unit of waiting time. This is important because, a single data point could be from transient noise from the measurement setup, or a fast event which could not be resolved due to the bandwidth of the detector though still recorded as a single point. Hence second to the choice of the size of window, this choice of counting minimum set of points for one unit of waiting time is critical to the whole counting process. In the next chapter we will see instances of counting single data point as one unit of waiting time yielding a very different distribution

8. Next the current level edges have to be identified correctly using the above information (points 4 through 7). It would be always possible that in the transition between two levels certain data points are left due to them being out of the windowed range for that particular and the next level, so it was always necessary to rightly approximate the transition edge of the current levels in the trace data. Other than this, it was also observed that spikes (comprising of less than minimum number of 'unit waiting time' data points) within each level had to be very correctly omitted and adjacent data points (around the spike) were correctly counted

9. Once the above steps are correctly undertaken, the waiting time for each trace (from single file or truncated part of large file) is calculated. In the case of large file with many truncated parts, the waiting times before and after the point of truncation are very diligently cross checked (programmatically) as it is possible that at point of truncation both the earlier and the later parts could be in the same state or in different state of energy (current), or points lost or gained due to approximation process of trace edges. Very slight errors at this part, after combining the truncated parts, did yield very different statistics and therefore the end observations and it often had been very tedious to locate source of data handling error from end statistical observation

10. From the waiting times distribution, to estimate the statistics of cumulants, the waiting times are counted in range of unit mean, to few ms large mean, time slots and their moments estimated and cumulants calculated

5 Full Counting Statistics

5.1 Motivation

This chapter discusses further idea of using counting statistics in the Coulomb blockade regime of the quantum dot, with experimental results of electron counting so obtained, through estimation of normal cumulants, factorial cumulants and waiting time distribution. We would also discuss waiting time distribution in terms of simulation experiments.

Parts of discussed text and figures would be similar to those presented (at places 'in verbatim') in the publications tentatively titled, 'Factorial cumulants in conditional tunneling regime in a single quantum dot' and 'Waiting time distributions in conditional tunneling regime in a single quantum dot'.

5.2 Effect of detector bandwidth

As we would further discuss the choice of statistical analysis as one tool to understand electron transport in quantum dots and 1D channels, we will have to understand the behavior of the detector which we started to understand in the last chapter. The detector introduces a certain lag (on its own) on the actual electron moving over the barrier. The current so forth measured at the detector would hence be lagging [120–123] with the reaction time (τ_d) of the detector, which is in fact an exponential suppression as,

$$\langle I \rangle_{\text{detected}} = \frac{\Gamma \cdot e^{-\Gamma \tau_d}}{2} \tag{5.1}$$

for symmetric barriers ($\Gamma_L = \Gamma_R = \Gamma$) here, which further can be given in terms of the distribution as [120–122, 124]

$$P(\tau_{(L,R)}) = \frac{e^{\frac{1}{2}(\Gamma_L+\Gamma_R+\Gamma_D+\Omega_{(L,R)})}(e^{\Omega_{(L,R)}\tau_{(L,R)}})\Gamma_D\Gamma_{(L,R)}}{2\Omega_{(L,R)}} \tag{5.2}$$

with,

$$\Omega_{(L,R)} = \sqrt{-4\Gamma_D\Gamma_{(L,R)} + (\Gamma_D + \Gamma_L + \Gamma_R)^2}$$

where again, the suffixes of D, R, L for the rates Γ, time τ represent corresponding values for the 'detector' the 'right' and 'left' barriers; $\Gamma_D = 1/\tau_d$. Figure 5.1 show the time evolution of the distribution the 'waiting times' of electron in the dot, 'before' and 'after' occupation of the dot with parameters as,

$$\Gamma_L = 28.990\,\text{kHz}$$
$$\Gamma_R = 10.320\,\text{kHz}$$
$$\Gamma_D = 500\,\text{kHz}$$

The lag due to the detector is visibly seen at the short time limits where the distribution tends rapidly towards 'zero'. The counting process for this representation made use of considering only three or more points as a unit waiting state, hence, the single and double data-point value distribution is not represented, which would nevertheless would have a dropping distribution towards zero (for this experimental data used in the calculation). At long time limit however, the distribution tends to be exponential. The model fits very aptly considering the fitting value for the detector used in the experiment here. The log scale helps representing the wide variation in the distribution very aptly. We also see that, the sum observed process is however not Poissonian due to the detectors manifestation on the real bandwidth of the tunneling process. The effective mean life could then be approximated as [120],

$$\langle\tau\rangle_{(L,R)} \approx \frac{\Gamma_D + \Gamma_L + \Gamma_R}{\Gamma_{(L,R)}\Gamma_D} \tag{5.3}$$

which is not simply $\langle\tau\rangle_{(L,R)} = 1/\Gamma_{(L,R)}$ value.

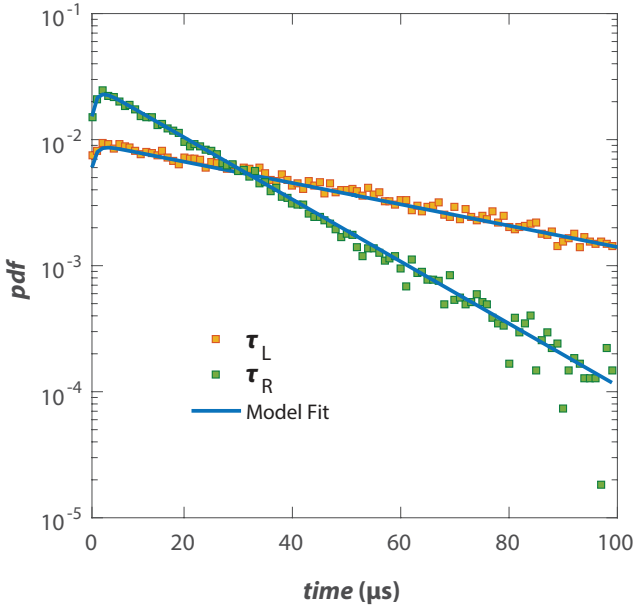

Figure 5.1: Waiting time distribution of tunneling event with two stable states, with the detector model fitting into the raw experimental data. We also observe how in very long time limit, the pdf falls rapidly and also creates outliers, implying the largest waiting times occur quite rarely, given a certain barrier width and thermal energies available at the dot-barrier system.

5.3 Time analysis of counted Electrons

5.3.1 Moments and Cumulants

Let us briefly revisit the idea of moments continuing from Chapter 1 again in this section with a brief mathematical connotation while trying to explain physics in the subsequent discussion. Here we have the simpler way to write a moment of an rth order about a point z, for a certain distribution F, using the Riemann-Stieltjes integral, would be,

$$\mu_{x^r} = \int_{-\infty}^{\infty} (x - z)^r dF \tag{5.4}$$

for random variable x with z about the mean or zero; where as, the rth moment about x in terms of rth and lower moments about another point z could be developed as,

$$\mu_r(x) = \sum_{j=0}^{r} \binom{r}{j} \mu_{r-j}(z)(x - z)^j \tag{5.5}$$

where again, x could be the mean of the distribution. The above two equations hold importance in discussions where we deal with grouped data, which is our waiting time data from the counting experiment. The grouped data offers the possibility for higher moments to be mathematically evaluated and possibly provided with a physical interpretation. Mathematically higher moments are always sensitive to fluctuations on the sampling process and possibly larger amount of errors. Further it is also possible to have a generating function or rather a moment generating function here from the distribution function (of the waiting times), which when expanded in powers of the time t, will give the moments as coefficients of those powers. Henceforth, if the frequency generating function is say, $F(t)$, the moment generating function would be $F(e^t)$.

Since our mathematical analysis would be on the probability distribution ($P(n,t)$) of event n in time t, an equivalent probability generating function would be useful to understand the mathematical evolution of the statistical analysis we shall discuss further, where the equivalent generating function is given as,

$$G(z, t) = \sum_{n=0}^{\inf} P(n, t) z^n \tag{5.6}$$

This idea allows one to treat any infinite sequence through the coefficients of the series. For our transport process, this is akin to the partition function in statistical mechanics which is equivalently written as product of

partition function of all the independent microstates, while the sum of all the probabilities each microstates occupy, equals 1. This is akin to normalization process of $\sum P(n,t) = 1$, which would also imply, $G(z = 1, t) = 1$, z called the 'counting field' being an arbitrary coupling field between the detector and the dot system [8]. For a long time limit $t \to \inf$, the logarithm lnG gets linear in time just like in a macroscopic / thermodynamic limit, the free energy (being $= k_B T Z$, the partition function) becomes linear in the volume of the system [8]. We see here the generating function of fundamental interest to evaluation of the whole transport process [consisting of any/all independent constituent sub-processes ($\xi(z) = \xi_1(z) \cdots \xi_k(z)$)], through factorization of the generating function. In terms of the moment generating function (as mentioned above), we will then have the generating function as,

$$M(z,t) = G(e^z, t) = \sum_n P(n,t) e^{nz} \tag{5.7}$$

This above description is akin to the Fourier transform of the probability distribution function P, in z.

As moments and cumulants are another set of constants which can give further information on the properties of the distribution and the system we can by taking the logarithm of the moment generating function (over its argument z), yield an irreducible set of correlation functions for the transport phenomena, called as cumulants [8]. In terms of power series [6] one can also conveniently write as,

$$exp\left[\kappa_1(t) + \kappa_2 \frac{t^2}{2!} + \cdots + \kappa_r \frac{t^r}{r!} + \cdots\right] = 1 + \mu_1 t + \mu_2 \frac{t^2}{2!} + \mu_r \frac{t^r}{r!} + \cdots$$
$$= G(t) \tag{5.8}$$

where, κ_r is the coefficient of $(t)^r/r!$ in $\log G(t)$, while μ_r is the coefficient of $(t)^r/r!$ in $G(t)$. Theoretically the idea of cumulants informs that they are invariant under change of origin, except the first (in contrast to moments about an arbitrary point) and any linear transformation of the kind $l\kappa + m$, leaves the cumulant unchanged (except the first, which is the mean).

We have therefore, the cumulants written as,

$$S(z,t) = \log(G(e^z,t)) \tag{5.9}$$

giving the mth cumulant by differentiating w.r.t z at $z = 0$ [125],

$$\langle\langle n^m \rangle\rangle(t) = \partial_z^m S(z,t) \mid_{z\to 0} \tag{5.10}$$

which develops into the set of cumulant definitions discussed in Chapter 1. Experimentally accessing P is more practical than G.

The theoretical work on using FCS for electrons tunneling through a conductor was pioneered by Levitov and Lesovik [54] and used the idea of scattering matrix to solve the problem of FCS of non-interacting electrons being transported through a conductor. Works of Pilgram and Nagev [126, 127] brought in ideas of FCS (evolution of third cumulant) being strongly influenced from transparencies at the contacts in a semi-classical regime. Evolution of FCS for interacting systems (Coulomb blockade regime) were discussed in [128–131], with the higher order moments and cumulants. The analytical properties of the FCS [132, 133] as functions of current, voltage, temperature, counting field (as a theoretical parameter) of the generating function of the probability distribution $P(n,t)$ has come to be of valuable interest since the transport process is essentially a function of all the independent, microscopic events and the generating function could be factorized according to these properties as pointed out in [134, 135].

Since cumulants have been the traditional way of deducing the FCS for characterizing the probability distribution $P(n,t)$, the fluctuations in cumulants have been the key idea to grasp any physical understanding of the underlying processes. The cumulants' fluctuation over time and other parameters of further investigation, would be further discussed in the next sub-sections. The cumulants for a non-Gaussian distribution have already been shown to oscillate as a function of any parameter in general (while temperature and magnetic susceptibility parameters are discussed below) in the works of Flindt et. al. in [103].

In the forthcoming sections on cumulants we will discuss the time evolution of normal cumulants as function of temperature fluctuation and varying magnetic susceptibilities on the quantum dot.

We had discussed the formulation of normal cumulants in Chapter 1, here we mention the cumulants or order n (in terms of central moments) as a binomial function of moments μ as,

$$C_n = \mu_n - \sum_{m=1}^{n-1} \binom{n-1}{m-1} C_m \mu_{n-m} \tag{5.11}$$

which upon expanding for the first four orders, yields,

$$\begin{aligned} C_1 &= \ll n \gg \\ C_2 &= <n^2> - <n>^2 \\ C_3 &= <(n - <n>)^3> \\ C_4 &= M_4 - 3{C_2}^2 \end{aligned} \tag{5.12}$$

where, M_4 is the 4th normal moment defined as, $M_4 = <(n - <n>)^4>$, for the distribution $P(n,t)$. The higher orders cumulants could be similarly inferred through expanding Equa. 5.11 in terms of higher order moments.

In terms of experimental data analysis, the histogram of electrons transferred through the barrier (as discussed in Chapter 4) essentially yields $P(n,t)$ and the idea of cumulants is developed analogously from the theory of k-statistics as developed in Chapter 12 of [6]. The idea of k-statistics proposes symmetric functions (k_1, k_2, $\cdot$, k_p) to characterize the distributions, and show the sampling cumulants could be obtained by combinatorial operations on these functions [6] (also as mentioned in Eq. 5.11). The idea remains same even for the discussion of factorial cumulants in the later sections.

The distributions of $P(n,t)$ are considered from the experimentally possible minimum to the experimentally possible maximum time limit while in the very long time limits, the discrete electron statistics turn up into (linear) continuous current statistics as $\ll I \gg \equiv \frac{\ll n^m \gg}{t}$, at $t \to \infty$. Discussions on cumulants and factorial cumulants in this work, are considered at zero-frequency limits which ideally means any information of interactions or correlations are averaged over the experimentally valid long times and the discreteness of electron transfers (resolvable at the detector's bandwidth limits of close to zero frequencies). Full counting statistics [52, 53, 87, 103, 136–144] had been so far remarkably utilized to understand higher order statistics of charge transfer distributions across the tunneling barrier

and the discussions in succeeding sections shall attempt to enhance this understanding. Of particular interest, is in using a comparatively newer idea in FCS, called as factorial cumulants to identify any discerning information in the transport statistics for example, the tails of the distribution in the log plot of Fig. 2.12. The idea that, voltage or current fluctuations were measurable [53, 141, 143] ideally by accounting the noise in the environment [52] paved ways to measure the distributions $P(n,t)$ [87, 137, 138] of tunneled charges circumventing the need to remove any environmental noises, heralded further ways to apply FCS to learn further through the higher moments and cumulants. The review works of [145, 146] and references therein, quite aptly sum the idea of applying the statistical techniques with charge detection and counting processes using QPCs in both single and double ([139]) quantum dots. Normal cumulants up to the 15th order have been worked upon in [103] using a single quantum dot.

We will also discuss 'waiting time distributions' again in the same frame of one another way of looking at charge transport. Discussions on cumulants and factorial cumulants are further taken up with references to different experiments discussed as follow.

5.3.1.1 Experiment-Set A: Cumulants vs. Temperature

The quantum dot is set to a fixed working point with a near constant rate for tunneling-in and tunneling-out of electrons. The switching current (as the QPC signal) is recorded at two different temperatures of base temperature (400 mK) and higher temperature of 1.3K at the quantum dot. The current traces are single switching events, indicating occupation of single free energy state within the dot's energy window for both the temperatures. While tunneling processes are compared, the quantity of tunneling asymmetry is of essential importance and it is defined as,

$$\alpha = \frac{\Gamma_{\text{out}} - \Gamma_{\text{in}}}{\Gamma_{\text{out}} + \Gamma_{\text{in}}} \tag{5.13}$$

where Γ_{out} and Γ_{in} are the tunneling rates for the tunneling-out and tunneling-in processes considering an unidirectional flow of current from the source to drain through the quantum dot. Asymmetry value is also an indicator of measure of the change in barrier transparency for the tunneling process between the two measurement. To compare two different tunneling processes, it is also essential that the transparency of the barrier is not

different so as to rightfully observe the effects of temperature rather than that of the barrier transparency affecting the statistics.

For this experiment we have the following observations for 1.3 K temperature,

$$\Gamma_{\text{in}} = 48.45\,\text{kHz}$$
$$\Gamma_{\text{out}} = 17.61\,\text{kHz}$$
$$\alpha = -0.47$$

while for 400 mK temperature,

$$\Gamma_{\text{in}} = 40.22\,\text{kHz}$$
$$\Gamma_{\text{out}} = 10.79\,\text{kHz}$$
$$\alpha = -0.57$$

The temperatures were inferred through the vapor pressure of He3 at the He3 insert since it was intentional to bring as minimum heat possible through any other sensors and measurement signals and avoid the use of extra wires supposedly for sensors.

Figures of 5.2, 5.3 plot the normal cumulants (standardized or 'normalized over the first cumulant') evolving over a period of time, so obtained from the two temperature measurements. The solid lines represent data for higher temperature while the dashed line represent data for base temperature measurement. If we consider the ratios of the cumulants themselves for the respective higher and lower temperature (the ratio for the cumulants without having been normalized), we see from Fig. 5.4 that, for the ratio of the first cumulant, the ratio stays to near constant value over time and the value is not 1 but, > 1 (the constant value being 1.5 with changes starting from 4th decimal position at longer times). This does indicate that the mean of the distribution has shifted to higher value for the higher temperature, indicating that we have larger average number of tunneling events at the higher temperature. While this increases the tunneling rate,

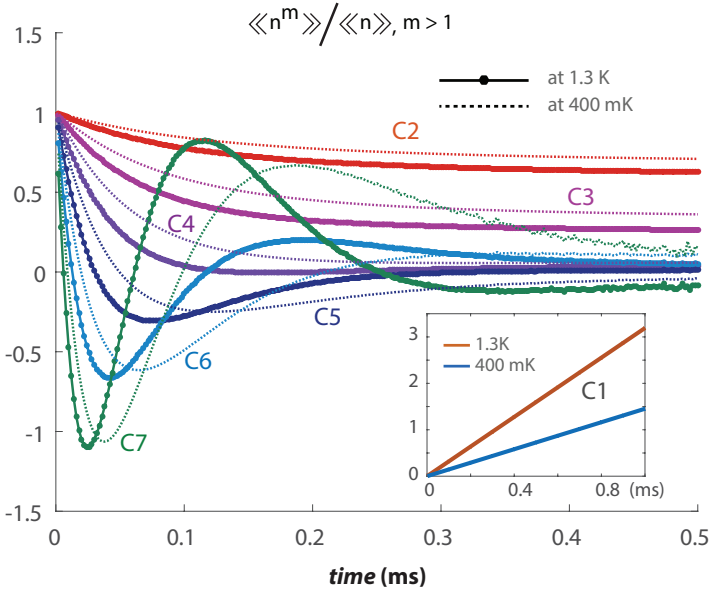

Figure 5.2: Time evolution of first seven cumulants for two different temperatures. The cumulants shown are normalized over the mean current (first cumulant). Solid lines are for higher temperature and dotted lines for base temperature measurements. The inset shows the first cumulant.

for a fair comparison of the temperature effects, the tunneling asymmetry was kept close to similar value (as mentioned above).

We observe from Fig. 5.4 that, apart from the mean becoming higher, we also observe the second and third cumulant ratios are higher than 1. This would mean that, the extent of spread from the mean position gets higher at the higher temperature, for the smaller waiting times as plotted in the figure. More events occur at the lower time limit when the temperature is high.

We do observe the higher temperature has brought in certain visible (if not very dramatic) change of statistics into the cumulants. The distribution for both the set of data is plotted in Fig. 5.5. The asymmetry being close

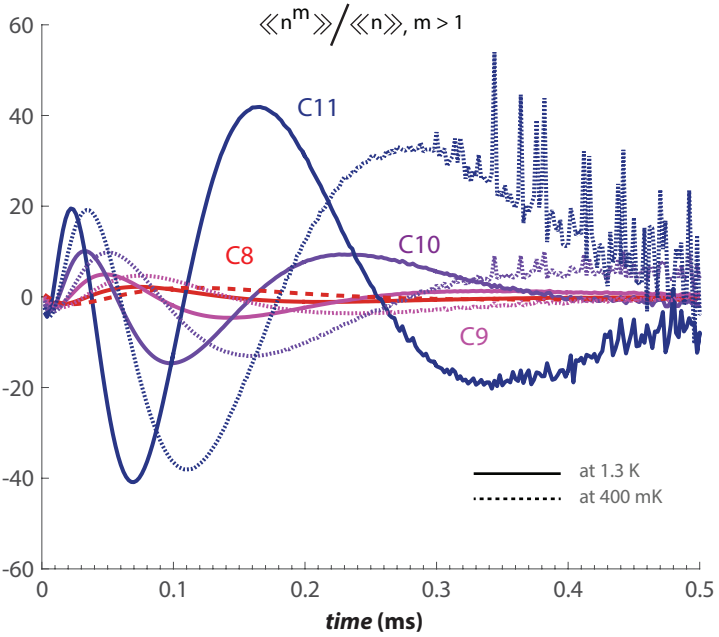

Figure 5.3: Time evolution of eighth to eleventh cumulants for the two different temperatures. The cumulants shown are normalized over the mean current (first cumulant). Solid lines are for higher temperature and dotted lines for base temperature measurements. The inset shows the first cumulant.

to similar for both temperature measurements (the closest so obtainable experimentally in this situation), at the higher temperature we do not expect any different tunnelling scenario except that in absolute terms the tunnel coupling is higher at both directions at higher temperature and we expect the higher temperature to bring in higher occupation states into the quantum dot, which would offer higher probability for the tunneling electrons to occupy those states and tunnel through the dot. While this increases the rate, it also effectively does not allow electrons to wait for longer time at the dot before tunneling out, indicating shorter waiting times. This is clearly observable in Fig. 5.5 with comparatively higher distribution at the shorter time limit; while the waiting time distribution at

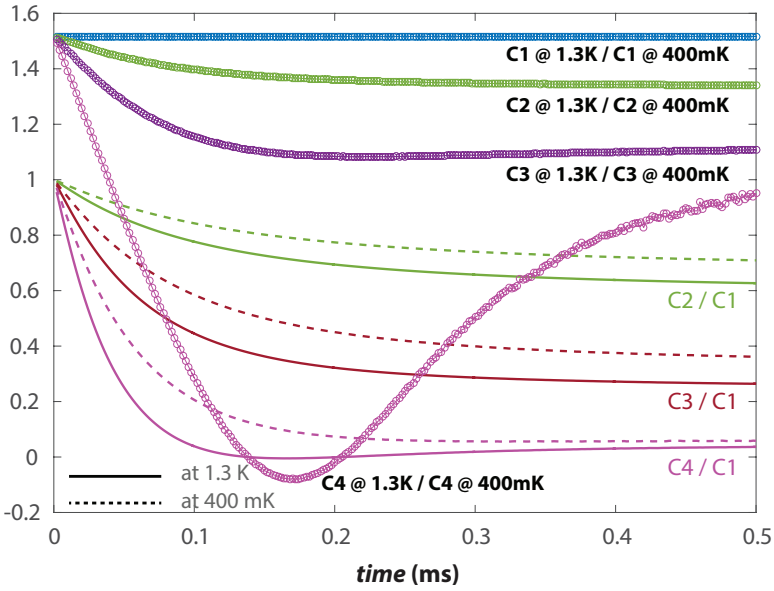

Figure 5.4: Ratios of the first through fourth cumulant for higher-temperature to base-temperature, are shown as respectively colored circles. The ratio of C1 for the two temperatures is shown in blue-circle (which is a constant 1.5), while that for C2 through C4 are shown in green, dark-brown, purple circles. The ratios of the cumulants are taken from the non-normalized values of the respective cumulants, to isolate any influence of the first cumulant in the understanding of the comparison. The solid and dashed lines for C2, C3, C4 are the normalized respective cumulants for the two temperatures, as shown in figure of 5.2 respectively.

the medium to longer time limit is appreciably much lower than that at the base temperature.

Further, higher temperature would bring in excited states into the energy window at the dot, and while, electrons could occupy these states, they would as well quickly decay into the nearest ground state [[147]] and ideally the tunneling would happen from that ground state. We do expect this to

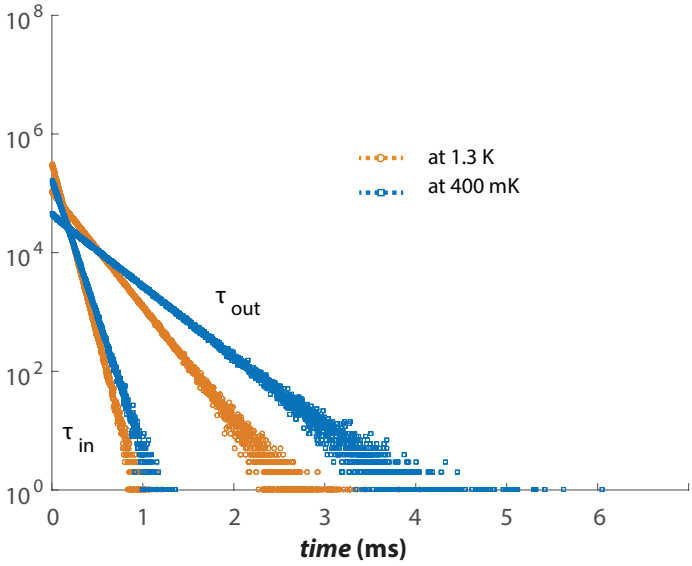

Figure 5.5: Distribution of waiting times for the experiment for the two different temperature. We see how for very long time limits the distribution becomes rarified and spreads at the bottom of the distribution. The distribution does show small differences for the two measurements at different respective temperature, at smaller and very long time limits.

happen continuously but these events are not detectable from the current experimental setup. The measurements basically see the transitions involving purely the ground states at the dot.

We hence show that, higher temperature does alter the statistics of tunneling electrons through single-dot measurements and these changes are observably classical in nature. The use of double-dots with much smaller size geometry and with a very fast detection setup, would dramatically give better picture of actual unidirectional flow and clear involvement of kind of occupation states involved in the tunneling process as the temperature would increase from base to higher values.

5.3.1.2 Experiment-Set B: Cumulants vs. Temperature vs. Asymmetry

We further evaluate the the dot system while we are continuously varying the asymmetry parameter by varying the voltages at the gates G1 and G2 (ref. Fig. 3.10)[G1 was varied from 422.5 mV to 880 mV and G2 was varied from 163 mV to 158 mV, while G3 was set at 113.1 mV]. Counting measurements were performed at different temperatures, and the asymmetry was varied at each temperature value.

The asymmetry values at temperature of 2 K, changed from 0.11 to 0.54; for temperature at 1 K, α changed from 0.32 to 0.73; for temperature at 700mK, α changed from 0.38 to 0.75 and; for the base temperature of 400 mK, α changed from 0.43 to 0.76.

Work on universality of cumulant oscillations were discussed in [144], wherein the cumulants oscillated with no special binding on the asymmetry parameter. Figures 5.6 and 5.7, show how the cumulants evolve at one particular temperature, with the varying asymmetry. For a particular temperature, the waiting times from each stepped asymmetry condition were counted into single distribution and the cumulants were evaluated. This way allows one to identify if the varying asymmetry condition could influence the total distribution and hence any particular behaviour in the oscillations of cumulants.

We do not observe any significant change in the pattern of time evolution of the oscillations even for one particular temperature, the asymmetry has changed. A reasoning similar to that discussed for Set-A experiments, could be made wherein, the positive change in asymmetry is manifested through the gradual opening of one of the tunnel barriers. This process does rearrange the dot levels but owing to the bias through the dot at close to 0.5 mV, though, slightly more positive from 0 V to aid uni-directional transport, the occupation level in the dot always stays single. The increase of temperatures though brings in higher coupling with the barrier contacts, the asymmetry value being similar across temperature, the statistics just varies as discussed in Set-A earlier, but, the stochastic nature is preserved and no other dramatic observation is made.

The randomness (stochastic nature) in the waiting times do not get influenced for any one particular temperature, though it should be mentioned that our measurement system is limited to probing of events at close to DC to few kHz frequencies and any possible bunching process that may happen

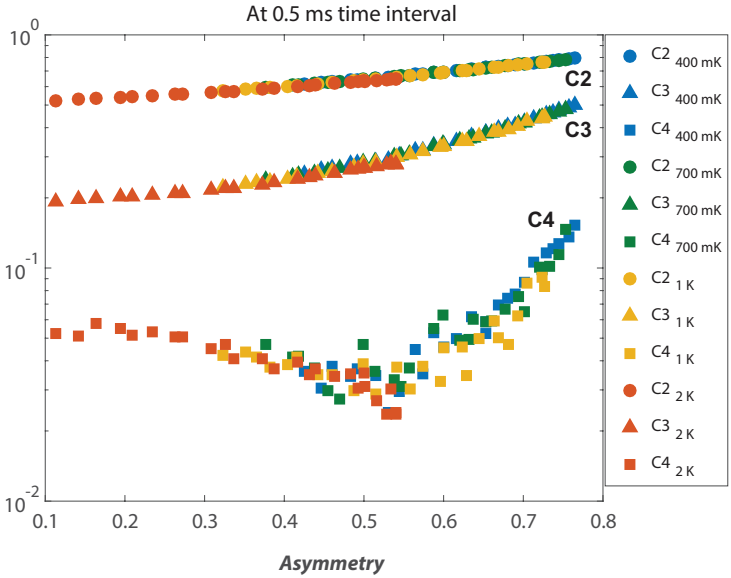

Figure 5.6: Semi-log plot of cumulants 2nd through 4th (normalized over the first) vs. Asymmetry, for a time interval of 0.5 ms. Refs. [125, 144] explain the universality of the oscillations of 15th order cumulant with respect to both asymmetry and dimensionless time (Γt) quantities. Here the first four orders are plotted with respect to asymmetry for different temperatures to show that, the stochastic nature of tunneling process is not altered and is universal with respect to change of asymmetry at different temperatures.

at high asymmetry and high kinetics (from very quick tunneling process) condition or through co-tunneling [148–151] and, would still be recorded in the combined time resolution of our system's measurement apparatus.

5.3.1.3 Experiment-Set C: Cumulants vs. Transverse Magnetic Field

In this experiment the quantum dot was evaluated for the influence of magnetic field with the field passing perpendicularly through the dot-detector system, at the base temperature and at gate voltages of G1 at 320 mV, G2 at 147 mV (G2 barrier nearly closed, while for 3T field, G2 was increased to

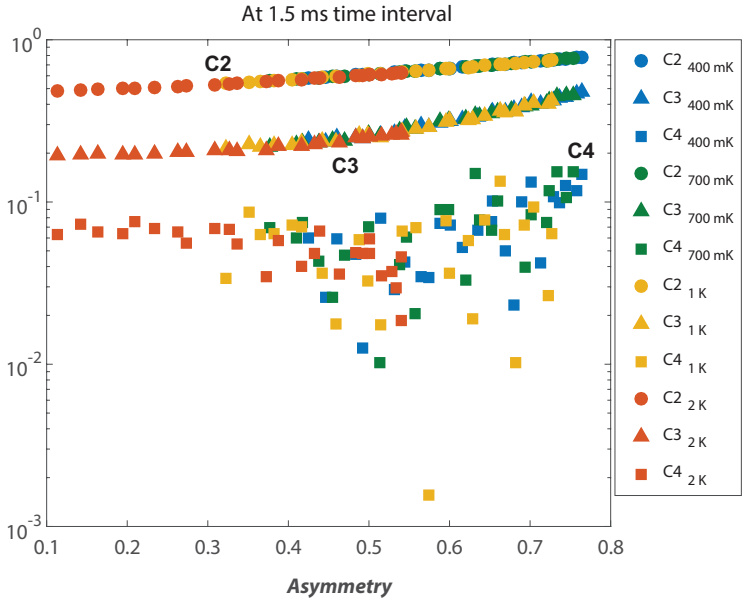

Figure 5.7: Semi-log plot of cumulants 2nd through 4th (normalized over the first) vs. Asymmetry, for a time interval of 1.5 ms. Refs. [125, 144] explain the universality of the oscillations of 15th order cumulant with respect to both asymmetry and dimensionless time (Γt) quantities. Just like the previous figure, 5.6, with the longer interval of counting the tunneling events, the stochastic nature of tunneling process is still not altered and is universal with respect to change of asymmetry at different temperatures.

132 mV) and G3 at 125 mV. The experiment is discussed for magnetic fields of 1, 2 and, 3 T, all measured at base temperature.

The asymmetry values maintained to similar values and were for 1T, 2T and 3T fields at $\alpha = 0.30$ ($\Gamma_1 = 8.943 \times 10^4$ Hz, $\Gamma_2 = 1.681 \times 10^5$ Hz), $\alpha = 0.28$ ($\Gamma_1 = 4.608 \times 10^4$ Hz, $\Gamma_2 = 8.136 \times 10^4$ Hz) and $\alpha = 0.25$ ($\Gamma_1 = 1.166 \times 10^4$ Hz, $\Gamma_2 = 1.928 \times 10^4$ Hz) respectively.

The presence of magnetic field ideally lifts the spin degeneracy due to which we do expect suppression of conductance due to spin-blockade which

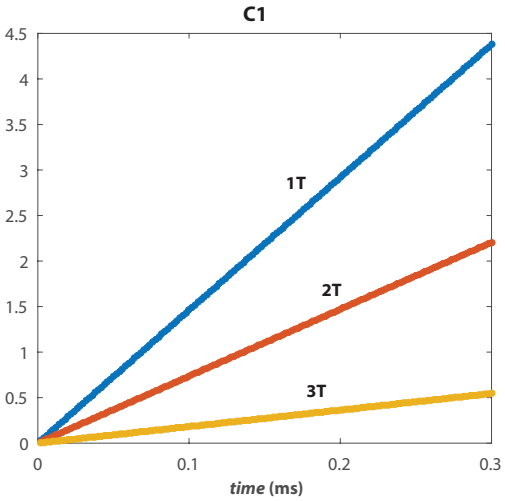

Figure 5.8: Time evolution of the first cumulant for magnetic fields of 1T, 2T and, 3T at base temperature.

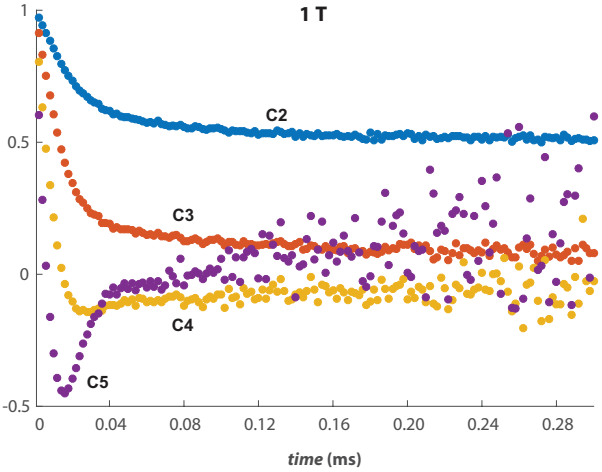

Figure 5.9: Time evolution of 2nd through 5th cumulant (normalized over the first) for magnetic fields of 1T at base temperature.

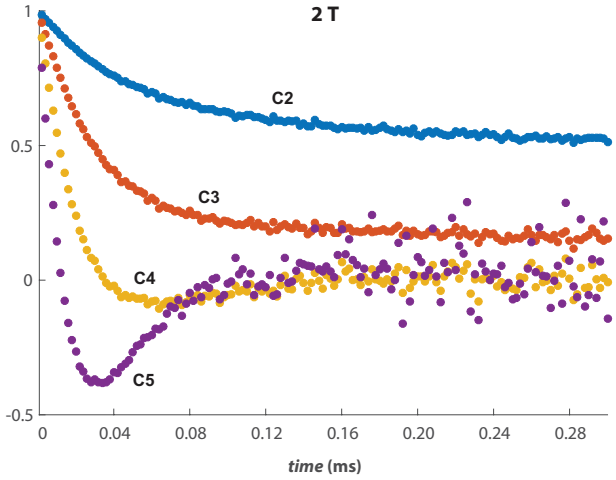

Figure 5.10: Time evolution of 2nd through 5th cumulant (normalized over the first) for magnetic fields of 2T at base temperature.

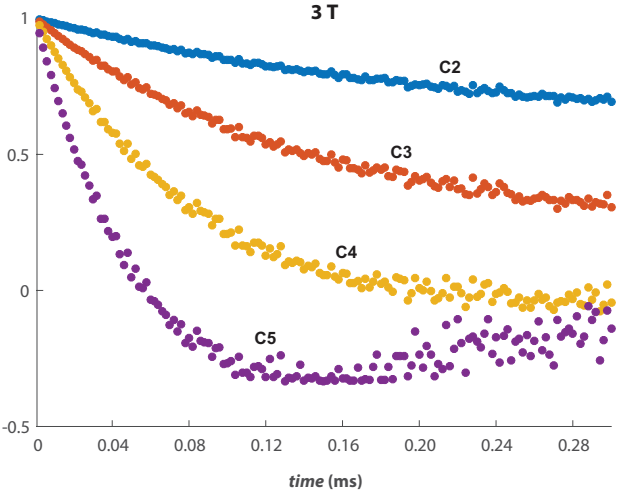

Figure 5.11: Time evolution of 2nd through 5th cumulant (normalized over the first) for magnetic fields of 3T at base temperature.

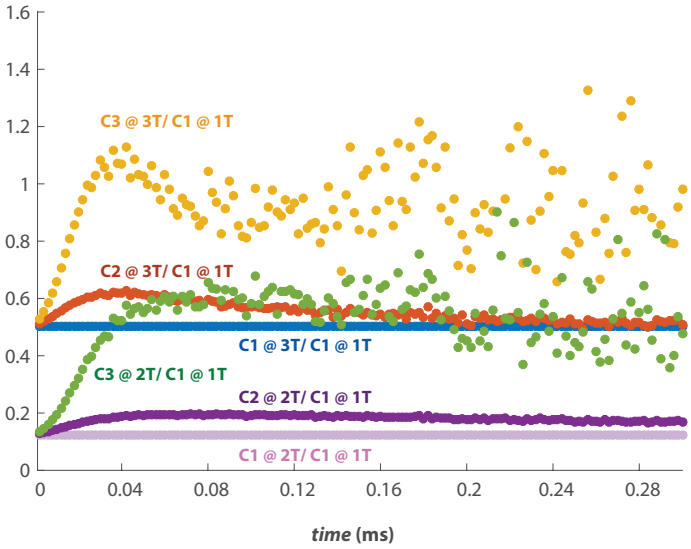

Figure 5.12: Ratios of 1st, 2nd and, 3rd cumulants with respect to magnetic fields of 2T/1T and 3T/1T, at base temperature. The ratios were taken for the non-normalized cumulant values for each magnetic field, so as to avoid influence of the mean current (first cumulant), in understanding the change in cumulant values as magnetic field increased. We observe how at higher magnetic fields the cumulants magnitude is suppressed (at each time position).

would be at its dominant at 3T compared to 2T and 1T fields. Influence of magnetic field assumes importance to the study of FCS owing to the various electron coupling possible through spin interactions [102, 152–159]. In this experiment nevertheless, the stochastic nature of electron tunneling through the tunneling barrier remains and the only difference the magnetic field brings in is an altered distribution of tunneled events through the barrier, through the suppression of distribution. The cumulants show suppressed oscillation at higher magnetic field markedly visible for higher order cumulants.

Figures 5.8, 5.9, 5.10 and 5.11 show the time evolution of the first five order cumulants for the three magnetic fields at base temperature. For the current observation, the length of measurement for time trace was about

1 min. and the Fano factor (2nd cumulant over the 1st cumulant) does not show any effects of the magnetic field which could be the first most visible observation for operating the dot and evaluating the FCS in the Kondo regime (through change in the tunneling statistics from any magnetic exchange couplings happening at the dot or across the barrier at higher bias or temperature). The Zeeman energy ($g\mu_B B \approx 25\,\mu\text{eV/Tesla}$, for $g \approx 0.4$) is much smaller than the single level spacing (see Chapter 3 for details) and is also $\leq k_B T$. This along with the small unidirectional dot bias just allows a single state occupation in the dot. The temperature also brings in a certain tunnel broadening at both the barriers and the non-ferromagnetic leads does not allow any spin exchange to happen with the leads. We do not expect the Fano factor to get values more than 1 (as an indication of super Poissonian transport owing to any transport happening in groups of electrons due to any coupling across the barrier) in this situation (and of investigation at DC - few-kHz frequencies), though the conductance through Coulomb blockade does gets suppressed through spin-blockade at the higher magnetic fields (the mean current - first cumulant, is suppressed as the magnetic field increases). Figure 5.12 shows the ratio of 1st, 2nd and, 3rd cumulant for magnetic fields at 2T vs. 1T and 3T vs. 1T. The ratios for the 2nd and 3rd cumulants were considered for non-normalized values of individual 2nd and 3rd cumulants at the respective fields. We observe that all the ratios are less than 1, for considerable time until the inherent noise (due to limited length of the data) overtakes the trend of the behavior. We see that, the mean current is suppressed by about 15 % at 2T from 1T field, and further suppressed by about 50 % at 3T going from 1T field. Second and third cumulants are as visibly shown to be reduced too. As we had seen the suppression due to spin-blockade mechanism, alters the statistics.

For this experiment the dot-bias was not swept through zero value at the presence of magnetic field and hence it remains interesting (still at DC - kHz frequencies), how the use of ferromagnetic leads and also a zero-bias anomaly affects the behavior of cumulants at close to zero bias condition of the quantum dot. At the QPC (detector) the presence of magnetic field tends to improve the quantization through reducing the amount of back-scattering (also see Chapter 2) happening at the point contact (even if the potentials at the QPC would not be completely adiabatic [160]).

5.3.1.4 Experiment-Set D: High dot bias condition

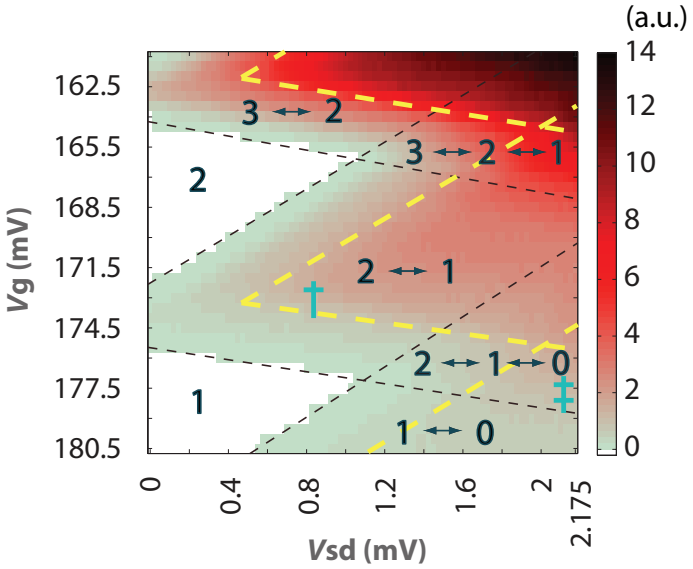

Figure 5.13: V_{SD} vs V_{G2} plot for the positive source-drain bias of the quantum dot. Refer text for description and explanation on various annotations.

The sample (from Fig. 3.10) [104, 161, 162] with the AFM oxidised barriers forming tunneling channels across both sides of the quantum dot, was subjected to source-drain bias sweep from -2.2 mV to +2.2 mV DC (in 25μV steps), while the gate G2, was stepped and opened gradually as shown in Fig. 5.13. Figure 5.13 shows the region of positive bias of the result (in the form of QPC mean current or the first cumulant as evaluated from the QPC current, as one of the channel was stepped through the bias). The electron temperature was inferred through the Coulomb blockade widths at zero bias (for FWHM $\propto 3.5k_BT$, accounting for a certain bias offset close to zero bias), and was found to be approximately, 800mK. In the figure, the dot is opened as the gate (G2) voltage decreases. Gate G1 voltage was appropriately set to allow for single tunneling events (in our sample device, gate G1 had gotten electrically weak due to aging and it was continuously

compensated accordingly). Further, the dot bias is also increased, offering further stable occupation states for the electron at the dot.

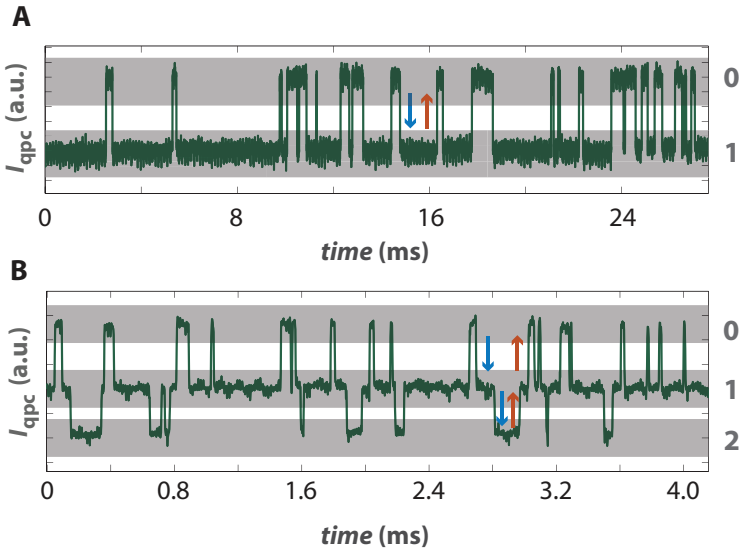

Figure 5.14: Time traces of current switches observed from the positions of 'single blue' (A) and 'double blue' (B) dagger points of Fig. 5.13. Arrows show the direction of current flow, i.e, the electrons are switching occupation states as $0 \rightarrow 1$ and $0 \rightarrow 1 \rightarrow 2$ as they fill the states and then empty thereafter one state at a time, unidirectionally, with $0, 1, 2$ being the occupation states.

Figure 5.13 highlights regions of low and high current regions. The pale yellow dashed line represent the region of an abrupt increase in the current from the region represented by the black dashed line. The abrupt current increase (marked as prominent presence of red colored values) is ascribed to the presence of first excited state becoming available in the energy window for the electron to occupy during the transport process. Following the discussion from Section 2.3.2, we do observe an excited state that is also visibly broadened (possibly due to presence of a continuum of excited states, made available through the large bias situation at the gate and the dot,

while the electrons tunneling through this continuum, would only take up the lowest state in the energy window). Regions 1 and 2 denote the Coulomb blockade region and the figure also shows regions of two and three stable states of electron occupation in the dot.

As bias increases, and electrons are able to occupy single or two occupation states (giving two or three stable configurations respectively, as shown in Fig. 5.13) and, the QPC current registers switches representing the respective stable configurations as shown in Fig. 5.14 (here we observe two plots of QPC currents with single and double switches respectively). These two plots also correspond to regions represented by single and double blue daggers of Fig. 5.13 respectively.

We can further infer from the both the plots of Fig. 5.14 on how the waiting times for the electrons in each stable state are distributed. The length of each waiting time is a random length due to the stochastic nature of the tunneling process. This gives us a Poisson behavior for the distribution. The smallest point from the time trace is of 2µs (discussed in Chapter 3). The figures of 5.13 and 5.14 from this experiment are further discussed in the next section of factorial cumulants.

5.3.2 Factorial Cumulants

Figure 5.14 represents regions of single and double occupation states for electron(s) to occupy inside the dot, at different gate voltages. We shall discuss these observations through the evaluation of factorial cumulants rather than non-factorial (normal) cumulants as in the previous sections since, the idea of factorial cumulants brings in additional information on the idea of possible Coulomb interactions in the Poissonian processes that we expect to observe happening across the tunnel barriers while involving more than one occupation levels inside the quantum dot.

We shall try to understand the experimental results through a short mathematical introduction to factorial moments and cumulants. The factorial expression [6] for a variable s is conveniently described as (with an analogy to power law, s^r),

$$s^{[r]} = s(s-h)(s-2h)\cdots s-(r-1)h$$

or rather taking the first difference with respect to s with unit h we will have,

$$\begin{aligned} \Delta s^r &= (s+h)^r - s^r \\ &= (s+h)s(s-h)\cdots s-(r-2)h - s(s-h)\cdots s-(r-1)h \\ &= rs^{r-1}h \end{aligned}$$

which could be compared to the equation in differential $dx^r = rx^{r-1}dx$. Conversely we will have,

$$\sum_{s=0}^{\infty} s^{[r]} = \frac{1}{(r+1)h}(s+h)^{[r+1]}$$

which would correspond to the rth factorial moment about an arbitrary origin a as [6],

$$\mu_{[r]} = \sum_{j=-\infty}^{\infty} s_j^{[r]} f(s_j) \tag{5.14}$$

with the summation (rather than Stieltjes integral) indicating the idea that the factorial moments are ideally useful for discontinuous distributions or continuous distributions [6, 7]grouped in intervals of width h and $f(s_j)$ being the distribution of s_j.

The factorial moments as defined as derivative of the factorial moment generating function would be [47] in terms of ordinary moments defined as,

$$< n^m >_F (t) \equiv \partial_z^m M_F(z,t) \mid_{z\to 0} = < n(n-1)\cdots(n-m+1) >$$

where, $M_F(z,t) = G(z+1,t)$ is the factorial moment generating function, alike the ordinary moment generating function discussed in the previous section.

We see the usefulness of employing factorial moments and factorial cumulants with reference to Fig. 2.11-2.12 where a certain Poisson process (with discrete distribution) with a certain rate Γ was not fitting with the Gaussian (continuous) distribution. This idea [47] can be further illustrated, if we

consider Equa. 2.51 (from Chapter 2) which in terms of the processes from Fig. 2.11 and 2.12 would yield for the Poisson process as (as a physical limit for the rare discrete process),

$$P(n,t) = \frac{\Gamma t}{n!} e^{-\Gamma t}$$

with the corresponding generating function as $G(z,t) = e^{\Gamma t(z-1)}$. This would give cumulants for the Poisson process as,

$$\ll n^m \gg (t) = \Gamma t$$

which for factorial cumulants $\ll n_F^m \gg (t)$ is zero (ideally it $\to 0$, which is visible at shorter time limits) for $m > 1$ (for Poissonian processes, Fano factor $= \langle\langle N^2 \rangle\rangle / \langle N \rangle = 1$, and have non-zero normal cumulants for order $m > 2$); hence the idea of factorial cumulants become important in the discussions of discrete processes in a possibly interacting system where the evaluation of factorial cumulants can reveal any deviations from pure Poisson statistics (just as normal cumulants would show deviations from pure Gaussian statistics). Figure 2.11 highlights this difference in the tails of the Poisson and Gaussian processes (in the log plot) and factorial cumulants of order $m > 1$ would be non-zero for deviating from Poisson statistics (Fig. 2.11).

In general, we could consider the factorial moments for a grouped data with distributions (frequencies) f_1, f_2, $\cdot\cdot$, f_n be given by the progressive summations, for the first four factorial moments as,

$$\mu_{F1} = \frac{\sum_{j=1}^{n} \{j f_j\}}{\sum f_j}$$

$$\mu_{F2} = \frac{\sum_{j=1}^{n} \{j(j-1) f_j\}}{\sum f_j}$$

$$\mu_{F3} = \frac{\sum_{j=1}^{n} \{j(j-1)(j-2) f_j\}}{\sum f_j}$$

$$\mu_{F4} = \frac{\sum_{j=1}^{n} \{j(j-1)(j-2)(j-3)f_j\}}{\sum f_j} \tag{5.15}$$

where the summation is divided by the total frequency $\sum f_j$. This way of summation and dividing by the total frequency has been the norm of calculating the factorial moments for all the experimental data discussed in this section.

Analogous to the discussions of ordinary moments and cumulants discussed in the previous section, here the factorial cumulants could be defined as the coefficient of $t^r/r!$ in the expansion of the logarithm of the factorial moment generating function [6, 47] as,

$$S_F(z,t) = \log[M_F(z,t)]\text{i.e,}$$
$$\ll n^m \gg_F (t) \equiv \partial_z^m S_F(z,t) \mid_{z\to 0} = \ll n(n-1)\cdots(n-m+1) \gg$$

While in the preceding section we witnessed how the normal cumulants have been oscillating, it has been not possible to extract any further information on physical processes (ideally the processes could be hiding in the oscillations) leading to the statistics other than the universality of the oscillations as discussed before. The idea brought by Abanov and Ivanov [163, 164] that, for noninteracting fermions through a two-terminal system would be a "generalized binomial" (also in [165]) and that the charge transfer process could be factorized into the individual charge events while the idea that the 'zeros' of the generating function would lie on the negative real axis. Theoretically the idea 'zeros of the generating function' stem from the mathematical operation of finding determinant in terms of spectral properties of operators whose eigenvalues give transmission probabilities of elementary charge transfers. The mathematical treatment of the subject is beyond the scope of this work and hence is referred as zeros and its likelihood of it not confining purely in the negative real axis of the complex plane indicates interactions in the fermionic system.

The treatment of zeros is not taken further in this work for the reasons that, its calculations in comparisons to results offered by factorial cumulants were not straightforward to calculate and understand within the discussions of the theoretical model discussed by Kambly et. al. in [125], which otherwise

forms the framework for discussing factorial cumulants characterizing our experimental data.

Factorial cumulants which have not been yet treated widely in the realm of FCS in mesoscopic physics is shown to provide an alternate view compared to ordinary cumulants to characterize the probability distribution $P(n,t)$ of the charge transport processes. Though works of [166–168] discuss factorial cumulants numerically in the realms of photons statistics through a QPC, entanglement entropy at QPC and in realms of spin degenerate quantum dot coupled to normal lead and spin non-degenerate quantum dot coupled to ferromagnetic lead respectively, the idea that they can characterize Coulombic interactions in an actual experiment of a simple two-terminal quantum dot with normal lead form the core of our discussions below.

Kambly et. al. have discussed in their work of [125] that, the binomial statistics that being characterized by factorial cumulants show that for noninteracting systems, the higher order factorial cumulants will not oscillate with any parameter (unlike the normal cumulants we observed in previous section). Our experiment just deals with the parameter of 'time' evolution of the factorial cumulants. Contrarily, if the higher order factorial cumulants oscillate as a function of some parameter ('time' in our experiment), the idea of 'generalized' binomial statistics is violated and it is hence a cause due to electron 'interactions' happened at the dot.

The expression of the generating function being factorable into independent elementary particle events, from [125, 163, 164], is mathematically given as,

$$G(z,t) \underset{\text{binomial}}{\overset{\text{generalized}}{=}} z^{-Q} \prod_i G_i(z,t) \tag{5.16}$$

where, $G_i(z,t) = 1 - p_i + p_i z$ is the expression for the binomial generating function corresponding to single elementary charge transport occurring with a probability $p_i \leq 1$. This generating function depends on 'time' as well as other parameters the system provides. The factor z^{-Q} equals 1 for an unidirectional transport, which is the experimental situation in our discussions. This factor corresponds to a deterministic background charge transfer with $Q = \sum_i p_i - \langle n \rangle \geq 0$ [125], with $\langle n \rangle$ being the mean value of the total transferred charge and $Q = 0$ for unidirectional transport.

Discussions in this section attempt to explain Coulombic interactions, influencing the stochastic processes across the barrier which further influence the

probability distribution $P(n,t)$, become visible through factorial cumulants unlike in ordinary cumulants.

The factorial cumulants from the experimentally obtained moments (as explained above), are further evaluated (as in terms of ordinary moments) for the first four orders (from Equa. 5.11) as,

$$F_1 = \mu_1 \tag{5.17}$$

$$F_2 = \mu_2 - F_1^2 \tag{5.18}$$

$$F_3 = \mu_3 - F_1^3 - 3F_1F_2 \tag{5.19}$$

$$F_4 = \mu_4 - F_1^4 - 6{F_1}^2F_2 - 4F_1F_3 - 3{F_2}^2 \tag{5.20}$$

The evaluation of factorial cumulants further than first four orders is not considered for want of very long time trace data, which as discussed in Chapter 4, amplifies noise at higher orders if the data length is short and it becomes impossible to learn further about the time behavior of factorial cumulants at higher orders. Additionally, the first four orders have been very sufficient to discuss the experimental observations characterized through factorial cumulants.

The figure of 5.13 shows two observations of importance, which we will continue to discuss further. First observation is, as shown by 'blue' daggers, with 'single' dagger positioned at the region of single occupation state in the dot, ultimately allows two possible stable states of electrons inside the dot. This single dagger position is highlighted by the time trace of Fig. 5.14A, which clearly shows current switches between occupied state (marked as '1') and unoccupied state (marked as '0'). We will further call this situation of time trace as 2-level system. The blue 'double' dagger is positioned at the region of 'high-bias' where the possibility of two-occupation state in the dot arises. This position is highlighted by the time trace of Fig. 5.14B, of current switches in states marked by '0', '1' and '2'. The dot offers states of '1' and '2' for two electrons to occupy in the region marked in Fig. 5.13 with two occupation probabilities and three stable states for the electrons inside the dot. We would further call this situation of time trace as 3-level system. The second observation is the near-stepped (though seen as a continuum, but with a certain marked step) increase of current in Fig. 5.13 shown as 'red' region and marked through 'yellow' dashed line. This line marks the availability of the first excited state in the transport window along the edges

of the 'black' dashed line, which denotes the ground occupation state. We will discuss this situation in terms of tunneling rate that we observe through the either barriers across the dot.

The figure of 5.13 was generated through 4040 data positions and for a unique dot bias and gate-G2 bias, time traces were measured for each of this position. The time traces varied from few hundred to up to about 2 million events per recorded trace of few seconds each, as both the biases were varied. Factorial cumulants were evaluated for each of this unique position.

The blue 'single' dagger of Fig. 5.13 position was observed for the dot bias of 0.85 mV and gate-G2 bias of 173.5 mV. The factorial cumulants evaluated at this point is shown in Fig. 5.15 as 'red' points. The data points get more scattered at longer times, owing to the short time trace data. The time evolution is hence calculated for up to 0.5 ms time.

Equation of 5.16, with single elementary probabilities of p_i, is evaluated for factorial cumulants as [125],

$$\ll n^m \gg = (-1)^{m-1}(m-1)!\left[\sum_i p_i^m - Q\right] \tag{5.21}$$

where, $Q = 0$ for our case of uni-directional transport. The factorial cumulants here alternates signs with respect to the order m as $(-1)^{m-1}$ (the statistics being generalized binomial). This expression is further theoretically evaluated (and discussed in [125]) as,

$$\ll n^m \gg = < n^m >_F - \sum_{k=1}^{m-1} \binom{m-1}{k-1} \ll n^m \gg < n^{m-k} > \tag{5.22}$$

with $< n^m >_F$ being the mth order factorial moment.

This idea is immediately observed in the figures of 5.15 for the experimental data ('red' points). The theoretical fits from the model as observed from the expressions discussed above (also in 'Appendix' of the work of D. Kambly [125] along with the idea of 'detector' in their calculations) is shown in 'blue'. The fits were determined by Mathematica codes provided by D. Kambly from her aforementioned work.

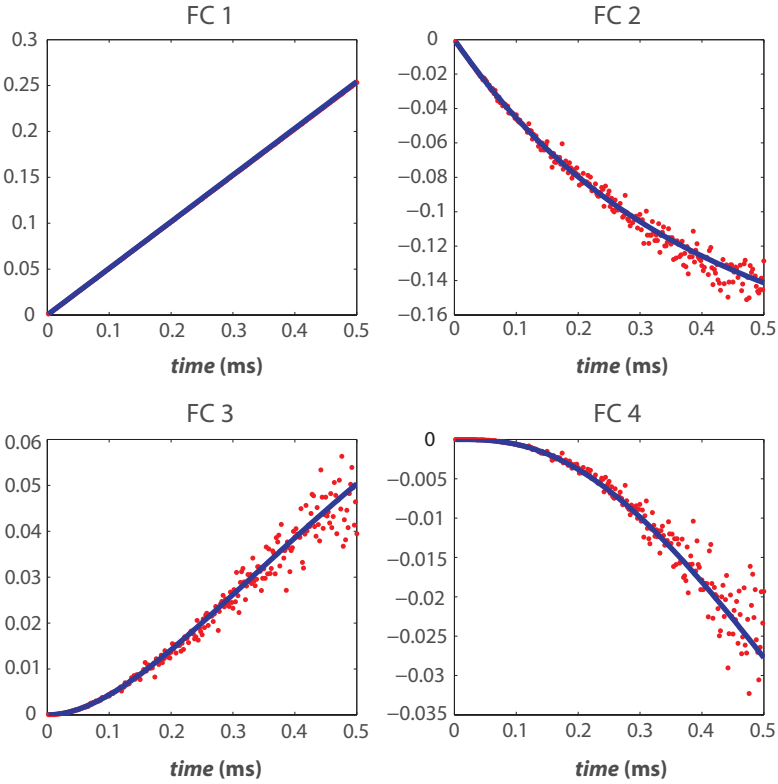

Figure 5.15: Factorial cumulants for first four orders (normalized over first) calculated for the 'blue single dagger' position of Fig. 5.14. Red data points are from the experimental data. Blue fit is from the theoretical model explained in work of Kambly et. al. [125].

We see near accurate fit, for the theoretical model for the following parameters;

$$\begin{aligned} \Gamma_{\text{Source}} &= 0.597\,\text{kHz} \\ \Gamma_{\text{Drain}} &= 3.880\,\text{kHz} \\ \Gamma_{\text{Detector}} &= 250\,\text{kHz} \end{aligned}$$

while the experimental values were,

$$\begin{aligned} \Gamma_{\text{Source}} &= 0.590\,\text{kHz} \\ \Gamma_{\text{Drain}} &= 3.807\,\text{kHz} \\ \Gamma_{\text{Detector}} &= 250\,\text{kHz} \end{aligned}$$

The Γ_{Source} and Γ_{Drain} would otherwise also be referred to as tunnel-IN and tunnel-OUT rates respectively.

We observe the factorial cumulants of even order taking negative values, and odd orders taking positive values. This follows the theoretical factor of $(-1)^{m-1}$ for $m = 1, 2, 3, 4$. The factorial cumulants do not oscillate though.

Following a simple Coulomb blockade model of our dot system, at a low-bias regime of 'single blue dagger' from the experiment, the energy level at the dot is well above the electrochemical potential of the drain and much lower than the electrochemical potential of the source, $\mu_{\text{source}} \gg \varepsilon_{\text{dot}} \gg \mu_{\text{drain}}$. The transition from (N) $\rightarrow$ (N+1) $\rightarrow$ (N) state (Fig. 5.16), carries an electron through the QD across the barriers. Since this corresponds to a simple unidirectional transport through a single energy state in the dot (a two state Markovian system), we expect no electron-electron interactions that would influence the statistics of the electron transiting through the dot. We do not have any situation for a Coulombic interaction at the dot. The factorial cumulants agreeably do not oscillate at this situation.

We further evaluate the factorial cumulants at the position of 'double blue dagger' of Fig. 5.13 which is at a comparatively high-bias situation than the situation at 'single blue dagger' position. We expect the energy window to further open up, to allow more states to become available, for the tunneling electrons to traverse across the *source* barrier through the dot. We would

briefly discuss the scenario of the electron transfer schemes across the energy levels at the dot. Once the $(N+2)$nd energy level is visible to the electron, the probability for two electrons to occupy the dot at the same time gets very high, which was also shown by Gustavsson et. al in [169]. Depending on the coupling of the QD with the *source* and the *drain* leads, at higher QD biases, electron transitions of (N) → (N+1) → (N+2) → (N+1) → (N) or (N+1) → (N+2) → (N+1) get highly likely.

The figure of 5.14B shows the time trace for this situation with the electron occupation probability of '1' and '2' at the dot. For this unique situation we would evaluate the factorial cumulants on the conditional statistics of tunneling-IN and tunneling-OUT cases as schematized in Fig. 5.17.

The tunneling events for the 3-level state data are identified as (N) → (N+1) or (N+1) → (N+2) transitions counted as single tunnel-IN event for each time bin and (N+2) → (N+1) or (N+1) → (N) transitions as single tunneling-OUT event for each time bin. The *P(n,t)* for either of these processes are different. We however never counted jumps of 2 states

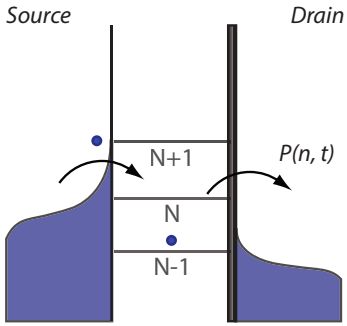

Figure 5.16: Simple Coulomb dot system. The 'Drain' barrier is slightly less transparent than the 'Source' barrier (as considered for a one-to-one comparison with the experimental situation). The schematic shows only one occupation possibility for the electron, akin to situation discussed for 'single blue dagger' of Fig. 5.13 and factorial cumulant results of Fig. 5.15.

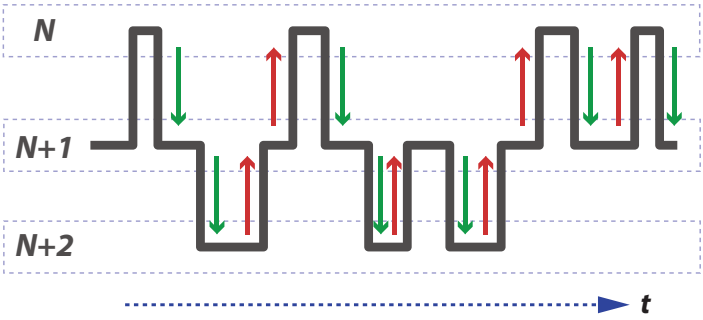

Figure 5.17: Conditional tunneling cases used to evaluate the factorial cumulants for the 3-level dot system. Each 'green' arrow is a tunneling-IN event, while each 'red' arrow is a tunneling-OUT event.

like (N) → (N+2) or (N+2) → (N) (though it was sparsely observed in few time traces) as, our experiment was bandwidth limited to few kHz, it was very likely that these double jumps as seen at the QPC were due to non-resolution of single state jumps at the QPC. Also we would further see that it was necessary to avoid extremely short time events (within the limits of experiment bandwidth) so as to conclude the waiting time distributions did not follow two different distributions.

The factorial cumulants for the conditional tunneling situation at two different positions (different from the blue dagger positions) of Fig. 5.13 is plotted in figures of 5.18 and 5.19. We discuss two cases, where for "Case A" represented by Fig. 5.18 is at a situation of dot bias of 2.175 mV and gate-G2 bias of 164.5 mV. "Case B" represented by Fig. 5.19 is at situation of dot bias of 2.175 mV and gate-G2 bias of 166 mV.

The factorial cumulants in both figures of 5.18 and 5.19 are plotted for the 4th order as this order could represent the highest possible with least amount of noise for the set of data from this experiment. The plots are plotted in log-log format, to allow for very clear observation of the oscillations where the factorial cumulant values move about the 'zero' of y-axis at very short time scales.

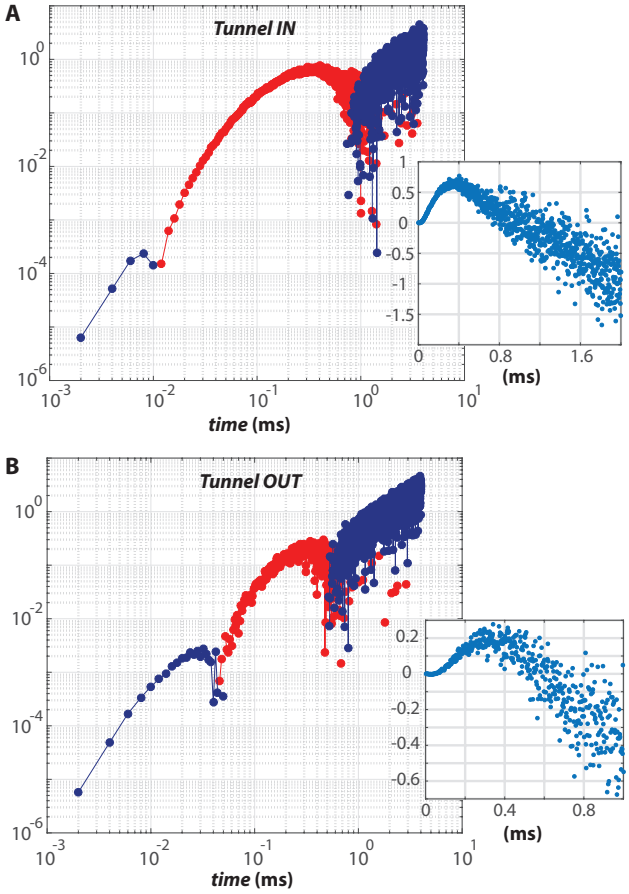

Figure 5.18: 4th order normalized factorial cumulant for the conditional tunneling situation of case A (G2-gate bias of 164.5 mV, dot bias of 2.175 mV, see text). The log-log plots very clearly identify the oscillations away from '0' at very short time scales which is otherwise not clear in the linear plot shown in the inset. 'Blue' points show negative values while 'red' points show positive values. The time scale is up to 4ms. The data is shown as numerically extracted from the calculations, to show the noise development at the longer time scale. We observe oscillation for both tunneling IN and OUT situations for the electrons, as shown in A and B respectively.

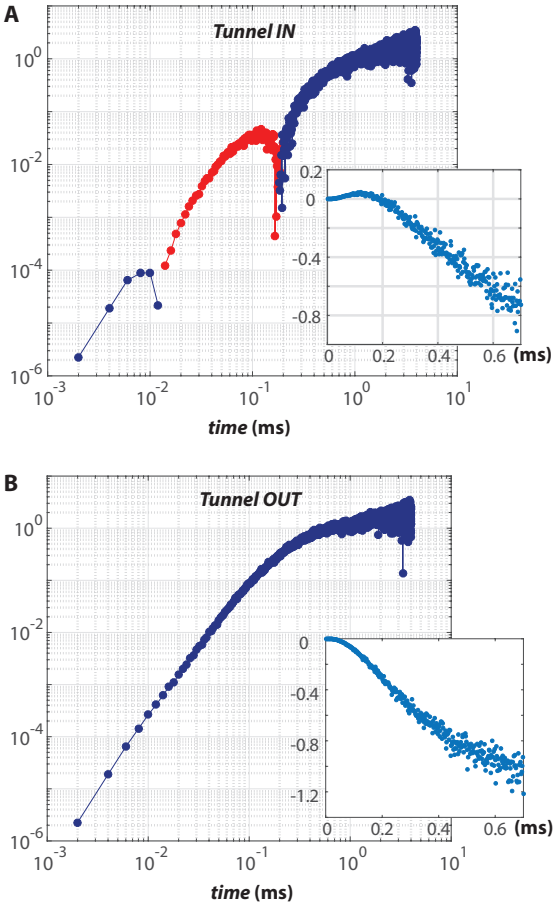

Figure 5.19: 4th order normalized factorial cumulant for the conditional tunneling situation of case B (G2-gate bias of 166 mV, dot bias of 2.175 mV, see text). The log-log plots very clearly identify the oscillations away from '0' at very short time scales which is otherwise not clear in the linear plot shown in the inset. 'Blue' points show negative values while 'red' points show positive values. The time scale is up to 4ms. The data is shown as numerically extracted from the calculations, to show the noise development at the longer time scale. We observe oscillation only for tunneling IN situation, and no oscillations for the tunneling OUT situation, as shown in A and B respectively.

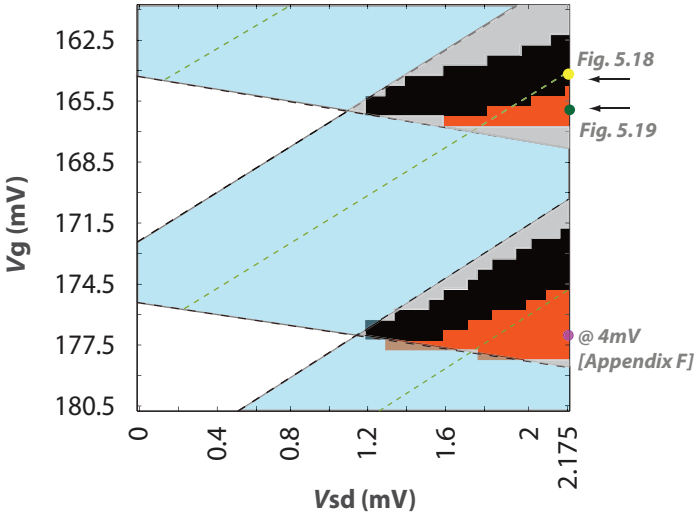

Figure 5.20: 4th order factorial cumulant shown for both tunnel-IN and tunnel-OUT cases across the whole span of dot and gate-G2 bias as shown in 5.13. Fig. 5.18 situation as Case A, and Fig. 5.19 situation as Case B is exemplified as 'yellow' and 'green' dots at the length of dot bias of 2.175 mV. The cases of A and B of figures of 5.18 and 5.19 actually extend over the either side of the 'dotted' green line which is otherwise also the 'dotted' yellow line from Fig. 5.13 with the 'black' colored region representing the case of oscillations for both tunnel-IN and tunnel-OUT cases, while the 'orange' colored region represent the case of oscillations only for only tunnel-IN case. The 'greyed' out region is the region where the 4th order factorial cumulant could not be properly resolved for oscillations due to noise effects. 'White' space is the Coulomb blockade region, 'blue' is the region with only one occupation probability and the factorial cumulants in this region do not show oscillations. A further point at 178 mV of gate bias marked in 'pale violet' dot, exemplified for a bias situation of 4 mV is discussed in Appendix F (Figs. 12.1-12.7), in the same analogy as bearing the characteristics of the whole 'orange' region.

We observe that for case A, the oscillations are visible for both the conditional tunnel-IN and tunnel-OUT cases while for the case B, the oscillations are only visible for only tunnel-IN case. This observation actually is made for the entire region of two occupation probability region of the high bias span as visible in Fig. 5.13. This is shown in Fig. 5.20.

We will try to explain this behavior also in terms of tunneling rate picture across the whole span of dot and gate-G2 biases.

We have the following situations, one where varying the capacitively coupled gate voltage, continuously tunes the energy levels in the QD relative to the Fermi-levels in the leads [1, 170] and it also shifts all the dot levels in a similar fashion as the gate voltage is effecting the electrochemical potentials to change all at the same time and, secondly the tunnel coupling which exponentially depends on $V_{source-drain}$ and V_{gate} [171], also becomes exponentially stronger with the further opening of the gate [172].

With this aforementioned idea, we start with a situation of Fig. 5.22A for slightly high dot bias and low gate-G2 bias situations (somewhere around where 'blue single dagger' of Fig. 5.13 was discussed). In this situation the tunneling happens through single occupation state through the dot and we do not expect any interactions. This was also shown in Fig. 5.16.

In a further high bias situation (1.2 mV - 2 mV dot bias) and and at certain higher gate-G2 voltages of Fig. 5.22B referred to as 'Case A' or 'Case B' (gate-G2 at 164.5 mV or 166 mV respectively) at the QD, we have a situation of two unoccupied energy levels coming into the transport energy window of the dot, the second being very likely the first excited state of the first ground state unoccupied level available in the dot. The tunneling rates for the transition '2 $\rightarrow$ 3', from Fig. 5.21 (either 'yellow' or 'magenta' points) in this case show a stepped increase than for transition '1 $\rightarrow$ 2' for the same 'yellow' or 'magenta' point, with the involvement of the excited level close to the *source* level at the dot and this increase is parallel to the diamond edge of the *source* $\rightarrow$ *dot* and *dot* $\rightarrow$ *drain* tunneling directions across the available energy level in the dot for these high bias situation.

When the gate-voltage is at 166 mV (case B situation), the *source* fermi level is comparatively strongly coupled to the dot due to gate-G2 being at the *source* and, after the first electron having tunneled into the dot, the stronger Coulomb force from the first electron effects in the tunneling probability of the second electron in waiting at the *source*. The tunneling-IN distribution

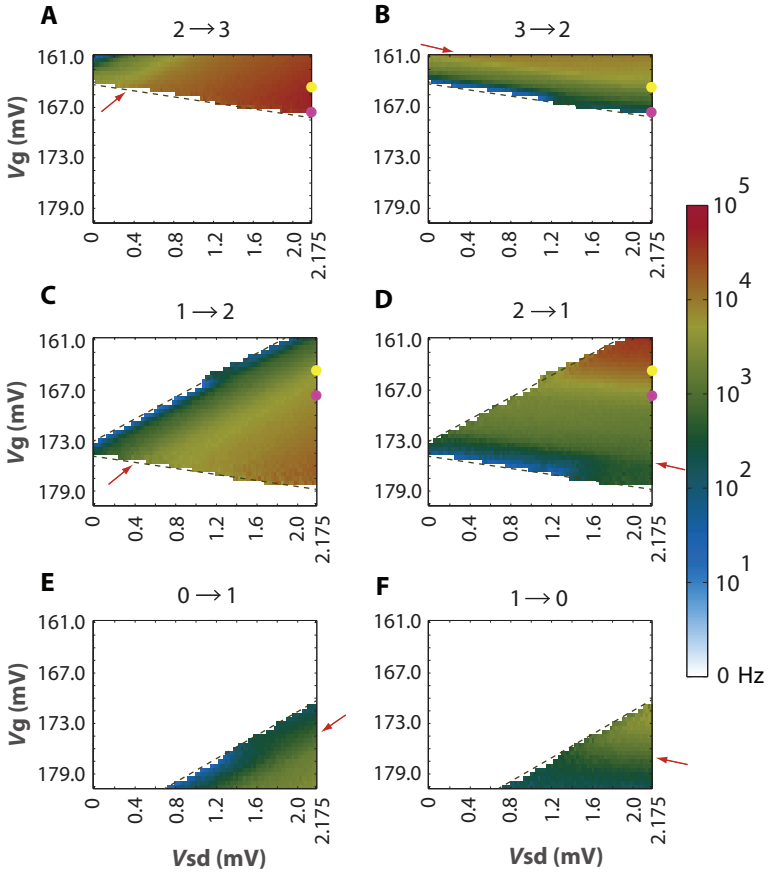

Figure 5.21: Tunneling rates for respective tunneling cases (as mentioned in the title of each sub-figure) shown for the whole span of dot and gate-G2 biases as mentioned in Fig. 5.13. The 'yellow' and 'magenta' points correspond to 'yellow' and 'green' points from 5.20. Refer text for explanation on annotations. The rate values are colored as base-10 log values of the actual rate values. 'Red' arrows show the marked step increases of the rate values, very likely at positions of the first excited state of Fig. 5.13. Please see Appendix E, on the explanation for the extraction of different rates.

is henceforth influenced from Coulomb interaction at this point. This is clearly visible as oscillations in the combined factorial statistics of the higher orders for the tunneling-IN case for Fig. 5.19A. Figure 5.22B schematize the tunneling-IN processes for this particular case.

The comparatively weakly coupled *drain* lead with the dot, does not influence the tunneling-OUT process and hence, the electrons tunnel out very much stochastically. We observe the tunneling rate for the '3 $\rightarrow$ 2' transition significantly smaller which is for the second electron for the tunnel-OUT process and so also is the case with the first electron ('2 $\rightarrow$ 1') since the *drain* fermi level is further below the energy level of the first electron in the dot (for rates at this situation, refer the magenta point of Fig. 5.21). Henceforth we do not observe any oscillation in the factorial cumulant (even at higher than the 4th order) for the tunneling-OUT process (5.19B).

Now at a gate-G2 voltage of 164.5 mV, (which further opens up gate G2; schematized in Figs. 5.22B-D), the electron distribution is further altered and ideally both the *source* and *drain* fermi levels gets 'comparatively strongly' coupled with the dot, though there is also a weaker influence on the gate barrier on the drain side from gate-G2 (source) voltage. In this situation, for the tunnel-IN process, we would follow the aforementioned argument (in the previous paragraph) as the reasons for Coulomb interactions and oscillations in the Tunneling-IN factorial cumulant. Now for the tunnel-OUT process, after the second electron has tunneled out stochastically, the first electron in the QD (implying 2 $\rightarrow$ 1 transition) sees a larger Coulomb force from the levels in the *drain* lead (also that, since the drain side is now 'comparatively strongly' coupled to the dot) "effecting" the tunneling-OUT process through Coulomb interaction from the *drain* side, which in turn, effects tunneling-OUT factorial cumulant to show marked oscillations just like in the tunneling-IN case (5.19A-B).

We can very strongly negate any 'back tunneling' since in these high energetic regimes (involving high bias and 3-level states), we do not observe either tunneling-IN or tunneling-OUT rates to be similar for any point in this regime, i.e, neither '3 $\rightarrow$ 2' and '2 $\rightarrow$ 3' or '1 $\rightarrow$ 2' and '2 $\rightarrow$ 1' rates for both 'yellow' and 'magenta' points are similar. The rates were determined through the slope (and later factored with normalized distribution values for case of 2 $\rightarrow$ 3 and 2 $\rightarrow$ 1 tunneling processes, due to certain behavior of waiting time distributions further discussed in the section of 'waiting time distribution', also see Appendix F) of the log plot of the waiting time

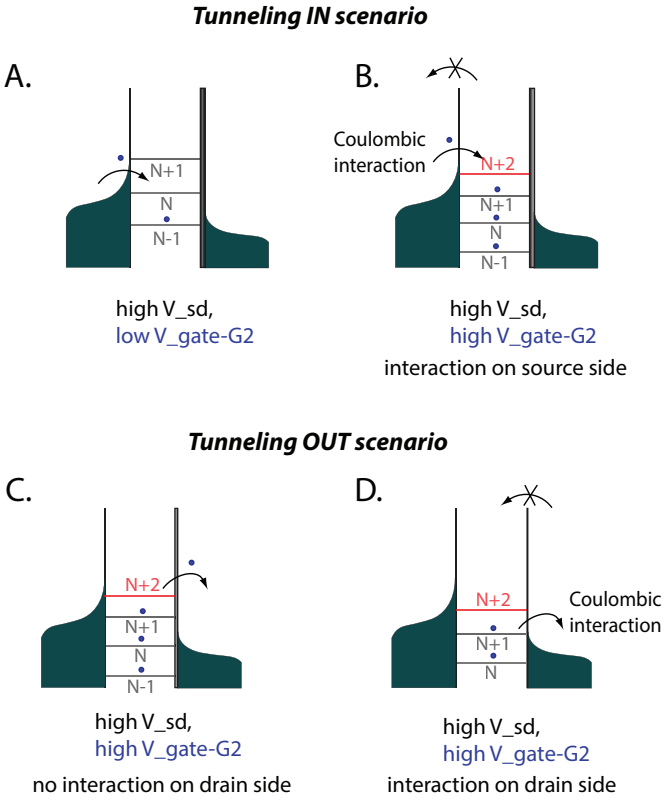

Figure 5.22: Schematic depicting tunneling schemes for situations of low and high bias situations. 'High V_{sd}' implies high dot bias, 'high (low) V_{G2}' implies high (low) gate-G2 bias situation.

distribution for each point in the dot bias and gate-G2 bias span, by a linear fit through the slope as we have the distribution given as,

$$P(n,t) \propto e^{\Gamma t} \tag{5.23}$$

with Γ being the tunneling rate. The rates shown in Fig. 5.21 are the base-10 log values of the actual rate values. Figure 5.23 shows how the distributions are skewed at very short time scales and at comparatively very

long time scales and the fitting process ideally was done at the region where the the time scale was in between as shown in Fig. 5.23.

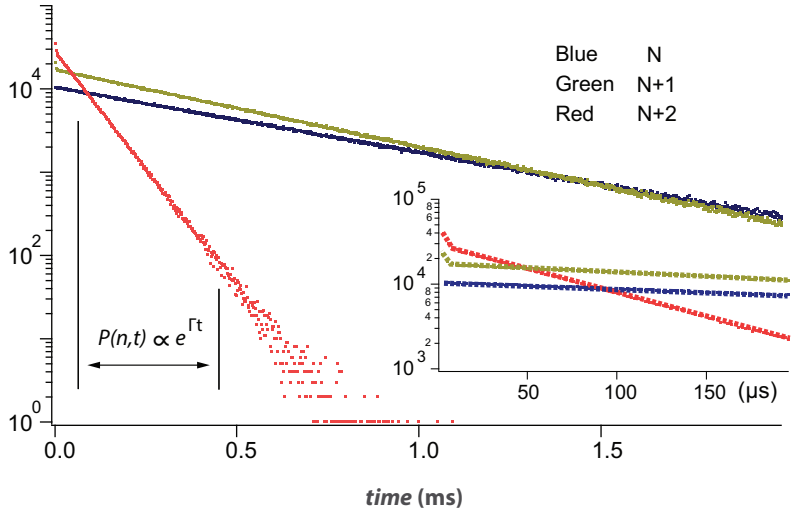

Figure 5.23: Determination of rates depended on fitting to the right region of the waiting time distribution (shown in the figure above), since at very short times, the distribution was highly skewed (also shown as magnified in the inset), since the counting of waiting times gives high density of very small time events which are thought to be present due to the experimental bandwidth limitation and possibly their length not entirely representative of actual waiting time. At very long times, the distribution also gets scattered (which can vary to high degree in short data set) due to sparse long time events. Hence the fitting algorithm to determine the rate (for the set of about 4000 data distributions of Fig. 5.21), was made to consider regions predominantly shown by the black line limits in the figure.

The idea of the above discussed argument in favor of the observations of figures 5.18 and 5.19 is complemented by the continuation of similar observation over the range of two occupation probability regions at high bias situations of the dot as is seen in the figure of 5.20.

We shall just try to look at the 2nd normalized normal cumulant (the Fano factor) for the cases of 'Case A' and 'Case B' from figures of 5.18 and 5.19 in Fig. 5.24, and, we do observe the fano factor getting over the

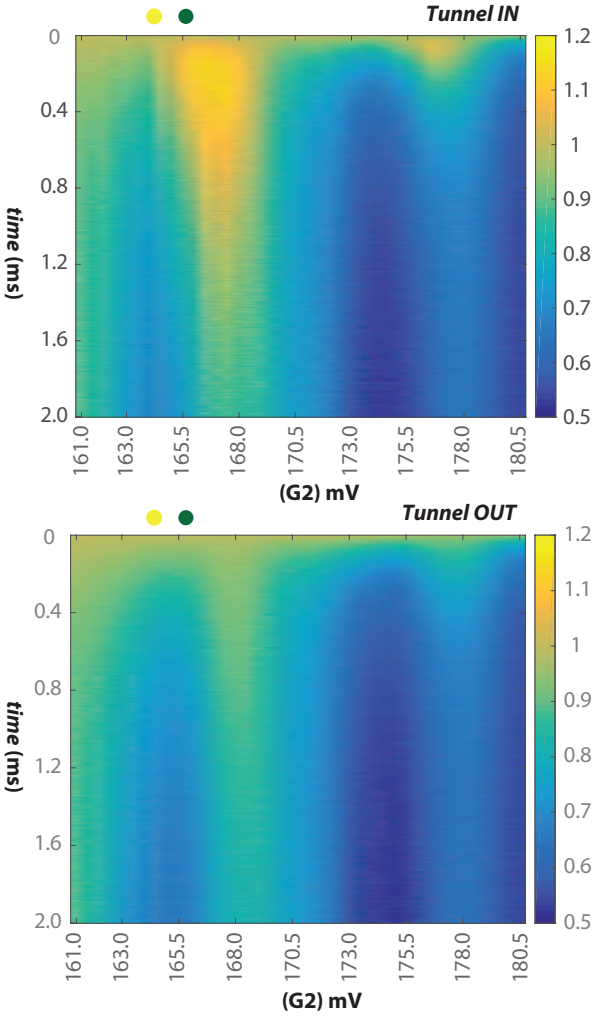

Figure 5.24: 2nd normal cumulant normalized over 1st, or the Fano factor observed over time for the dot bias of 2.175 mV and the range of gate-G2 voltages discussed in figure 5.13 and the case of figures 5.18 and 5.19 are particularly presented here.

value of 1, which ideally signifies super-poissonian distribution and very likely a hint of interaction. Dramatically the tunnel-IN case shows values larger than 1, for both gate-G2 bias values as referred in figures of 5.18 and 5.19, but not for the tunnel-OUT case. We just try to validate our arguments for the interactions through the normal 2nd cumulant though it is not very indicative as the factorial cumulants of figures 5.18 and 5.19. We also observe that the 2nd cumulant normalized over the 1st, takes larger than 1 values at short times scales, close to 0.2 ms, which ideally is also not affected due to noise factor in the evaluation of the statistics which otherwise is very visible at long times. Another situation just as discussed in Case B (of Fig. 5.19) above but, for a very high dot bias of 4 mV is discussed Appendix F (Figs. 12.1-12.7) of this thesis wherein we show a similar behavior of oscillating factorial cumulants for tunnel-IN case and non-oscillating factorial cumulants for tunnel-OUT case.

Further as discussed by Philipp Stegmann and Jürgen König in [[173]] for the generalized factorial cumulants, we also show in our experimental results that, the factorial cumulants even during the presence of interactions, observe the power law over time t as, t^m, m being the order of the factorial cumulant. This is shown in figures of 5.25 and 5.26. We observe that as the order increases, the magnitude of the factorial cumulants also increase from 1 to 4, only at the shorter time limit. For the first factorial cumulant, the slope of Fig. 5.25A shows the magnitude increase from 5×10^{-2} to 5×10^{-1} for a respective change in time from 10^{-2} to 10^{-1} and hence we have a 1st order power law with time. In Fig. 5.25B we have, for the 2nd factorial cumulant the magnitude increase from $\approx 2.3 \times 10^{-5}$ to $\approx 2.3 \times 10^{-3}$ for a respective change in time from 10^{-3} to 10^{-2} and we have a 2nd order power law with time. From Fig. 5.26A, for the third factorial cumulant, we have the magnitude change from $\approx 2.5 \times 10^{-7}$ to $\approx 2.5 \times 10^{-4}$ for a respective change in time from 10^{-3} to 10^{-2} and we have a 3rd order power law with time. From Fig. 5.26B, for the fourth factorial cumulant, we have the magnitude change from 4.0×10^{-9} to 4.0×10^{-5} for a respective change in time from 10^{-3} to 10^{-2} and we have a 4th order power law with time. Appendix F (Figs. 12.1-12.7) further discusses the factorial cumulants in the log-log scale for further higher orders (for a different experiment) and while they are plotted there in the normalized (over the first factorial cumulant) form, they very much show similar behavior at the shorter time scale, as orders increase.

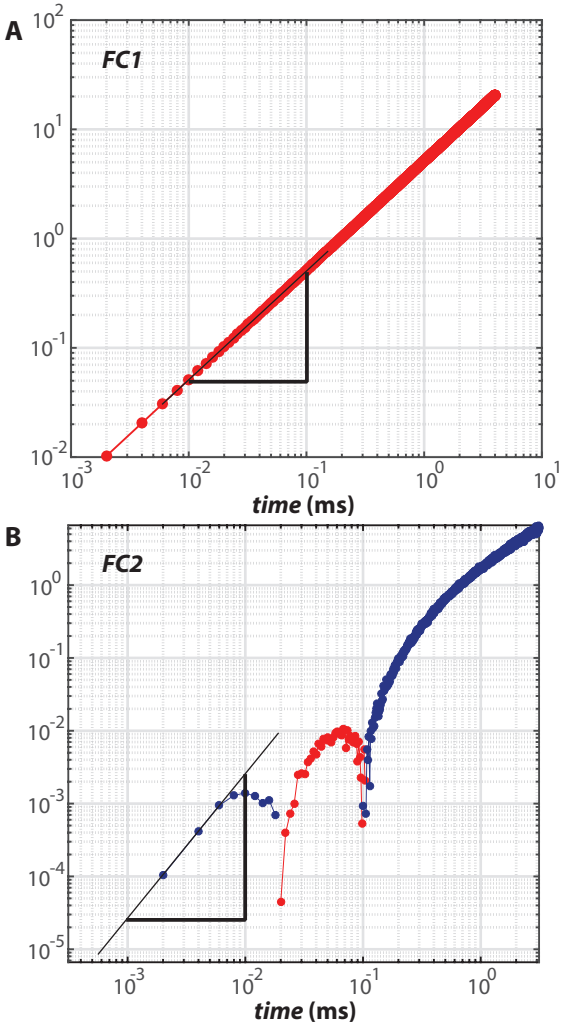

Figure 5.25: Power law fit t^m of time t, for order $m = 1, 2$ [[173]]. The factorial cumulants are from the case A situation of Fig. 5.18 and are not normalized. We see the magnitude scales up proportional to the order as function of time with order 1 in A, and order 2 in B (see text for slope values).

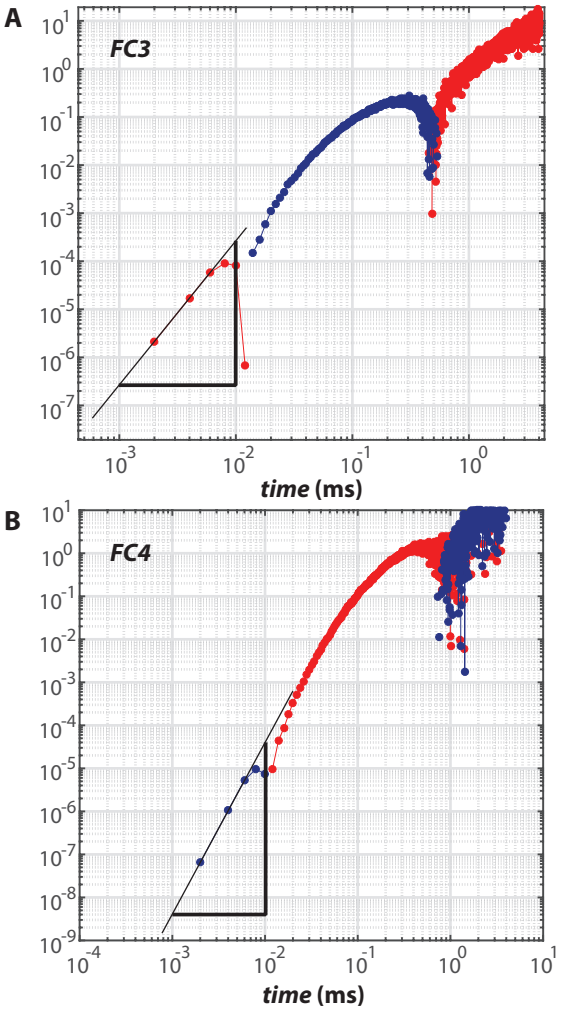

Figure 5.26: Power law fit t^m of time t, for order $m = 3, 4$ [[173]]. The factorial cumulants are from the case A situation of Fig. 5.18 and are not normalized. We see the magnitude scales up proportional to the order as function of time with order 3 in A, and order 4 in B (see text for slope values).

5.3.3 Waiting time distribution

Complementary to the discussions of cumulants from previous two sections, the waiting time distributions (WTD) [124, 174–178] also provides us with a significant statistical insight into the tunneling events and as well allows detailed investigations into very short times scales. The waiting time distribution is the delay time between two switches or events for the electron tunneling in / out of the dot and is widely studied in the realm of quantum optics. Waiting times carry (a) a certain causal information (we will see further in our discussions that, this causal information is from the electron's state across the barrier), (b) the single or more than single reset characteristics of the dot (in our experimental consideration) and (c) possibly the Coulomb interaction information (in relation to point (a)). We start our discussion with a very unique observation on similarity of two tunneling rates, for 3-level state system (more than single reset system) of our quantum dot and cross relate this observation with the stochastic behavior of widely used functional mathematical function used in computing systems.

We shall foremost discuss our simple Coulomb blockade dot and the 3-level state system that it offered us at high bias situation to discuss how the waiting times evolve through the tunneling process across the barriers.

We observe from Fig. 5.27 that the distributions for the transition from $2 \rightarrow 3$ and $2 \rightarrow 1$ state always have the same slope, while we still think that, the tunneling process from the state 2 in either direction of the barriers, which can bring an additional electron or, empty the existing electron at the dot, though expectedly stochastic in character, their waiting times are distributed alike (not same distribution though) and their tunneling rates are nearly the same.

We could simulate the model of the simple Coulomb blockade dot with two tunneling barriers (Fig. 5.30) but with no detector in the simulation, using the following algorithmic description.

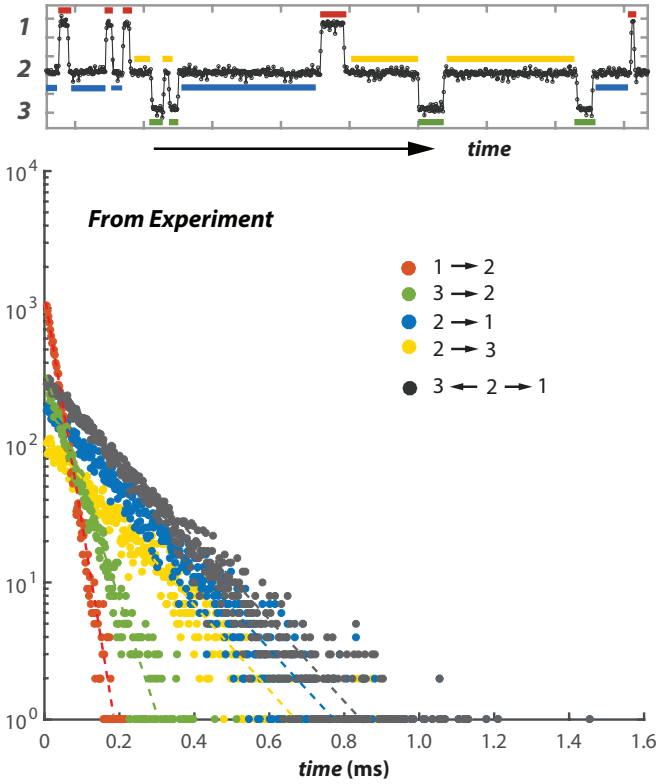

Figure 5.27: Waiting time distribution for a time trace as highlighted in the top, the color of the distributed data corresponds to the state of electron waiting to transit to either state, looking in the forward direction of time and unidirectional transport mechanism. The data set show time distribution which is scattered to a higher degree at longer time scales. The y-axis show the actual distribution of the waiting times. The solid colored lines are guide to the eyes which were also fit through regression based fitting method, to show the nature of the slope for the different waiting times. We see that, distributions shown for yellow and blue data points, have a similar slope. Black data point is the sum of the distribution for tunneling events happening on either directions from state 2 (sum of yellow and blue). Please see Appendix E, to find how we got ahead with rate differentiation for the two tunneling rates from tunneling events from either directions of state 2.

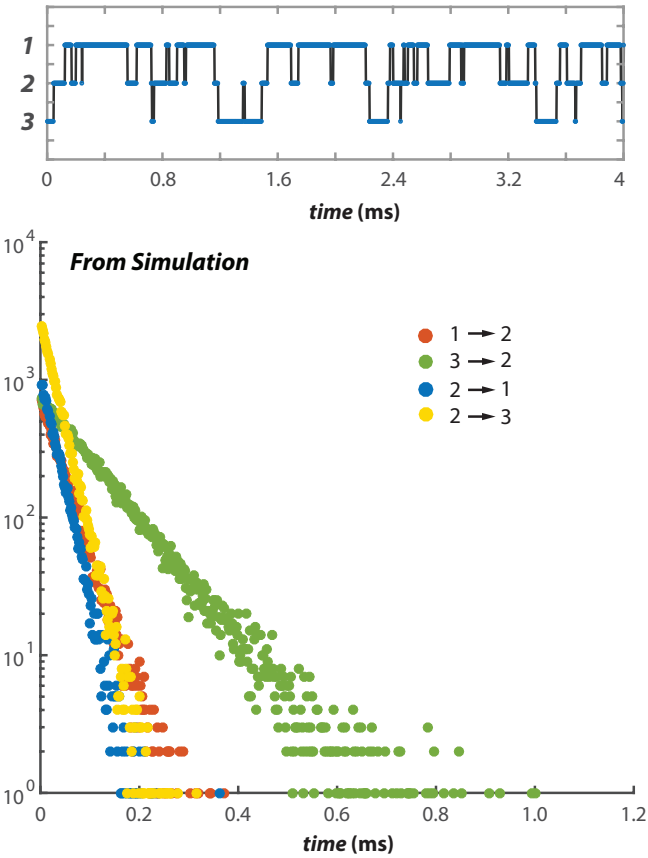

Figure 5.28: Waiting time distribution for a time trace as highlighted in the top, simulated using the random number generator of Matlab (Mersenne Twister) and Windows OS. Along with discussions in the text, flow chart of Fig. 5.29 explains the algorithm behind this simulation. We again observe the distributions given by blue and yellow data points having similar slope, the characteristics is very similar to that described in Fig. 5.27

The algorithm also explains the Fig. 5.29 in the following steps;

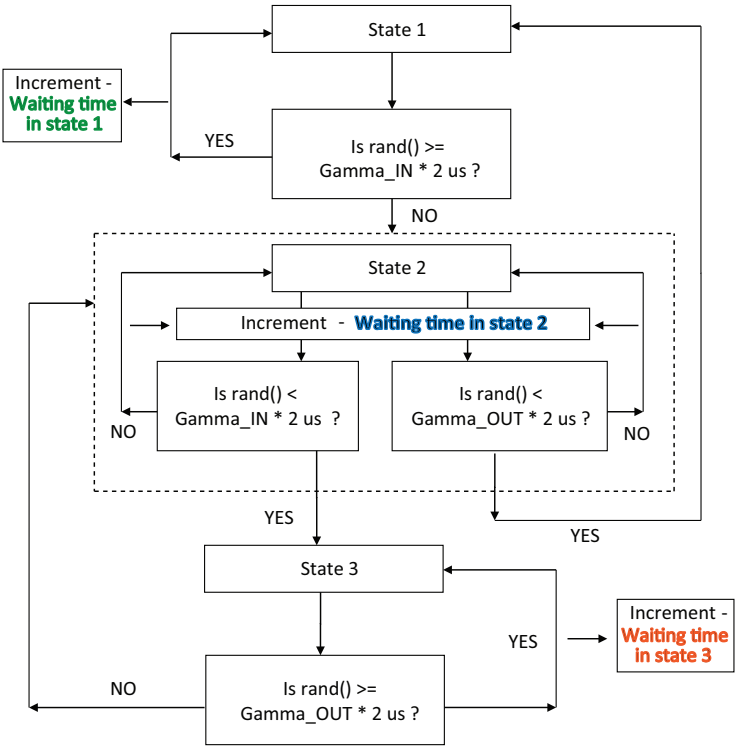

Figure 5.29: State flow picture for simulation of the waiting time distribution and time trace shown in Fig. 5.28.

1. Since, there are only two tunneling barriers, we will technically have only two tunneling rates which of course will depend on the waiting time of 'blocking' electron in the dot, for the tunneling-IN electron and, the tunneling-OUT rate would depend on the waiting time of the 'blocked' electron in the dot, due to electrons across the 'Drain' barrier.

Now this idea though is straightforward, the presence of an another occupation state within the dot, would create a third tunneling rate for this electron, and for clarity, this third tunneling rate would in principle be due to the waiting time of that electron being again blocked due to electrons across the 'Drain' barrier

2. The inputs are;

   2 tunneling rates (Rate 1 and Rate 2 respectively as Tunnel-IN rate and Tunnel-OUT rate) due to two barriers irrespective of the number of occupation states available in the QD; and we have from these rates, two respective scalar values, 'Scalar 1 = Rate 1 x shortest time resolution of the experiment' and 'Scalar 2 = Rate 2 x shortest time resolution of the experiment'

   the total number of the tunneling events (Total length)

3. The simulation starts with the electron in an arbitrary state, say state 1:

4. Within state 1: a random number is generated and evaluated against Scalar 1: i.e., Is random-number() $\geq$ Scalar 1: True? As long as random-number() $\geq$ Scalar 1:, count variable Count-for-state-1 is incremented from zero value and this count is the waiting time the electron will spend in State 1: If random-number() $\geq$ Scalar 1: is False ? then, Waiting-time-for-State1 = Count-for-state-1, Goto step 5

5. The electron is in State 2:

6. Within State 2: again, two conditions are evaluated in parallel since after State2 an electron could be next visible in either State1 or State3, and the two conditions are evaluated until Count-for-State-2 $>$ 0 and no jumps are made from State 2; another count value Count-for-State-2 is incremented from zero Condition 1: Is random-number() $<$ Scalar 1: ? If True ?, Waiting-time-for-State2 = Count-for-State-2; Break the step 6 loop and Jump to Step 7 (into state 3) Else if Condition 2: Is random-number() $<$ Scalar 2: ? If True ?, Waiting-time-for-State2 = Count-for-State-2; Break the step 6 loop and Jump to Step 3 (into state 1)

7. The electron is in State 3:

8. Within State 3:, random number is generated and evaluated against Scalar 2, i.e., Is random-number() $\geq$ Scalar 2: ? Until this condition is true, Count-for-state-3 value is incremented from zero value If random-number() $\geq$ Scalar 2: is false, Waiting-time-for-State3 = Count-for-state-3; Goto Step 9

9. If '(total number of Waiting-time-for-State1 + total number of Waiting-time-for-State2 + total number of Waiting-time-for-State3) $<$ Total length (of events)' is True, Goto Step 3, else Goto Step 10

10. Stop

and the tunnel-IN and tunnel-OUT values for the simulated result was 25kHz and 10kHz respectively, while the minimum data point size was 2μs as it was in our actual experiment. The total numer of events was about 100000, inclusive for all the three states.

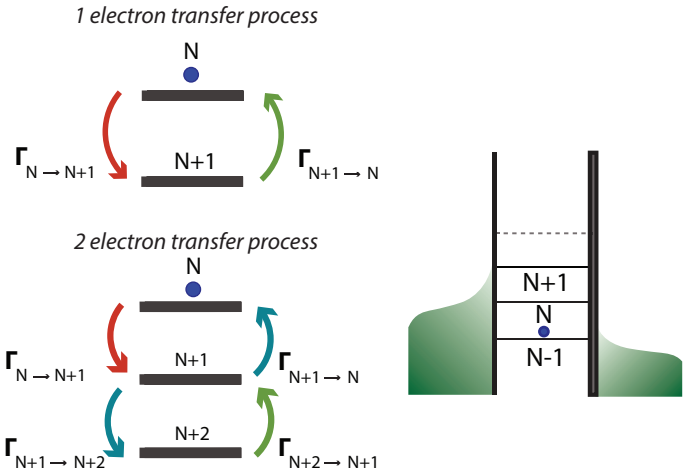

Figure 5.30: Tunneling probabilities shown for 1- and 2-electron tunnel process through a simple, two barrier Coulomb blockade dot model.

Figure 5.30 schematizes the tunneling process through single or double occupation states across the two barrier Coulomb blockade dot model. Tunnel-IN direction is observed as (N) → (N+1) or (N) → (N+1) → (N+2) change of charge states while respectively (N+1) → (N) or (N+2) → (N+1) → (N) change of charge states are observed as tunnel-OUT directions. For the case of three level states this conditional treatment of tunneling time distribution for the tunneling direction just follows what we do for the case of two level states. The tunneling rate $\Gamma_{N->N+1}$ or $\Gamma_{N+1->N+2}$ or $\Gamma_{N+1->N}$ or $\Gamma_{N+2->N+1}$ could be either extracted from the corresponding slope of the line fit as shown in the figure or by considering, $\Gamma = 1/\langle\tau\rangle$ where, $\langle\tau\rangle$ is the corresponding averaged tunneling time extracted from the respective distribution or the slope of the linear fit of the respective distribution.

The observation in the case of 2-electron transfer process, the slope being the tunneling rate, the rates are similar when the electron is tunneling from one particular level which is the (N+1) state (i.e, the slopes for the distributions of 2 → 1 and 2 → 3 is very similar). This behavior is observed for any 3-level state transport process. For a process which is very stochastic this observation is very unique. The two tunneling process from the (N+1) level is supposedly an independent one from each other owing to the Coulomb blockade influence from two different sides (barriers) of the quantum dot but still the averaged tunneling times are observed to be very similar.

The simulation study through the model (as described above) yields results seen in figure of 5.28 very similar to that of Fig. 5.27. This idea of stochastic transfer involving only two barriers keeps the state of transfer from $N + 1$ state very much same. There is perhaps a memory effect ideally due to less of a random process and while it is also known of the random-number-generator algorithms used in Matlab and Windows OS, being not purely random in nature (called as pseudo-random). In analogous case of our actual experimental quantum dot with two barriers, this ideally in terms of Coulomb blockade, allow the (N+1)st electron in the dot see the barriers (implying 2 → 1 transition, with dot being emptied) in the same way, as the (N+2)nd electron waiting at the barrier contacts see the dot (implying 2 → 3 transition, with dot being filled with 2nd electron).

We think that the Coulomb interaction limits the stochastic nature of the transfer process particularly when the dot provides the energy window for the electron to accept second electron immediately or transfer the first electron

immediately and, this very likely is influenced by the barrier transparency at that moment, into the electron rate in a same way, which makes the rates very similar for both tunneling processes. The barrier transparency for these two tunneling processes while being similarly influencing the electrons to interact at the dot, the transparency is always unique for a given gate-G2 and dot bias values.

Having discussed the waiting time distribution idea from an experimental point of view, when we observe the rates for tunneling process of $2 \rightarrow 1$ and $2 \rightarrow 3$ to be similar, we differentiate the rates for these two processes by factoring the slope-obtained values with the ratio of the mean of the distributions of either process ('yellow' or 'blue' data sets of Fig. 5.27) with the mean of the distribution of the sum of both the processes ('black' data set of Fig. 5.27). This way the tunneling rates (for the two processes) are understood to be influenced by the pseudo-stochastic process at the barrier which ideally makes one distribution different from other ('yellow' and 'blue' data set of Fig. 5.27).

We further plot the waiting time distribution in linear scale for cases of both 2-level state system and 3-level state system in figures of 5.31 and, 5.32 in reference to two gate-G2 biases as referred to in the figure caption.

For the data of Fig. 5.31 ideally follows the simple example of single-reset system of [124], where the dot is able to reset to its initial ground configuration (within the regime of Coulomb blockade) with tunneling of single electron, with the waiting time distribution $W(\tau)$ for time τ given as,

$$W(\tau) = \frac{\Gamma_L \cdot \Gamma_R}{\Gamma_L - \Gamma_R} e^{-\Gamma_L \tau} - e^{-\Gamma_L \tau} \tag{5.24}$$

with Γ_L and Γ_R forming the rates at input and output barrier at the dot. We do observe $W(\tau) \rightarrow 0$ as, $\tau \rightarrow 0$ for this simple case (the fit in Fig. 5.31 also accounts for a small factor in the denominator, along with the result of the aforementioned equation). The fit values were, $\Gamma_L = 2.55$ kHz and $\Gamma_R = 7.2901$ kHz, which from actual experiment data were 2.2333 kHz and 7.2901 kHz respectively.

The vanishing of the waiting time ideally indicates that once the electron has tunneled out of the dot, the dot recedes into the empty state configuration and can be filled immediately by another succeeding electron.

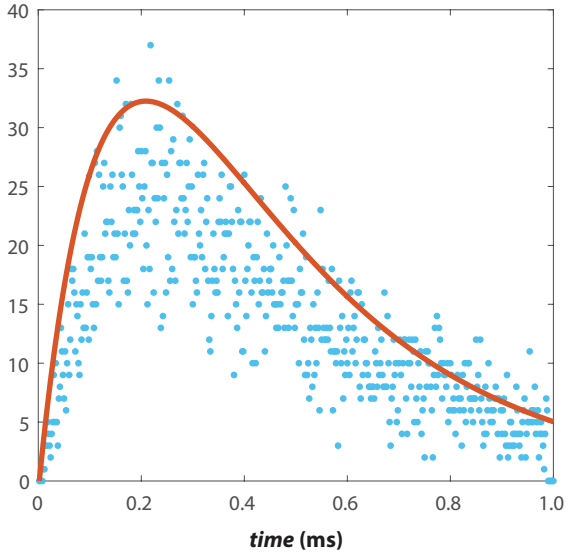

Figure 5.31: Waiting time distribution for a 2-level state system (just one occupation state at the dot) for the case of dot bias of 2.175 mV and gate-G2 bias of 169 mV (see Fig. 5.13). The fits are from Eq. 5.24.

From the discussions of Tobias Brandes in [124], we expect the 3-level system to be a sort of a multiple-reset system though our system is not spin-degenerate compared to the theoretical discussion therein. The waiting time distribution for a 3-level state system is plotted in Fig. 5.32. The tunnel-IN and tunnel-OUT times were determined with the immediate preceding waiting time to the tunneling-IN process (see Fig. 5.17) and the immediate succeeding waiting time to the tunneling-OUT process respectively. The waiting time distribution here, approaches '0' as $\tau \to 0$ with a certain jump for both the cases of tunnel-IN and tunnel-OUT situations. This is again a new observation which unlike the case for 2-level state system. The jumps are not from the counts of more than 1-electron at a time, but the statistical distribution of the tunneling times observed in our experiment. The fit in the figures of 5.32 is through Gaussian and not through the multiple reset model of [124]. The step from 0 to a finite value in the distribution is not due to omission of short time events during the counting process. So it is

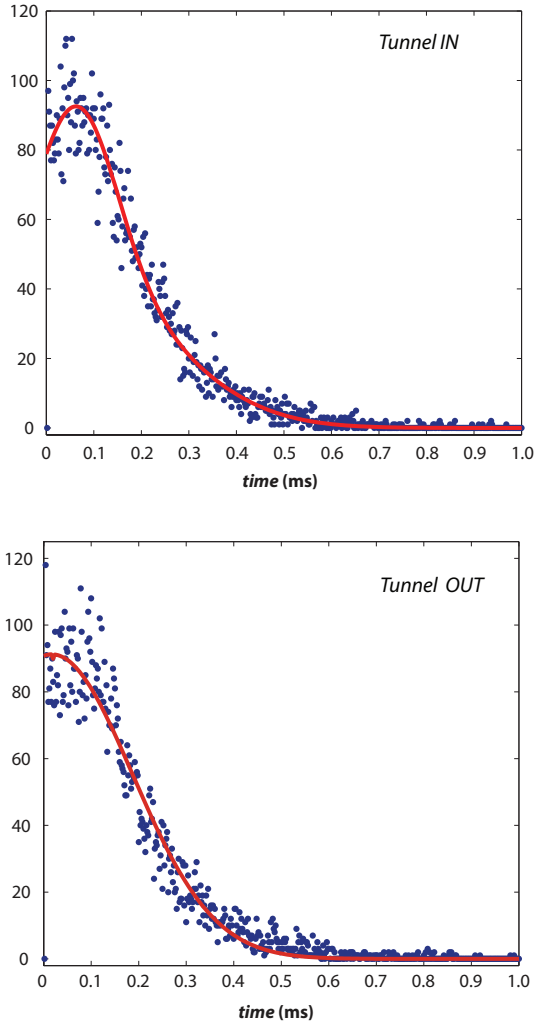

Figure 5.32: Waiting time distribution for a 3-level state system (two occupation state at the dot) for the case of dot bias of 2.175 mV and gate-G2 bias of 163.5 mV (see Fig. 5.13). The fits are Gaussian.

interesting to observe how the waiting times evolve with a definite value at short time limits and follow a Gaussian as time increases.

While it is possible that the limitation of our detector could be a reason to have this observation, but it is very unlike from the distribution of a 2-level state system where the distribution evolves gradually from the short time limit and progress into a Gaussian like behavior as time increases. It would definitely be important and interesting to see the same experiment done with a very high bandwidth detector.

5.3.4 Concluding Remarks

We have observed that counting statistics in terms of normal cumulants are not strongly indicative of absolute changes in temperature or barrier asymmetry, except that, due to changes in temperature and barrier asymmetry, the distribution of tunneling events does change and that is seen as changes in the time evolution of higher order cumulants. The magnetic field also has a similar effect on the subjection of tunneling through strong spin blockade which is observed in the cumulants' time evolution behavior, but as such information on spin blockade cannot be extracted from the evolving statistics. The influence of parameters of temperature, barrier asymmetry and magnetic fields are inferable in only relative terms with changes in each parameter.

On the other hand, we evaluate factorial cumulants and we can absolutely infer the presence or absence of Coulomb interactions with looking at the presence or absence of oscillations in the magnitudes of higher order factorial cumulants. While it is important to note that, the oscillatory behavior of factorial cumulants have been observable only in the 3-level state system and not on the 2-level state system, we infer that, the 3-level state system is a better choice to study better any interacting system as the presence of 2 electrons in the tunneling process at the dot, increases influence of electronic interaction to become visible in the tunneling statistics.

Secondly we also observe from 3-level system experiment that, there is a certain causal relationship on the electron tunneling processes into and through the dot. The 2nd electron in waiting to tunnel in (to fill N+2 state), gets influenced by electron already at the dot and further, the 2nd electron in waiting to tunnel out (emptying N+1 state), also gets influenced by electron at the dot. Due to this we do observe a similar tunneling rate for both the tunneling processes, which is possibly a good indicator of a causal (and less of a purely stochastic) relationship in the tunneling process.

We should note that, this observation is made at all positions of dot and gate-G2 bias for 3-level state system.

While if can ask why this behavior is not indicated in a 2-level state system, the answer could be that, in this system, the statistics from the only electron to tunnel in and tunnel out is not fully representative of any Coulombic interaction that might have happened at the dot, which is otherwise strongly visible in a 3-level state system.

We have hence presented counting statistics as a useful tool to apply into the studies of physical system in mesoscopic systems.

6 Conclusion

The primary result in this thesis work discusses the idea of using full counting statistics of single charge transport to clearly identify an interacting and a non-interacting electron system. Further, towards the quest of creating a reliable multiple quantum-dot and charge detection system, hybrid nano-structures were investigated and attempted to be fabricated in our lab.

Hybrid nano-structures were fabricated with the intention to increase detection sensitivity of charging/discharging happening at the quantum dots and hence improve the signal to noise ratio at the quantum point contact (QPC). Hybrid nano-structures were fabricated on shallow 2DEG heterostructures employing top gates, forming the dot structures and QPC gates while AFM structured barrier isolated dot structures from the QPC gates. In preliminary studies using this design, the sensitivity of the QPC was found to be much better than those employed through purely top gated structures (and hence holds good promise to form a very good charge detector, with more dots in the scheme of detection). High noise content in the measurements rendered the fabricated devices not usable for counting measurements. The high noise in the devices were primarily reasoned to the design of shallow 2DEG heterostructures which are naturally more susceptible to noises arising from impurities and dopant ions compared to deeper 2DEG heterostructures. This warrants a need for rigorous system of production and evaluation of shallow 2DEG heterostructure and devices made with them. The hybrid nano-fabrication involved rigorous steps using Optical, AFM and SEM lithography techniques and the thesis also discusses the bottlenecks and many optimization procedures undertaken at all the three lithography steps to create an electrically correct hybrid nano-structure.

Use of Palladium based ohmic contacting process was successfully implemented which allowed very small ohmic resistances (measured in combination with the mesa resistance across opposite end contacts). Palladium based contacts were found to be consistently reliably forming (offering very low contact resistances), after the annealing steps for all the 16 arms of the

star structure patterned through the Optical lithography process (using the current setup). While for the Ge/Au/Ni eutectic alloy based contacts, the contact reliability were not consistently observable. The need to have many good quality ohmic contacts was necessitated by the requirement of using ≥ 2 quantum dot structures along with the QPCs or another quantum dot for charge detection across the AFM barrier structure, in the same mesa structure. The Palladium based contacts were studied only on the shallow 2DEG heterostructures.

Moving further into the discussions of using full counting statistics to understand charge transport phenomena in the quantum dot, we have observed that unlike the higher order normal cumulants which would oscillate as a function of any system parameter (also time), the factorial cumulants have been found to behave very differently. Factorial cumulants by definition (of their generation function) were found to be alternating signs with respect to their orders while they did not oscillate. The absence of oscillations clearly represented situation of absence of interactions in our simple 2-occupation state dot system. The factorial cumulants were further observed to oscillate when the situations of Coulombic interactions became favorable in our 2-occupation state dot system. This is the first main result of this thesis. The observation of non-oscillating factorial cumulants very much coincided with the theoretical observation of non-oscillating factorial cumulants, for similar system parameters.

Our 2-occupation state dot system was made available through a bias of > 1mV across the quantum dot. We also showed that, the QPC could successfully detect the presence and absence of the second electron at the dot very clearly, which further allowed us to extract conditional waiting-time statistics for both tunneling-in and tunneling-out processes, involving both electrons at the dot.

As our second important result, we observed that, the tunneling in rate for the tunneling process happening from the state of second occupation state to the third occupation state and, the tunneling out rate for the tunneling process happening from the second occupied state to the first occupied state, is similar. There seems to exist a causal relationship for the waiting electron trying to occupy the third state (in the 3 level system) with the electron already occupied in the second state. And, similarly, there seems to exist a causal relationship for the waiting electron to empty the second state with electron occupying the first state in the dot. This causal relationship

though not been observed in any other way in our experiments, the presence of similar tunneling rates for two different supposedly stochastic process is surprising. This observation is consistently observed in each 3-level system across the dot and gate-G2 biases.

We suspect that the conditional tunneling process (condition being the intermediate electron waiting time) carries the memory of the system across the tunneling barrier (given a non-changing barrier height and temperature for both tunneling directions). This observation was also observed in our simulation experiment, using a pseudo-random number generated waiting times. The simulated result was found to be identical to the observations made from experimental data.

Our work allowed us to look deeper into the classical tunneling phenomena, while offering better understanding of Coulomb interactions and therefore enabling the application of full counting statistic technique to study a quantum mechanical phenomena. Our observations would be very interesting to be undertaken at finite frequencies involving both single and a multiple dot system, which would perhaps bring out more details on an interacting system through the application of full counting statistics.

7 Appendix A

This discussion as an extension for Chapter 3, describes the Ohmic and SEM lithography process steps. The recipes described here for Ohmic and SEM lithography process were carefully modified upon the standard recipes (from literature) for,

1. improving on number of steps undertaken until the final hybrid-structure, which would eventually reduce susceptibilities to process errors
2. improving on the contrast profile for mask layers and hence the metal layers
3. accurate placing of AFM and SEM structures
4. efficient bonding of the sample with the chip carrier
5. avoiding any possible damage to the surface and the electron gas layer in the samples, since the 2DEG was shallow one for the purpose

Additionally, the newer Palladium metal based recipes (also see Chap. 3) used for Ohmic contact laying is discussed.

Ohmic contacting process

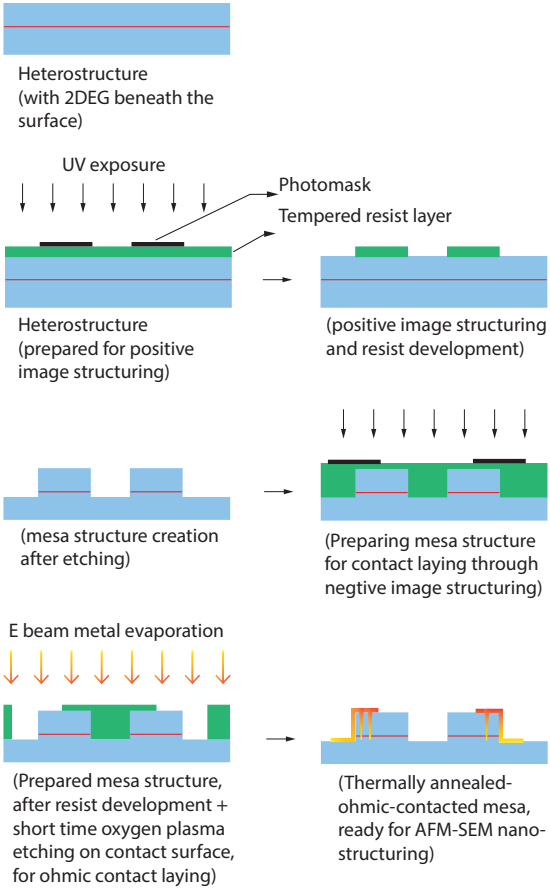

Figure 7.1: Schema of optical lithography wet-chemical processing steps, for 'GaAs/AlGaAs 2DEG' sample surface.

	For positive image structuring
1	Spin coat Photoresist† @ 6000 RPM for 60s (yields a thickness of 14000 Å)
2	Resist baked at 92°C for 3min
3	UV exposed for 10s
4	Developed‡ for 50s
5	Exposed surface etched with solution of H_2O : H_2O_2 : H_3PO_4 (40 : 2.5 : 1.5)

	For negative image structuring
1	Spin coat Photoresist† @ 6000 RPM for 60s (yields a thickness of 14000 Å)
2	Resist baked at 92°C for 3min
3	UV exposed for 10s
4	Resist again baked at 115°C for 5min for image reversal
5	UV exposed for 20s
6	Developed‡ for 50s
7	Exposed surface O_2 plasma etched for 30s (ready for metal evaporation)

Deionized water cleaning and Nitrogen drying happens before and after each step where necessary

† ARU-4040 resist - '2 -Methoxy-1-methylethylacetate' compound, with high photosensitivity, positive and negative image structuring, high contrast in negative mode

‡ AR 300-35 developer - 'Dinatriummetasilicate -pentahydrate, Trinatriumphosphate' compound, optimally suited for ARU-4040 Photoresist development

Figure 7.2: Schema of optical lithography wet-chemical processing steps, continued from Fig. 7.1, for 'GaAs/AlGaAs 2DEG' sample surface. Using very dilute HCl after step 7 of 'negative image structuring' helps remove any oxide build up and efficient ohmic contact sticking.

Ge/Au/Ni and Pd/Ge/Au alloy based ohmic-contact recipe

Standard ohmic contacting layers		Annealing recipe			
Metal layers	Thickness (nm)				
Ge	40		Final temp. (°C)	Duration (s)	At (H_2 : N_2 - 20 : 80) flow pressure of 290 mbar
Au	60	1	40	60	[ramp up from room temperature]
Ni	27	2	470	30	[ramp up from 40 C]
Au	150	3	470	120	[steady]
Au [*]	500 ~ 2500	4	40	60	[ramp down]
Pd based ohmic processing		Annealing recipe I for Pd based layers			
Metal layers	Thickness (nm)		Final temp. (°C)	Duration (s)	At (H_2 : N_2 - 20 : 80) flow pressure of 270 mbar for step 1, 2, 4; 150 mbar for step 3
Pd	10	1	40	60	[ramp up from room temperature]
Ge	40	2	180	60	[ramp up from 40 C]
Au	50	3	180	3600	[steady]
Pd	25	4	40	60	[ramp down]
Au	125				
Au [*]	500 ~ 1000	Annealing recipe II for Pd based layers			
			Final temp. (°C)	Duration (s)	At (H_2 : N_2 - 20 : 80) flow pressure of 290 mbar for all steps
		1	40	60	[ramp up from room temperature]
		2	400	30	[ramp up from 40 C]
		3	400	30	[steady]
		4	40	60	[ramp down]

Figure 7.3: Annealing recipe for the Ge/Au/Ni and Pd/Ge/Au based ohmic contact laying process. See the following text, for further details [*].

All mentioned temperatures were measured at the thin ceramic heating-plate surface (of the annealing oven) using a Pt-1000 sensor glass-welded to the bottom of the surface. AuGe has a melting temperature of 360°C and starts to form alloy at 420°C [9].

The Pd based processing techniques were only tested for shallow ($\approx$ 36-40nm deep) 2DEGs. Both the two recipes of Pd based ohmic contacting process (tested out of many other trials, for both optimal use of metals and gases, and very good and stable ohmic behavior at 4K temperature), yielded very good ohmic contacts offering $\approx$ 2-3 kΩ (likely sheet resistance being few ohms per sq. per contact) between opposite contacts of the star structure discussed in Chapter 3, at 4K temperature.

Lower temperature processing are always beneficial since at higher temperatures, any impurity dopant species might get activated to move into the 2DEG region and can cause a larger impurity profile in the 2DEG and become source sample noise in the nano-structured device. Particularly the use of shallow 2DEG necessitated that, higher temperature processing does not introduce movement of any impurities from far side of the 2DEG and from close to the surface (though it is passivated by thin capping layer which is also etched at near the contacts).

[$*$] The extra layer of Au, helped in reducing pinhole numbers [179] forming at the ohmic contact pads after the annealing step. Reduced pin holes enhanced Au wedge sticking on the bonding pads during wire bonding process. Pinholes (see Appendix C) happened to be one reason suspected for inefficient wedge sticking during gold wire bonding, the other being the surface property of the eutectic alloy so formed which couldn't be verified within the scope of this work. The number of pin holes for the Pd based processing were often less than that of standard ohmic contact process. At times it also helped to etch about 5 - 7 nm (not more) surface layer during the preparation for Pd based ohmic contact laying process, which yielded much better ohmic contacts but at cost of an extra wet processing step.

Top gates structuring process

Step 1. Forming e-beam resist mask

Resist layers	Recipe I		Spin speed for 60s (rpm)	Thickness finally (nm)		Advantage
1st	PMMA - 200k mol. Wt. (@ 4%)		8000	220		Better liftoff due to good undercut
2nd	PMMA - 950k mol. Wt. (@ 3%)		8000			
	Recipe II					
Only one	PMMA - 950k mol. Wt. (@ 3%)		6000	95 ~ 110		
Each layer baked for 7 min at 185 C						

Step 2. E-beam exposure

A beam voltage of 20kV and an aperture of 10 µm was chosen after multiple trials with different apertures and voltages, with correct line/area dose for,

(1) a good optimum between DOF and lens scattering,

(2) allow quick scanning process to avoid over-exposure to the resist,

(3) avoid possible beam penetration damage to the 2DEG and,

(4) allow accurate lithography on the shallow 2DEG surface, all at the same time!

The penetration damage was at times reasoned from higher sample (QPC current, tested at 4K) noise with samples exposed to longer duration/higher beam than not, while the samples were from center & adjacent positions, from same wafer

Step 3. Development and metal deposition

The exposed mask was developed in 1:3 - MIBK:Isopropanol (RT /22°C) for 50s time; e-beam evaporation of Cr : Au at 10 : 80 nm lays the top gates

Figure 7.4: Brief SEM lithography process recipe.

8 Appendix B

We discuss here, the MBE recipe used in the preparation of hybrid nanostructures (see Chapter 3 for more details).

The MBE recipe described in Fig. 8.1, were evaluated for differing spacer thickness (4 iterations, for other constant parameters), differing delta-doping times (3 iterations, for other constant parameters) to yield a good mobility bearing heterostructure. Each time the heterostructure was evaluated for QPC performance (through the hybrid structure) other than determining electron densities and mobilities.

Further iterations were also made to figure out the temperature gradients presented by the sample holder (see text and Fig. 3.8), which were causing poor samples. The 'best' obtained values with the recipe iterations resulted in, for (spacer thickness of 20nm and for the structure of Fig. 3.4), mobility of 2.3 x 10^5 cm^2/Vs and, density of 4.5 x 10^{11} /cm^2, while for the case where the spacer was 23nm thick (other parameters same), the values were , for mobility of 3.56 x 10^5 cm^2/Vs and, density of 3.6 x 10^{11} /cm^2.

	Layer	Temp. profile	Layer thickness / time	
Substrat	GaAs		~450 µm	
Buffer	GaAs	560°C	300 nm	
	GaAs	560°C --> 620°C	100 nm	
	GaAs	620°C	100 nm	
SL (50x)	AlGaAs		7 nm	
	GaAs		3 nm	
Channel (forming layer)	GaAs		1 µm	
Pause			10 sec	
Spacer	AlGaAs		20 nm	
Temp change	at Sample	620°C --> 550°C		
	at Silicon crucible	850°C --> 1068°C		
Pause			30 sec	
Delta-doping	Silicon		300 sec	at 2,23809 x 10^{10} cm^{-2} / s
Barrier	GaAs		2 nm	
	AlAs		2nm	
	AlGaAs		8 nm	
Cap	GaAs		5 nm	

Figure 8.1: Brief MBE process recipe for the shallow 2DEG heterostructure discussed in Chapter 3 [courtesy Dr. Eddy Patrick Rugeramigabo].

9 Appendix C

In this discussion we highlight certain critical issues faced while fabrication of hybrid nano structures and whose reasonings are hypothesised for the discussions in this work.

Faulting of SEM nanostructures due to possible electromigration

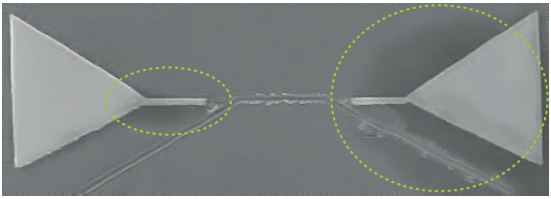

Figure 9.1: The SEM image shows the AFM structured oxidation line along with SEM lithography step markers.

From the SEM image of Fig. 9.1, we see two large pointed markers placed adjacent to the AFM structured oxidation line. The large metal markers placed close to the nanostructure region was also to enhance capacitive coupling of QPC structure sitting on the other side of the AFM structured line. This image is particularly highlighted, for the encircled diffused-darker-than-mesa (under SEM scan) regions formed around the metal markers which are suspected to have been caused through 'electromigration' of certain metal ions diffusing along the surface of GaAs capping layer along the edges of the Cr-Au metal layer and, since this could not be experimentally verified in this work it is a hypothesis at the moment.

This observation was made after between 3 days to a weeks time after doing the lithography. The metal markers are composed of 10 nm Cr and

40 nm Au. This kind of behavior was also observed in other samples in the region of actual top-gate structures. Additionally in any sample where this behavior was observed at around top-gate structures, the sample also showed very high noise relative to noises from samples purely from the 2DEG/heterostructure and, the samples were very sensitive to electrostatics that most top-gated structures blew off at the slightest built of any charges during handling and transport between labs. Length between the ends of the markers (tip to tip) is 2 microns.

Faulting of bonding process possibly due to pinholes at contacts

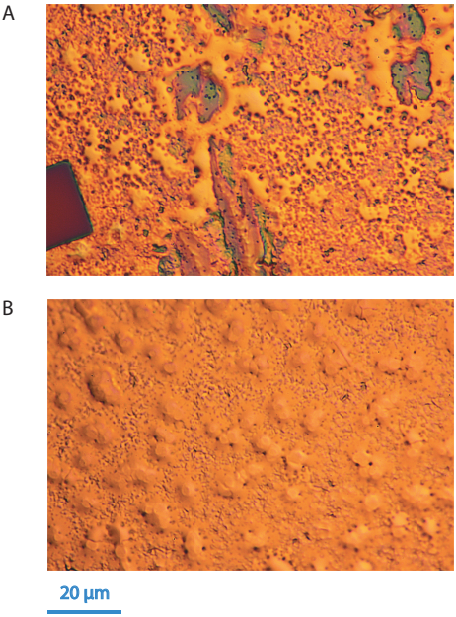

Figure 9.2: Pinhole formation at the Au/Ge/Ni ohmic contacts.

From Fig. 9.2, after the annealing process using Au/Ge/Ni recipe as discussed in Appendix A has been undertaken, a thin-layer gold is deposited

in image (A), and comparatively thicker-layer gold is deposited in image (B). The reduced number of pinholes in image (B), enhanced wedge sticking during the gold wire bonding process. At times, the thin layer metallization also creates small pockets of retracted metal upon annealing which is also visible in image (A).

10 Appendix D

We hypothesize here, certain unproven idea to improve the experimental output, particularly for counting experiments.

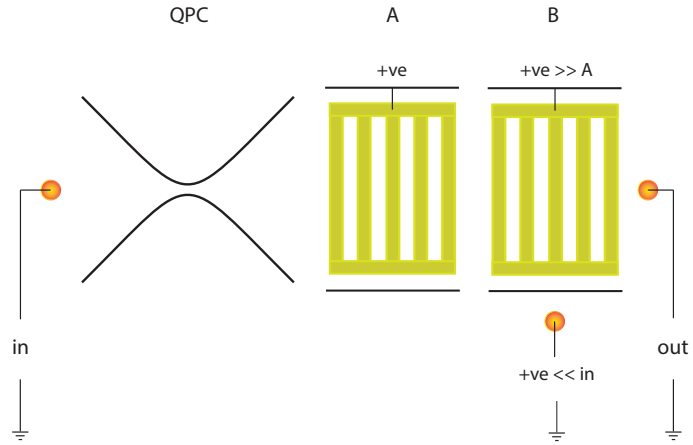

Figure 10.1: Schema of QPC current amplification.

From Fig. 10.1, the current through the QPC (1D region) passes through stages A, B which are biased during the cool down of the sample. Stage A, is maintained at positive bias while cooling down, Stage B, is maintained at comparatively (to Stage A) higher positive bias while cooling down; the output (at 'out') could be tested while applying a very small bias between stage B and the output, as well without applying any bias. The increase in electron density below the top-gates (of the stages A, B) would directly relate

to the increase in the current flowing through the 2D region. This increased current would be then easier to amplify (through external amplifiers) with higher SNR than one without. It needs to be tested how much improvement one could achieve and vary the positive biases at the gates of stages A, B, to test the improvements for a given heterostructure (and as well determine how much the bias current through the 2D region help in improving the current from the QPC). The thermal and RTS noise (after biasing) from the 2D region (of stages A, B) have to be observed too.

11 Appendix E

In this discussion, we show, on how we went ahead in differentiating the rates for tunneling event of $2 \rightarrow 3$ and $2 \rightarrow 1$, since the distributions of both these two tunneling events always had a similar slope.

From, Fig. 5.27 of Chap. 5, we observe that slope of the distribution for events $2 \rightarrow 3$ and $2 \rightarrow 1$ are similar. Since we had extracted the rates through linear fit of the distributions, the rates for these two tunneling events yielded similar values always. Since believe that the tunneling event of $2 \rightarrow 3$ is a separate event from event of $2 \rightarrow 1$, as the former being the situation of the dot being filled by the second electron while the latter being the dot getting emptied of the first electron, we needed to differentiate their rates to plot the figure of 5.21. We shall describe how we went ahead by considering the example of Fig. 5.27 as plotted again here in Fig. 11.1.

From linear fit of the slopes, we get the following rates; for 'green' data, for the transition $3 \rightarrow 2$ as 17230.25 Hz; for 'red' data, for the transition $1 \rightarrow 2$ as 38840.43 Hz; for 'blue' data, for the transition $2 \rightarrow 1$ as 6655.54 Hz; for 'yellow' data, for the transition $2 \rightarrow 3$ as 6630.08 Hz; and for the sum, 'black' data, for the transition $3 \rightarrow 2 \rightarrow 1$ as 6697.56 Hz;

To differentiate the 'yellow' and 'blue' transition rates, we determine the ratios of the distributions of yellow to black and blue to black, as shown in figures of 11.2 and 11.3.

We obtain the ratios of 0.35 and 0.65 as shown in insets of figures of 11.2 and 11.3 respectively. The ratios are then factored with the rate value of the sum distribution ($3 \rightarrow 2 \rightarrow 1$) to yield final rates as, for 'green' data, for the transition $3 \rightarrow 2$ as 17230.25 Hz; for 'red' data, for the transition $1 \rightarrow 2$ as 38840.43 Hz; for 'blue' data, for the transition $2 \rightarrow 1$ as 4353.4 Hz (0.65×6697.56); for 'yellow' data, for the transition $2 \rightarrow 3$ as 2344.1 Hz (0.35×6697.56).

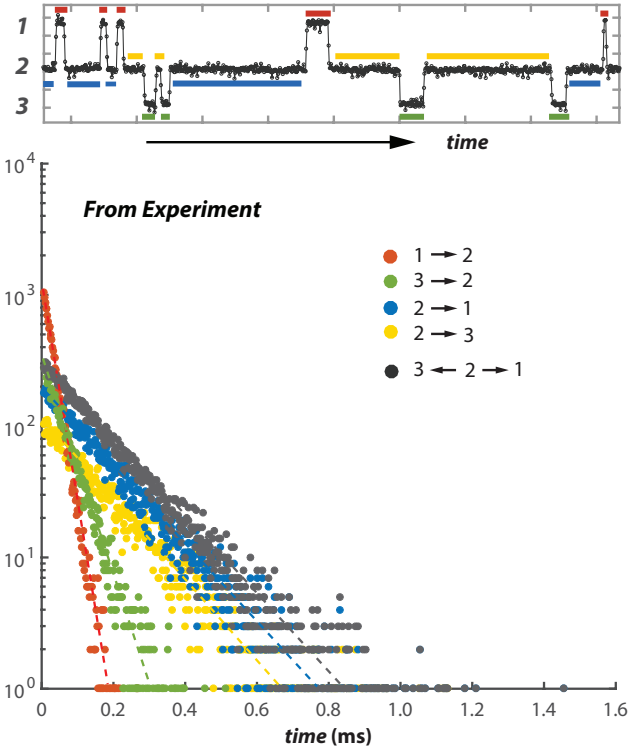

Figure 11.1: Waiting time distribution for a time trace as highlighted in the top, the color of the distributed data corresponds to the state of electron waiting to transit to either state, looking in the forward direction of time and unidirectional transport mechanism.

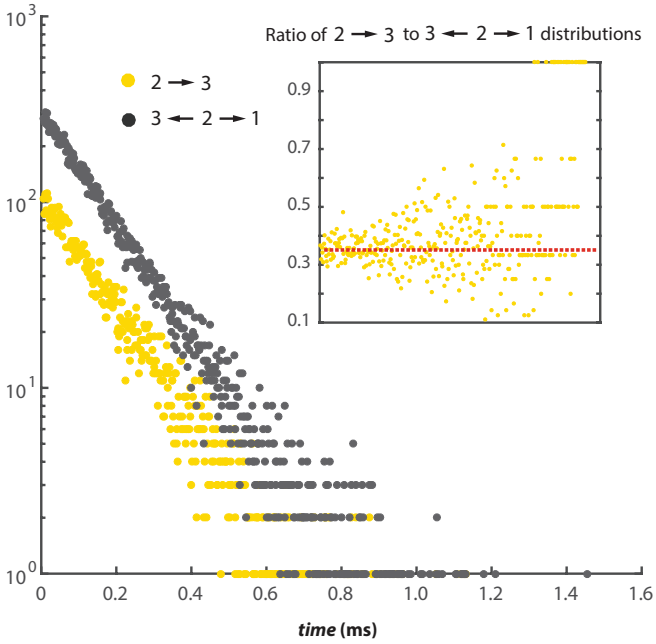

Figure 11.2: Waiting time distributions as discussed in Fig. 11.1 for the transition of $2 \rightarrow 3$ and the sum which is $3 \rightarrow 2 \rightarrow 1$. Inset shows the ratio of the distribution for $2 \rightarrow 3$, with the sum distribution for $3 \rightarrow 2 \rightarrow 1$. The ratio yields a near constant mean value of 0.35.

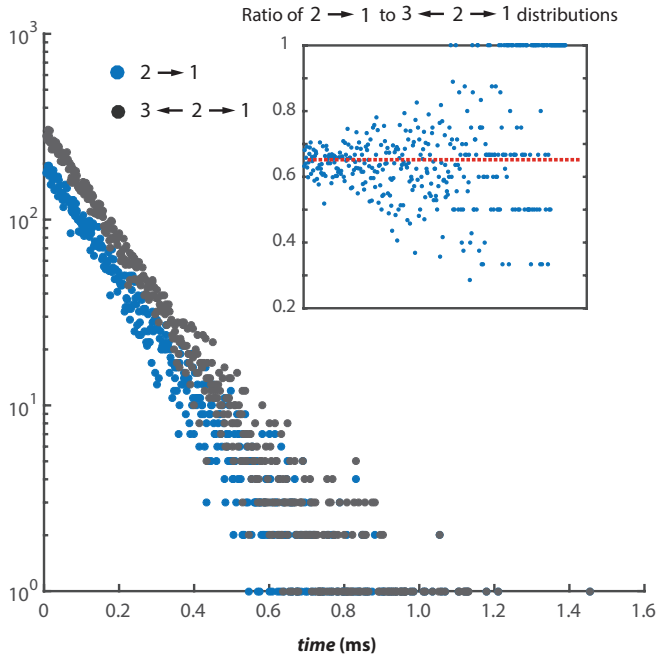

Figure 11.3: Waiting time distributions as discussed in Fig. 11.1 for the transition of $2 \rightarrow 1$ and the sum which is $3 \rightarrow 2 \rightarrow 1$. Inset shows the ratio of the distribution for $2 \rightarrow 1$, with the sum distribution for $3 \rightarrow 2 \rightarrow 1$. The ratio yields a near constant mean value of 0.65.

12 Appendix F

We show here a similar situation of 'Case B' at a further higher dot bias of 4 mV, and with gate-G2 bias at 178 mV. We say the situation at this bias combination is similar to 'case B' of Fig. 5.18, is because, irrespective of the high dot bias, the dot is still witnessing a two occupation state in its energy window and within the region (gate G2 bias) where we observe oscillations only for the tunneling-IN situation and not for the tunneling-OUT situation (see Fig. 5.20). We had not swept the gate G2 bias at this high dot bias situation.

For this situation, we observe for the tunnel-IN condition (Figs. 12.1, 12.2, as linear plots and, 12.5, 12.6 as log-log plots), while no oscillations for the tunnel-OUT condition (Figs. 12.3, 12.4 and 12.7). This particular data was recorded for about less than an hour duration and the length of this data allowed calculation of factorial cumulants for further higher orders for longer time limits with comparatively less influence of noise effects at longer time limits. The data point of G2 bias of 178 mV, is shown with a pale violet dot in Fig. 5.20 which falls in the orange region, which we believe would take similar space in the three occupation probability region at the dot at the bias of 4 mV, and the arguments for observing oscillations for this particular situation is same as was discussed in the last paragraphs (even if there are three occupation probability state at the dot) of section 5.3.2 from Chapter 5. We note here that, the time trace for the current switches is 'predominantly' the same as that shown for 'two occupation probability' state at the dot, as in figure of 5.14B, while very rare events of the third occupation probability was also observed and were considered during the counting process, presumably the rarity of the events had not brought different observations from what had been observed in the discussions of section 5.3.2 of Chapter 5.

We also observe that the Fano factor for the high dot bias of 4 mV and gate-G2 bias of 178 mV is > 1 at shorter time limit for the tunnel-IN situation and not for the tunnel-OUT situation. This behavior is shown in Fig. 12.8.

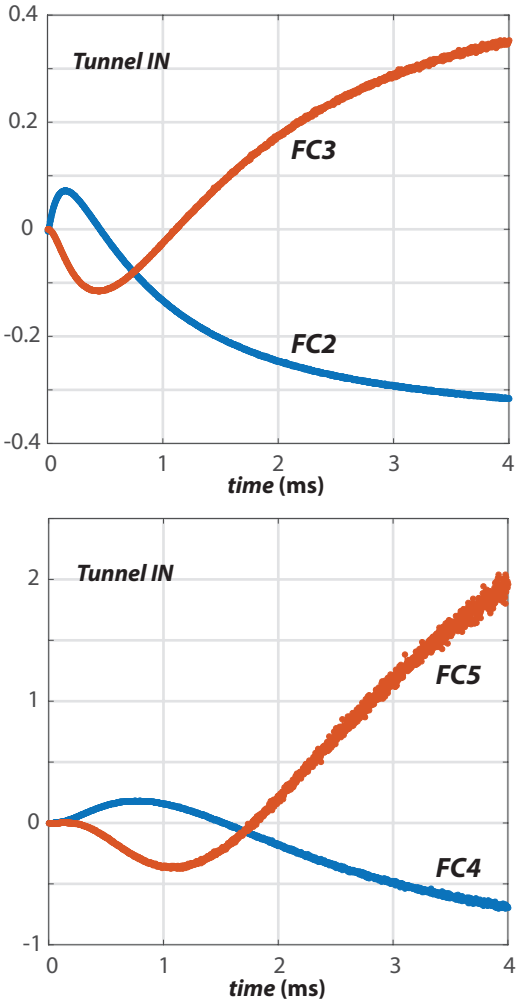

Figure 12.1: First 4 orders of normalized factorial cumulants for Tunnel-IN case, for gate-G2 bias of 178 mV which falls on the 'orange' spot but further at higher dot bias of 4 mV as referrable from Fig. 5.20. The factorial cumulants are normalized over the first one.

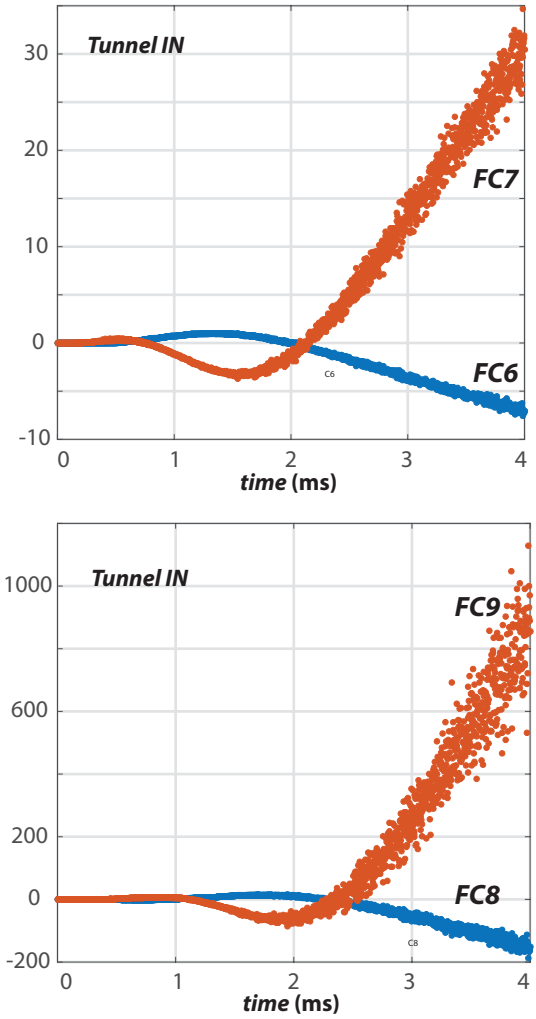

Figure 12.2: Further 4 orders of normalized factorial cumulants for Tunnel-IN case, for gate-G2 bias of 178 mV which falls on the 'orange' spot but further at higher dot bias of 4 mV as referrable from Fig. 5.20. The factorial cumulants are normalized over the first one.

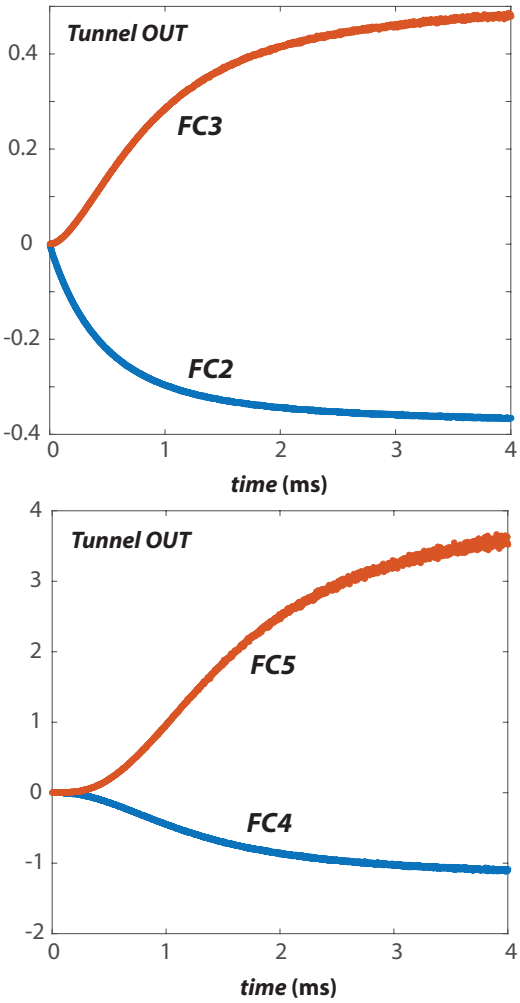

Figure 12.3: First 4 orders of normalized factorial cumulants for Tunnel-OUT case, for gate-G2 bias of 178 mV which falls on the 'orange' spot but further at higher dot bias of 4 mV as referrable from Fig. 5.20. The factorial cumulants are normalized over the first one.

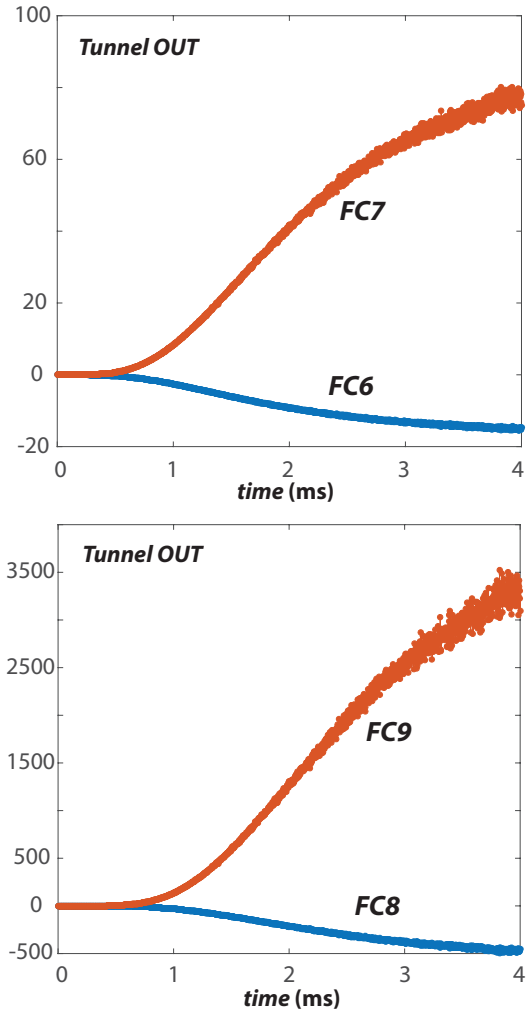

Figure 12.4: Further 4 orders of normalized factorial cumulants for Tunnel-OUT case, for gate-G2 bias of 178 mV which falls on the 'orange' spot but further at higher dot bias of 4 mV as referrable from Fig. 5.20. The factorial cumulants are normalized over the first one.

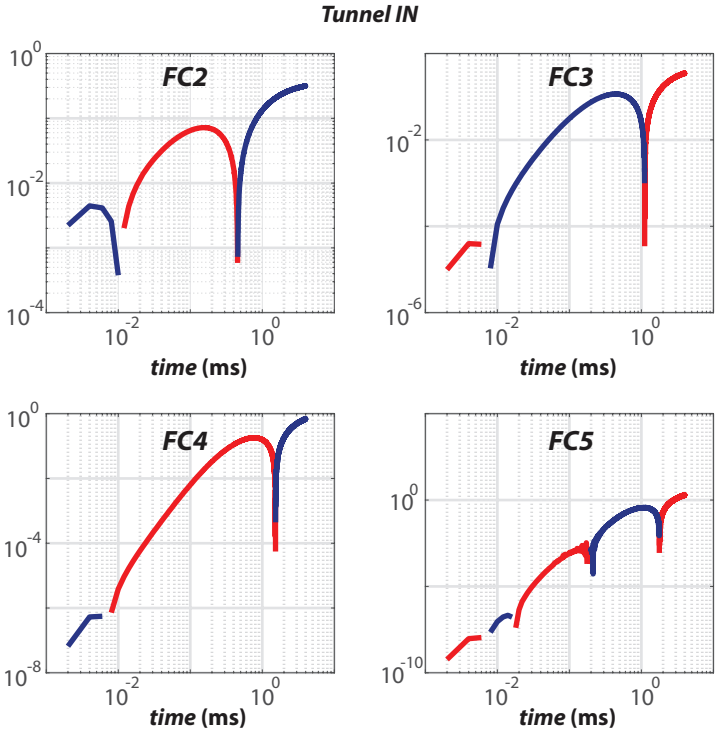

Figure 12.5: First 4 orders of normalized factorial cumulants for Tunnel-IN case, for gate-G2 bias of 178 mV which falls on the 'orange' spot but further at higher dot bias of 4 mV as referrable from Fig. 5.20. The factorial cumulants are normalized over the first one. We observe more oscillations than what we could observe from Fig. 12.1.

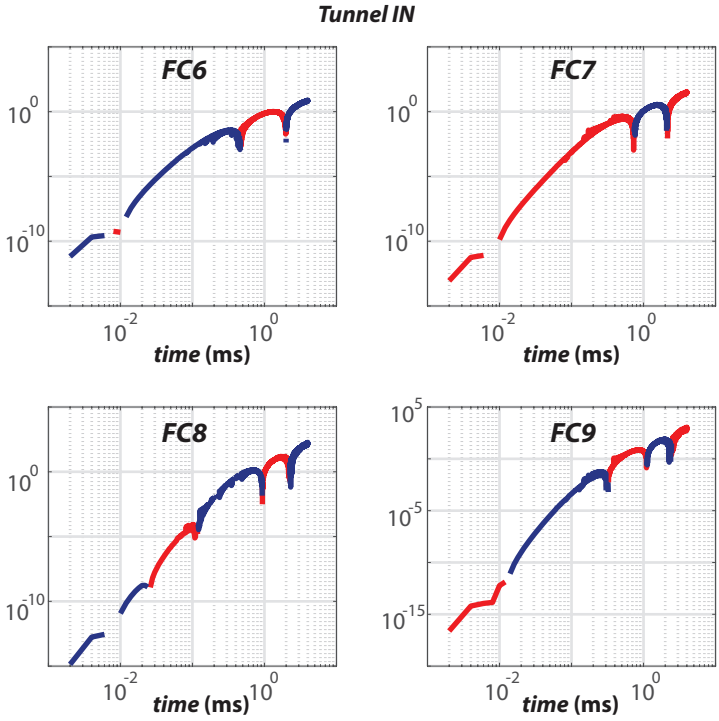

Figure 12.6: Further 4 orders of normalized factorial cumulants for Tunnel-IN case, for gate-G2 bias of 178 mV which falls on the 'orange' spot but further at higher dot bias of 4 mV as referrable from Fig. 5.20. The factorial cumulants are normalized over the first one. We observe more oscillations than what we could observe from Fig. 12.2.

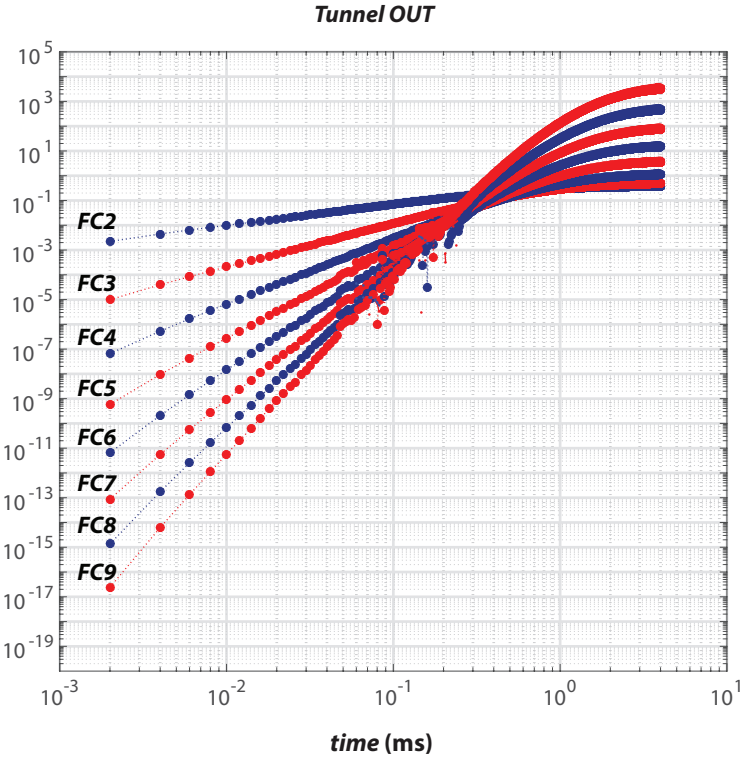

Figure 12.7: Further 9 orders of normalized factorial cumulants for Tunnel-OUT case, for gate-G2 bias of 178 mV which falls on the 'orange' spot but further at higher dot bias of 4 mV as referrable from Fig. 5.20. The factorial cumulants are normalized over the first one. This figure refers to Figs. 12.3 and 12.4.

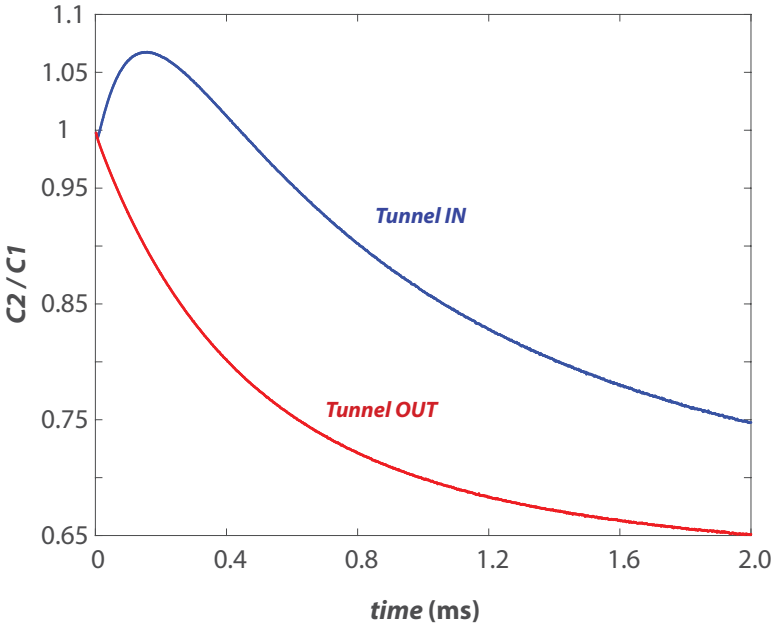

Figure 12.8: 2nd normal cumulant normalized over 1st, or the Fano factor observed over time for the dot bias of 4.0 mV and the gate-G2 voltage of 178 mV discussed for the case of 2nd factorial cumulant discussed in figures of 12.1 and 12.3.

Bibliography

[1] L. L. Sohn, L. P. Kouwenhoven, and G. Schoen, *Mesoscopic Electron Transport* (Springer Netherlands, 2009), ISBN 978-94-015-8839-3.

[2] Y. V. Nazarov and Y. M. Blanter, *Quantum Transport, Introduction to Nanoscience* (Cambridge University Press, 2009), ISBN 9780521832465.

[3] H. Birk, M. J. M. de Jong, and C. Schoenenberger, Phys. Rev. Lett. **75**, 1610 (1995), URL `http://link.aps.org/doi/10.1103/PhysRevLett.75.1610`.

[4] L. Saminadayar, D. C. Glattli, Y. Jin, and B. Etienne, Phys. Rev. Lett. **79**, 2526 (1997), URL `http://link.aps.org/doi/10.1103/PhysRevLett.79.2526`.

[5] R. de Picciotto, M. Reznikov, M. Heiblum, V. Umansky, G. Bunin, and D. Mahalu, Nature **389**, 162 (1997), ISSN 0028-0836, URL `http://dx.doi.org/10.1038/38241`.

[6] S. M. Kendall and A. Stuart, *The Advanced Theory of Statistics* (Charles Griffin and Company Ltd., 1977), ISBN 0852642423.

[7] N. L. Johnson, A. W. Kemp, and S. Kotz, *Univariate Discrete Distributions* (Wiley, 2005), 3rd ed., ISBN 0852642423.

[8] Y. V. Nazarov, *Quantum Noise in Mesoscopic Physics*, vol. 97 of *NATO Science Series* (Springer Netherlands, 2003), ISBN 978-94-010-0089-5.

[9] T. Heinzel, *Mesoscopic Electronics in Solid State Nanostructures* (Wiley-VCH Verlag GmbH, 2007), ISBN 9783527618910.

[10] S. Datta, *Quantum Transport, Atom to Transistor* (Cambridge University Press, 2013), ISBN 9781107632134.

[11] T. Ando, A. B. Fowler, and F. Stern, Rev. Mod. Phys. **54**, 437 (1982), URL http://link.aps.org/doi/10.1103/RevModPhys.54.437.

[12] R. Ismail, M. T. Ahmadi, and S. Anwar, *Advanced Nanoelectronics* (CRC Press, 2012), ISBN 9781439856802.

[13] K. Klitzing, *The Quantum Hall Effect: Poincaré Seminar 2004* (Birkhäuser Basel, Basel, 2005), chap. 25 Years of Quantum Hall Effect (QHE) A Personal View on the Discovery, Physics and Applications of this Quantum Effect, pp. 1–21, ISBN 978-3-7643-7393-1, URL http://dx.doi.org/10.1007/3-7643-7393-8_1.

[14] D. B. Chklovskii, B. I. Shklovskii, and L. I. Glazman, Phys. Rev. B **46**, 4026 (1992), URL http://link.aps.org/doi/10.1103/PhysRevB.46.4026.

[15] B. I. Halperin, Phys. Rev. B **25**, 2185 (1982), URL http://link.aps.org/doi/10.1103/PhysRevB.25.2185.

[16] M. Büttiker, Phys. Rev. B **38**, 9375 (1988), URL http://link.aps.org/doi/10.1103/PhysRevB.38.9375.

[17] S. Tarucha, D. G. Austing, T. Honda, R. J. van der Hage, and L. P. Kouwenhoven, Phys. Rev. Lett. **77**, 3613 (1996), URL http://link.aps.org/doi/10.1103/PhysRevLett.77.3613.

[18] B. J. van Wees, H. van Houten, C. W. J. Beenakker, J. G. Williamson, L. P. Kouwenhoven, D. van der Marel, and C. T. Foxon, Phys. Rev. Lett. **60**, 848 (1988), URL http://link.aps.org/doi/10.1103/PhysRevLett.60.848.

[19] D. A. Wharam, T. J. Thornton, R. Newbury, M. Pepper, H. Ahmed, J. E. F. Frost, D. G. Hasko, D. C. Peacock, D. A. Ritchie, and G. A. C. Jones, Journal of Physics C: Solid State Physics **21**, L209 (1988), URL http://stacks.iop.org/0022-3719/21/i=8/a=002.

[20] L. P. Kouwenhoven, D. G. Austing, and S. Tarucha, Reports on Progress in Physics **64**, 701 (2001), URL http://stacks.iop.org/0034-4885/64/i=6/a=201.

[21] V. Fock, Z. Phys. **47** (1928).

[22] C. Darwin, Proceedings of the Cambridge Philosophical Society **27**, 86 (1931).

[23] P. Schmelcher and W. Schweizer, *Atoms and Molecules in Strong External Fields* (Springer US, 2002), ISBN 978-0-306-45811-8.

[24] R. Landauer, IBM Journal of Research and Development **1**, 223 (1957), ISSN 0018-8646.

[25] R. Landauer, IBM Journal of Research and Development **32**, 306 (1988), ISSN 0018-8646.

[26] M. Büttiker, Phys. Rev. Lett. **57**, 1761 (1986), URL `http://link.aps.org/doi/10.1103/PhysRevLett.57.1761`.

[27] M. Büttiker, IBM J. Res. Dev. **32**, 317 (1988), ISSN 0018-8646, URL `http://dx.doi.org/10.1147/rd.323.0317`.

[28] M. Büttiker, Phys. Rev. Lett. **65**, 2901 (1990), URL `http://link.aps.org/doi/10.1103/PhysRevLett.65.2901`.

[29] M. Büttiker, Phys. Rev. B **46**, 12485 (1992), URL `http://link.aps.org/doi/10.1103/PhysRevB.46.12485`.

[30] Y. Imry and R. Landauer, Rev. Mod. Phys. **71**, S306 (1999), URL `http://link.aps.org/doi/10.1103/RevModPhys.71.S306`.

[31] M. Büttiker, Phys. Rev. B **41**, 7906 (1990), URL `http://link.aps.org/doi/10.1103/PhysRevB.41.7906`.

[32] W. Schottky, Ann. Phys. (Leipzig) **57**, 541 (1918).

[33] J. R. Pierce, Bell System Technical Journal **27**, 158 (1948).

[34] R. Landauer, Nature **392**, 658 (1998), ISSN 0028-0836, 10.1038/33551, URL `http://dx.doi.org/10.1038/33551`.

[35] Y. Blanter and M. Büttiker, Physics Reports **336**, 1 (2000), ISSN 0370-1573, URL `http://www.sciencedirect.com/science/Article/pii/S0370157399001234`.

[36] J. H. Davies, P. Hyldgaard, S. Hershfield, and J. W. Wilkins, Phys. Rev. B **46**, 9620 (1992), URL `http://link.aps.org/doi/10.1103/PhysRevB.46.9620`.

[37] A. Nauen, F. Hohls, J. Könemann, and R. J. Haug, Phys. Rev. B **69**, 113316 (2004), URL http://link.aps.org/doi/10.1103/PhysRevB.69.113316.

[38] R. Landauer, Phys. Rev. B **47**, 16427 (1993), URL http://link.aps.org/doi/10.1103/PhysRevB.47.16427.

[39] C. W. J. Beenakker and M. Büttiker, Phys. Rev. B **46**, 1889 (1992), URL http://link.aps.org/doi/10.1103/PhysRevB.46.1889.

[40] S. Washburn, R. J. Haug, K. Y. Lee, and J. M. Hong, Phys. Rev. B **44**, 3875 (1991), URL http://link.aps.org/doi/10.1103/PhysRevB.44.3875.

[41] M. Reznikov, M. Heiblum, H. Shtrikman, and D. Mahalu, Phys. Rev. Lett. **75**, 3340 (1995), URL http://link.aps.org/doi/10.1103/PhysRevLett.75.3340.

[42] A. Kumar, L. Saminadayar, D. C. Glattli, Y. Jin, and B. Etienne, Phys. Rev. Lett. **76**, 2778 (1996), URL http://link.aps.org/doi/10.1103/PhysRevLett.76.2778.

[43] Y. Ji, Y. Chung, D. Sprinzak, M. Heiblum, D. Mahalu, and H. Shtrikman, Nature **422**, 415 (2003), ISSN 0028-0836, 10.1038/nature01503, URL http://dx.doi.org/10.1038/nature01503.

[44] P. Roulleau, F. Portier, P. Roche, A. Cavanna, G. Faini, U. Gennser, and D. Mailly, Phys. Rev. Lett. **100**, 126802 (2008), URL http://link.aps.org/doi/10.1103/PhysRevLett.100.126802.

[45] L. V. Litvin, A. Helzel, H.-P. Tranitz, W. Wegscheider, and C. Strunk, Phys. Rev. B **78**, 075303 (2008), URL http://link.aps.org/doi/10.1103/PhysRevB.78.075303.

[46] L. G. B., JETP Letters **49**, 592 (1989).

[47] D. Kambly, *Counting statistics in interacting nano-scale conductors* (Univ. Genéve, 2014), iD: unige:34909, URL http://archive-ouverte.unige.ch/unige:34909.

[48] C. Röthig, G. Schön, and M. Vojta, *CFN Lectures on Functional Nanostructures - Volume 2: Nanoelectronics*, Lecture Notes in Physics (Springer Berlin Heidelberg, 2011), ISBN 9783642143779, URL https://books.google.de/books?id=NvgaswEACAAJ.

[49] S. Hershfield, J. H. Davies, P. Hyldgaard, C. J. Stanton, and J. W. Wilkins, Phys. Rev. B **47**, 1967 (1993), URL http://link.aps.org/doi/10.1103/PhysRevB.47.1967.

[50] L. Y. Chen and C. S. Ting, Phys. Rev. B **43**, 4534 (1991), URL http://link.aps.org/doi/10.1103/PhysRevB.43.4534.

[51] M. Abramowitz and I. A. Stegun, *Handbook of Mathematical Functions* (Dover Publications, New York, 1972).

[52] Y. Bomze, G. Gershon, D. Shovkun, L. S. Levitov, and M. Reznikov, Phys. Rev. Lett. **95**, 176601 (2005), URL http://link.aps.org/doi/10.1103/PhysRevLett.95.176601.

[53] B. Reulet, J. Senzier, and D. E. Prober, Phys. Rev. Lett. **91**, 196601 (2003), URL http://link.aps.org/doi/10.1103/PhysRevLett.91.196601.

[54] L. L. S. and L. G. B., JETP Letters **58**, 230 (1993).

[55] I. D. A. and L. L. S., JETP Letters **58**, 461 (1993).

[56] W. Belzig and Y. V. Nazarov, Phys. Rev. Lett. **87**, 197006 (2001), URL http://link.aps.org/doi/10.1103/PhysRevLett.87.197006.

[57] Y. V. Nazarov and D. A. Bagrets, Phys. Rev. Lett. **88**, 196801 (2002), URL http://link.aps.org/doi/10.1103/PhysRevLett.88.196801.

[58] A. H. Steinbach, J. M. Martinis, and M. H. Devoret, Phys. Rev. Lett. **76**, 3806 (1996), URL http://link.aps.org/doi/10.1103/PhysRevLett.76.3806.

[59] R. J. Schoelkopf, P. J. Burke, A. A. Kozhevnikov, D. E. Prober, and M. J. Rooks, Phys. Rev. Lett. **78**, 3370 (1997), URL http://link.aps.org/doi/10.1103/PhysRevLett.78.3370.

[60] R. C. Liu, B. Odom, Y. Yamamoto, and S. Tarucha, Nature **391**, 263 (1998), ISSN 0028-0836, 10.1038/34611, URL http://dx.doi.org/10.1038/34611.

[61] E. Comforti, Y. C. Chung, M. Heiblum, V. Umansky, and D. Mahalu, Nature **416**, 515 (2002), ISSN 0028-0836, 10.1038/416515a, URL http://dx.doi.org/10.1038/416515a.

[62] E. F. Schubert, *Delta Doping of Semiconductors* (Cambridge University Press, 1996).

[63] E. F. Schubert, *Doping in III-V Semiconductors:* (Cambridge University Press, Cambridge, 1993), ISBN 9780511599828, URL https://www.cambridge.org/core/books/doping-in-iii-v-semiconductors/F05AEE3D3139B07CE4F3556B1360B869.

[64] E. F. Schubert, T. D. Harris, J. E. Cunningham, and W. Jan, Phys. Rev. B **39**, 11011 (1989), URL http://link.aps.org/doi/10.1103/PhysRevB.39.11011.

[65] T. Kuech, *Handbook of Crystal Growth, 2nd Edn.* (Elsevier, 2014), ISBN 9780444633040.

[66] J. P. Harrang, R. J. Higgins, R. K. Goodall, P. R. Jay, M. Laviron, and P. Delescluse, Phys. Rev. B **32**, 8126 (1985), URL http://link.aps.org/doi/10.1103/PhysRevB.32.8126.

[67] G. Bergmann, Phys. Rev. B **28**, 2914 (1983), URL http://link.aps.org/doi/10.1103/PhysRevB.28.2914.

[68] J. Tersoff, Phys. Rev. B **30**, 4874 (1984), URL http://link.aps.org/doi/10.1103/PhysRevB.30.4874.

[69] I. H. Tan, G. L. Snider, L. D. Chang, and E. L. Hu, Journal of Applied Physics **68**, 4071 (1990), URL http://scitation.aip.org/content/aip/journal/jap/68/8/10.1063/1.346245.

[70] G. L. Snider, I. H. Tan, and E. L. Hu, Journal of Applied Physics **68**, 2849 (1990), URL http://scitation.aip.org/content/aip/journal/jap/68/6/10.1063/1.346443.

[71] B. L. Sharma, *Metal-Semiconductor Schottky Barrier Junctions and Their Applications* (Springer US, 1984), ISBN 978-1-4684-4657-9.

[72] A. Firrincieli, E. Simoen, M. Meuris, and C. Claeys, Proceedings of the Semiconductor Advances for Future Electronics Workshop - SAFE pp. 464–467 (2008).

[73] M. L. Lovejoy, A. J. Howard, K. R. Zavadil, D. J. Rieger, and R. J. Shu, J. Vac. Sci. Technol. **13**, 758 (1995).

[74] D. L. Partin, A. G. Milnes, and L. F. Vassamillet, Journal of Electronic Materials **7**, 279 (1978).

[75] F. Lehmann, G. Richter, T. Borzenko, V. Hock, G. Schmidt, and L. Molenkamp, Microelectronic Engineering **65**, 327 (2003).

[76] G. Binnig and H. Rohrer, IBM J. Res. Dev. **44**, 279 (2000), ISSN 0018-8646, URL http://dx.doi.org/10.1147/rd.441.0279.

[77] L. Gross, F. Mohn, N. Moll, B. Schuler, A. Criado, E. Guitián, D. Peña, A. Gourdon, and G. Meyer, Science **337**, 1326 (2012), http://www.sciencemag.org/content/337/6100/1326.full.pdf, URL http://www.sciencemag.org/content/337/6100/1326.abstract.

[78] L. Gross, F. Mohn, N. Moll, P. Liljeroth, and G. Meyer, Science **325**, 1110 (2009), http://www.sciencemag.org/content/325/5944/1110.full.pdf, URL http://www.sciencemag.org/content/325/5944/1110.abstract.

[79] V. Cambel, J. Martaus, J. Soltys, R. Kudela, and D. Gregusova, Ultramicroscopy **108**, 1021 (2008), ISSN 0304-3991 (Print) 0304-3991 (Linking), URL http://www.ncbi.nlm.nih.gov/pubmed/18565663.

[80] N. J. Curson, R. Nemutudi, N. J. Appleyard, M. Pepper, D. A. Ritchie, and G. A. C. Jones, Applied Physics Letters **78**, 3466 (2001), ISSN 00036951.

[81] C. Fricke, M. C. Rogge, B. Harke, M. Reinwald, W. Wegscheider, F. Hohls, and R. J. Haug, Physical Review B **72** (2005), ISSN 1098-01211550-235X.

[82] C. Fricke, J. Regul, F. Hohls, D. Reuter, A. D. Wieck, and R. J. Haug, Physica E: Low-dimensional Systems and Nanostructures **34**, 519 (2006), ISSN 13869477.

[83] F. Hohls, C. Fricke, and R. J. Haug, Physica E: Low-dimensional Systems and Nanostructures **40**, 1760 (2008), ISSN 13869477.

[84] M. Huefner, S. Schnez, B. Kueng, T. Ihn, M. Reinwald, W. Wegscheider, and K. Ensslin, Nanotechnology **22**, 295306 (2011), ISSN 1361-6528 (Electronic) 0957-4484 (Linking), URL http://www.ncbi.nlm.nih.gov/pubmed/21693803.

[85] D. Köhler, M. Knop, U. Kunze, D. Reuter, and A. D. Wieck, Semiconductor Science and Technology **20**, 140 (2005), ISSN 0268-12421361-6641.

[86] M. C. Rogge, C. Fühner, U. F. Keyser, R. J. Haug, M. Bichler, G. Abstreiter, and W. Wegscheider, Applied Physics Letters **83**, 1163 (2003), ISSN 00036951.

[87] S. Gustavsson, R. Leturcq, B. Simovic, R. Schleser, T. Ihn, P. Studerus, K. Ensslin, D. C. Driscoll, and A. C. Gossard, Physical Review Letters **96** (2006), ISSN 0031-90071079-7114.

[88] M. Bartošík, D. Škoda, O. Tomanec, R. Kalousek, P. Jánský, J. Zlámal, J. Spousta, P. Dub, and T. Šikola, Physical Review B **79**, 195406 (2009), URL http://dx.doi.org/10.1103/PhysRevB.79.195406.

[89] E. K. Tanyi, R. M. Kolagani, P. Srivastava, W. Vanderlinde, G. Yong, C. Stumpf, and D. Schaefer, AIP Advances **4**, 127129 (2014), URL http://dx.doi.org/10.1063/1.4904427.

[90] M. Lazzarino, M. Padovani, G. Mori, L. Sorba, M. Fanetti, and M. Sancrotti, Chemical Physics Letters **402**, 155 (2005), ISSN 0009-2614, URL http://www.sciencedirect.com/science/Article/pii/S0009261404019554.

[91] J. J. Ahn, K. S. Moon, and S. M. Koo, Nanoscale Res Lett **6**, 550 (2011), ISSN 1931-7573 (Print).

[92] W.-P. Huang, H.-H. Cheng, S.-R. Jian, D.-S. Chuu, J.-Y. Hsieh, C.-M. Lin, and M.-S. Chiang, Nanotechnology **17**, 3838 (2006), URL http://stacks.iop.org/0957-4484/17/i=15/a=039.

[93] S.-R. Jian, T.-H. Fang, and D.-S. Chuu, Journal of Physics D: Applied Physics **38**, 2424 (2005), URL http://stacks.iop.org/0022-3727/38/i=14/a=019.

[94] Y. Okada, Y. Iuchi, and M. Kawabe, Journal of Applied Physics **87**, 8754 (2000), URL http://scitation.aip.org/content/aip/journal/jap/87/12/10.1063/1.373606.

[95] M. Ishii and K. Matsumoto, Japanese Journal of Applied Physics **34**, 1329 (1995), provided by the SAO/NASA Astrophysics Data System, URL http://adsabs.harvard.edu/abs/1995JaJAP..34.1329I.

[96] P. Avouris, R. Martel, T. Hertel, and R. Sandstrom, Applied Physics A **66**, S659 (1998), ISSN 0947-8396, URL http://dx.doi.org/10.1007/s003390051218.

[97] C. Fricke, M. C. Rogge, B. Harke, M. Reinwald, W. Wegscheider, F. Hohls, and R. J. Haug, Physical Review B **72** (2005), ISSN 1098-01211550-235X.

[98] M. Field, C. G. Smith, M. Pepper, D. A. Ritchie, J. E. F. Frost, G. A. C. Jones, and D. G. Hasko, Phys. Rev. Lett. **70**, 1311 (1993), URL http://link.aps.org/doi/10.1103/PhysRevLett.70.1311.

[99] R. Schleser, E. Ruh, T. Ihn, K. Ensslin, D. C. Driscoll, and A. C. Gossard, Applied Physics Letters **85**, 2005 (2004), URL http://scitation.aip.org/content/aip/journal/apl/85/11/10.1063/1.1784875.

[100] J. M. Elzerman, R. Hanson, L. H. Willems van Beveren, B. Witkamp, L. M. K. Vandersypen, and L. P. Kouwenhoven, Nature **430**, 431 (2004), ISSN 0028-0836, 10.1038/nature02693, URL http://dx.doi.org/10.1038/nature02693.

[101] L. DiCarlo, H. J. Lynch, A. C. Johnson, L. I. Childress, K. Crockett, C. M. Marcus, M. P. Hanson, and A. C. Gossard, Phys. Rev. Lett. **92**, 226801 (2004), URL http://link.aps.org/doi/10.1103/PhysRevLett.92.226801.

[102] J. R. Petta, A. C. Johnson, J. M. Taylor, E. A. Laird, A. Yacoby, M. D. Lukin, C. M. Marcus, M. P. Hanson, and A. C. Gossard, Science **309**, 2180 (2005), ISSN 0036-8075, http://science.sciencemag.org/content/309/5744/2180.full.pdf, URL http://science.sciencemag.org/content/309/5744/2180.

[103] C. Flindt, C. Fricke, F. Hohls, T. Novotný, K. Netočný, T. Brandes, and R. J. Haug, Proceedings of the National Academy of Sciences **106**, 10116 (2009), http://www.pnas.org/content/106/25/10116.full.pdf, URL http://www.pnas.org/content/106/25/10116.abstract.

[104] C. Fricke, *Der Quantenpunktkontakt als Ladungsdetektor in der Transportspektroskopie* (Leibniz Universität Hannover, 2009), URL http://edok01.tib.uni-hannover.de/edoks/e01dh09/600443175.pdf.

[105] Y. P. Li, D. C. Tsui, J. J. Heremans, J. A. Simmons, and G. W. Weimann, Applied Physics Letters **57**, 774 (1990).

[106] A. D. Bell, *Noise and the Solid State* (Halsted Press, New York, 1985), ISBN 9780470202296.

[107] D. Harbusch, D. Taubert, H. P. Tranitz, W. Wegscheider, and S. Ludwig, Phys. Rev. Lett. **104**, 196801 (2010), URL `http://link.aps.org/doi/10.1103/PhysRevLett.104.196801`.

[108] K. Horibe, T. Kodera, and S. Oda, Applied Physics Letters **106**, 053119 (2015).

[109] B. A. Turek, K. W. Lehnert, A. Clerk, D. Gunnarsson, K. Bladh, P. Delsing, and R. J. Schoelkopf, Phys. Rev. B **71**, 193304 (2005), URL `http://link.aps.org/doi/10.1103/PhysRevB.71.193304`.

[110] C. W. J. Beenakker, M. Kindermann, and Y. V. Nazarov, Physical Review Letters **90** (2003), ISSN 0031-90071079-7114.

[111] V. S. Khrapai, S. Ludwig, J. P. Kotthaus, H. P. Tranitz, and W. Wegscheider, Phys. Rev. Lett. **97**, 176803 (2006), URL `http://link.aps.org/doi/10.1103/PhysRevLett.97.176803`.

[112] L. Gaudreau, A. Kam, G. Granger, S. A. Studenikin, P. Zawadzki, and A. S. Sachrajda, Applied Physics Letters **95**, 193101 (2009), ISSN 00036951.

[113] G. J. Schinner, H. P. Tranitz, W. Wegscheider, J. P. Kotthaus, and S. Ludwig, Phys. Rev. Lett. **102**, 186801 (2009), URL `http://link.aps.org/doi/10.1103/PhysRevLett.102.186801`.

[114] B. Küng, C. Rössler, M. Beck, M. Marthaler, D. S. Golubev, Y. Utsumi, T. Ihn, and K. Ensslin, Physical Review X **2** (2012), ISSN 2160-3308.

[115] F. D. Parmentier, A. Anthore, S. Jezouin, H. le Sueur, U. Gennser, A. Cavanna, D. Mailly, and F. Pierre, Nature Physics **7**, 935 (2011), ISSN 1745-24731745-2481.

[116] Y. Utsumi, D. S. Golubev, M. Marthaler, K. Saito, T. Fujisawa, and G. Schön, Physical Review B **81** (2010), ISSN 1098-01211550-235X.

[117] G. Granger, D. Taubert, C. E. Young, L. Gaudreau, A. Kam, S. A. Studenikin, P. Zawadzki, D. Harbusch, D. Schuh, W. Wegscheider, et al., Nat. Phys. **8**, 522 (2012), ISSN 1745-2473, 10.1038/nphys2326, URL http://dx.doi.org/10.1038/nphys2326.

[118] J. S. Blakemore, Journal of Applied Physics **53**, R123 (1982), URL http://scitation.aip.org/content/aip/journal/jap/53/10/10.1063/1.331665.

[119] H. Karl, W. Dietsche, A. Fischer, and K. Ploog, Phys. Rev. Lett. **61**, 2360 (1988), URL http://link.aps.org/doi/10.1103/PhysRevLett.61.2360.

[120] O. Naaman and J. Aumentado, Phys. Rev. Lett. **96**, 100201 (2006), URL http://link.aps.org/doi/10.1103/PhysRevLett.96.100201.

[121] S. Gustavsson, R. Leturcq, T. Ihn, K. Ensslin, M. Reinwald, and W. Wegscheider, Phys. Rev. B **75**, 075314 (2007), URL http://link.aps.org/doi/10.1103/PhysRevB.75.075314.

[122] C. Flindt, A. Braggio, and T. Novotný, AIP Conference Proceedings **922**, 531 (2007), URL http://scitation.aip.org/content/aip/proceeding/aipcp/10.1063/1.2759735.

[123] C. Emary, Philosophical Transactions of the Royal Society of London A: Mathematical, Physical and Engineering Sciences **371** (2013), ISSN 1364-503X, http://rsta.royalsocietypublishing.org/content/371/1999/20120468.full.pdf, URL http://rsta.royalsocietypublishing.org/content/371/1999/20120468.

[124] T. Brandes, Annalen der Physik **17**, 477 (2008), ISSN 1521-3889, URL http://dx.doi.org/10.1002/andp.200810306.

[125] D. Kambly, C. Flindt, and M. Büttiker, Phys. Rev. B **83**, 075432 (2011), URL http://link.aps.org/doi/10.1103/PhysRevB.83.075432.

[126] S. Pilgram, A. N. Jordan, E. V. Sukhorukov, and M. Büttiker, Phys. Rev. Lett. **90**, 206801 (2003), URL http://link.aps.org/doi/10.1103/PhysRevLett.90.206801.

[127] K. E. Nagaev, S. Pilgram, and M. Büttiker, Phys. Rev. Lett. **92**, 176804 (2004), URL http://link.aps.org/doi/10.1103/PhysRevLett.92.176804.

[128] D. A. Bagrets and Y. V. Nazarov, Phys. Rev. B **67**, 085316 (2003), URL http://link.aps.org/doi/10.1103/PhysRevB.67.085316.

[129] C. Emary, D. Marcos, R. Aguado, and T. Brandes, Phys. Rev. B **76**, 161404 (2007), URL http://link.aps.org/doi/10.1103/PhysRevB.76.161404.

[130] C. Flindt, T. Novotný, A. Braggio, M. Sassetti, and A.-P. Jauho, Phys. Rev. Lett. **100**, 150601 (2008), URL http://link.aps.org/doi/10.1103/PhysRevLett.100.150601.

[131] C. Flindt, T. Novotný, A. Braggio, and A.-P. Jauho, Phys. Rev. B **82**, 155407 (2010), URL http://link.aps.org/doi/10.1103/PhysRevB.82.155407.

[132] M. Esposito, U. Harbola, and S. Mukamel, Rev. Mod. Phys. **81**, 1665 (2009), URL http://link.aps.org/doi/10.1103/RevModPhys.81.1665.

[133] R. Sánchez, R. López, D. Sánchez, and M. Büttiker, Phys. Rev. Lett. **104**, 076801 (2010), URL http://link.aps.org/doi/10.1103/PhysRevLett.104.076801.

[134] M. Vanević, Y. V. Nazarov, and W. Belzig, Phys. Rev. Lett. **99**, 076601 (2007), URL http://link.aps.org/doi/10.1103/PhysRevLett.99.076601.

[135] M. Vanević, Y. V. Nazarov, and W. Belzig, Phys. Rev. B **78**, 245308 (2008), URL http://link.aps.org/doi/10.1103/PhysRevB.78.245308.

[136] N. Ubbelohde, C. Fricke, C. Flindt, F. Hohls, and R. J. Haug, Nat Commun **3**, 612 (2012), 10.1038/ncomms1620, URL http://dx.doi.org/10.1038/ncomms1620.

[137] W. Lu, Z. Ji, L. Pfeiffer, K. W. West, and A. J. Rimberg, Nature **423**, 422 (2003), ISSN 0028-0836, 10.1038/nature01642, URL http://dx.doi.org/10.1038/nature01642.

[138] J. Bylander, T. Duty, and P. Delsing, Nature **434**, 361 (2005), ISSN 0028-0836, 10.1038/nature03375, URL http://dx.doi.org/10.1038/nature03375.

[139] T. Fujisawa, T. Hayashi, R. Tomita, and Y. Hirayama, Science **312**, 1634 (2006), ISSN 0036-8075, http://science.sciencemag.org/content/312/5780/1634.full.pdf, URL http://science.sciencemag.org/content/312/5780/1634.

[140] E. V. Sukhorukov, A. N. Jordan, S. Gustavsson, R. Leturcq, T. Ihn, and K. Ensslin, Nat Phys **3**, 243 (2007), ISSN 1745-2473, 10.1038/nphys564, URL http://dx.doi.org/10.1038/nphys564.

[141] A. V. Timofeev, M. Meschke, J. T. Peltonen, T. T. Heikkilä, and J. P. Pekola, Phys. Rev. Lett. **98**, 207001 (2007), URL http://link.aps.org/doi/10.1103/PhysRevLett.98.207001.

[142] G. Gershon, Y. Bomze, E. V. Sukhorukov, and M. Reznikov, Phys. Rev. Lett. **101**, 016803 (2008), URL http://link.aps.org/doi/10.1103/PhysRevLett.101.016803.

[143] J. Gabelli and B. Reulet, Phys. Rev. B **80**, 161203 (2009), URL http://link.aps.org/doi/10.1103/PhysRevB.80.161203.

[144] C. Fricke, F. Hohls, N. Sethubalasubramanian, L. Fricke, and R. J. Haug, Applied Physics Letters **96** (2010).

[145] S. Gustavsson, R. Leturcq, M. Studer, I. Shorubalko, T. Ihn, K. Ensslin, D. Driscoll, and A. Gossard, Surface Science Reports **64**, 191 (2009), ISSN 0167-5729, URL http://www.sciencedirect.com/science/Article/pii/S0167572909000193.

[146] J. P. Pekola, O.-P. Saira, V. F. Maisi, A. Kemppinen, M. Möttönen, Y. A. Pashkin, and D. V. Averin, Rev. Mod. Phys. **85**, 1421 (2013), URL http://link.aps.org/doi/10.1103/RevModPhys.85.1421.

[147] E. A. Zibik, T. Grange, B. A. Carpenter, N. E. Porter, R. Ferreira, G. Bastard, D. Stehr, S. Winnerl, M. Helm, H. Y. Liu, et al., Nat Mater **8**, 803 (2009), ISSN 1476-1122, 10.1038/nmat2511, URL http://dx.doi.org/10.1038/nmat2511.

[148] J. Aghassi, M. H. Hettler, and G. Schön, Applied Physics Letters **92** (2008).

[149] I. Weymann and J. Barnaś, Phys. Rev. B **77**, 075305 (2008), URL http://link.aps.org/doi/10.1103/PhysRevB.77.075305.

[150] G. Kiesslich, E. Schöll, F. Hohls, and R. J. Haug, physica status solidi (c) **5**, 166 (2008), ISSN 1610-1642, URL http://dx.doi.org/10.1002/pssc.200776502.

[151] O. Zarchin, Y. C. Chung, M. Heiblum, D. Rohrlich, and V. Umansky, Phys. Rev. Lett. **98**, 066801 (2007), URL http://link.aps.org/doi/10.1103/PhysRevLett.98.066801.

[152] M. Dineykhan and R. G. Nazmitdinov, Phys. Rev. B **55**, 13707 (1997), URL http://link.aps.org/doi/10.1103/PhysRevB.55.13707.

[153] S. M. Cronenwett, T. H. Oosterkamp, and L. P. Kouwenhoven, Science **281**, 540 (1998), ISSN 0036-8075, http://science.sciencemag.org/content/281/5376/540.full.pdf, URL http://science.sciencemag.org/content/281/5376/540.

[154] S. Sasaki, S. De Franceschi, J. M. Elzerman, W. G. van der Wiel, M. Eto, S. Tarucha, and L. P. Kouwenhoven, Nature **405**, 764 (2000), ISSN 0028-0836, 10.1038/35015509, URL http://dx.doi.org/10.1038/35015509.

[155] Y. E. Kim and A. L. Zubarev, Physics Letters A **289**, 155 (2001), URL http://www.sciencedirect.com/science/Article/pii/S0375960101006041.

[156] Y. Utsumi, Phys. Rev. B **75**, 035333 (2007), URL http://link.aps.org/doi/10.1103/PhysRevB.75.035333.

[157] D. Breyel and A. Komnik, Phys. Rev. B **84**, 155305 (2011), URL http://link.aps.org/doi/10.1103/PhysRevB.84.155305.

[158] K. Le Hur, Nature **526**, 203 (2015), ISSN 0028-0836, URL http://dx.doi.org/10.1038/526203a.

[159] H.-B. Xue, H.-J. Jiao, J.-Q. Liang, and W.-M. Liu, Scientific Reports **5**, 8978 (2015), URL http://dx.doi.org/10.1038/srep08978.

[160] T. Ando, Phys. Rev. B **44**, 8017 (1991), URL http://link.aps.org/doi/10.1103/PhysRevB.44.8017.

[161] B. Harke, *Herstellung und Untersuchung von Quantenpunktkontakten und Quantenpunkten - Möglichkeiten der AFM-Lithographie* (Leibniz Universität Hannover, 2004).

[162] M. C. Rogge, *Einzel-, Doppel- und Dreifachquantenpunkte im Transport* (Leibniz Universität Hannover, 2008), URL http://edok01.tib.uni-hannover.de/edoks/e01dh09/590526545.pdf.

[163] A. G. Abanov and D. A. Ivanov, Phys. Rev. Lett. **100**, 086602 (2008), URL http://link.aps.org/doi/10.1103/PhysRevLett.100.086602.

[164] A. G. Abanov and D. A. Ivanov, Phys. Rev. B **79**, 205315 (2009), URL http://link.aps.org/doi/10.1103/PhysRevB.79.205315.

[165] F. Hassler, M. V. Suslov, G. M. Graf, M. V. Lebedev, G. B. Lesovik, and G. Blatter, Phys. Rev. B **78**, 165330 (2008), URL http://link.aps.org/doi/10.1103/PhysRevB.78.165330.

[166] C. W. J. Beenakker and H. Schomerus, Phys. Rev. Lett. **93**, 096801 (2004), URL http://link.aps.org/doi/10.1103/PhysRevLett.93.096801.

[167] H. F. Song, C. Flindt, S. Rachel, I. Klich, and K. Le Hur, Phys. Rev. B **83**, 161408 (2011), URL http://link.aps.org/doi/10.1103/PhysRevB.83.161408.

[168] P. Stegmann, B. Sothmann, A. Hucht, and J. König, Phys. Rev. B **92**, 155413 (2015), URL http://link.aps.org/doi/10.1103/PhysRevB.92.155413.

[169] S. Gustavsson, R. Leturcq, B. Simovič, R. Schleser, P. Studerus, T. Ihn, K. Ensslin, D. C. Driscoll, and A. C. Gossard, Phys. Rev. B **74**, 195305 (2006), URL http://link.aps.org/doi/10.1103/PhysRevB.74.195305.

[170] S. M. Cronenwett, S. M. Maurer, S. R. Patel, C. M. Marcus, C. I. Duruöz, and J. S. Harris, Phys. Rev. Lett. **81**, 5904 (1998), URL http://link.aps.org/doi/10.1103/PhysRevLett.81.5904.

[171] K. MacLean, S. Amasha, I. P. Radu, D. M. Zumbühl, M. A. Kastner, M. P. Hanson, and A. C. Gossard, Phys. Rev. Lett. **98**, 036802

(2007), URL http://link.aps.org/doi/10.1103/PhysRevLett.98.036802.

[172] E. B. Foxman, U. Meirav, P. L. McEuen, M. A. Kastner, O. Klein, P. A. Belk, D. M. Abusch, and S. J. Wind, Phys. Rev. B **50**, 14193 (1994), URL http://link.aps.org/doi/10.1103/PhysRevB.50.14193.

[173] P. Stegmann and J. König, ArXiv e-prints (2016), 1605.09258v1, URL https://arxiv.org/pdf/1605.09258v1.pdf.

[174] S. Welack, S. Mukamel, and Y. Yan, EPL (Europhysics Letters) **85**, 57008 (2009), URL http://stacks.iop.org/0295-5075/85/i=5/a=57008.

[175] M. Albert, C. Flindt, and M. Büttiker, Phys. Rev. Lett. **107**, 086805 (2011), URL http://link.aps.org/doi/10.1103/PhysRevLett.107.086805.

[176] M. Albert, G. Haack, C. Flindt, and M. Büttiker, Phys. Rev. Lett. **108**, 186806 (2012), URL http://link.aps.org/doi/10.1103/PhysRevLett.108.186806.

[177] K. H. Thomas and C. Flindt, Phys. Rev. B **87**, 121405 (2013), URL http://link.aps.org/doi/10.1103/PhysRevB.87.121405.

[178] G. Haack, A. Steffens, J. Eisert, and R. Hübener, New Journal of Physics **17**, 113024 (2015), URL http://stacks.iop.org/1367-2630/17/i=11/a=113024.

[179] K. C. Lee, J. Res. Natl. Inst. Stand. Technol. **103**, 177 (1998).

Acknowledgements

The journey through the doctoral study years had been one of the best fulfilling times for me. It had brought in wonderful learning opportunities for me in many areas of human dimensions and it would be impossible for me to become expressively thankful to each aspect that played that essential part in teaching me with many of the nuances that I would always treasure.

I would start with my sincere gratitude to Prof. Dr. Rolf J Haug, my thesis supervisor, for having given me an opportunity to work in his labs, for having been an excellent manager for me with taking care of most needs inside and outside of the labs during my experiment times, for his keen interests to bring in valuable expertise for scientific discussions, for his silent understanding and kind patience for me at times of my decelerated efficiencies during the times of samples continuously not working and the later years, all of which had always been very encouraging for me.

I like to thank Dr. Stephan Pfalz, for his good emotional support as Quest coordinator during the initial years of my doctoral work. I'd learnt the tricks of the trade of carrying out experiments in counting statistics, in the initial years through numerous discussions with the established wisdom of my early senior colleagues Dr. Christian Fricke, Dr. Niels Ubbelohde and, Privat Dozent Dr. Frank Holz, while I'm also thankful to Dr. Maximillian Rogge, Mr. Cay Kalmbach, Mr. Bogdan Popescu and Dr. Daniel Tutuc for all their support with my initial experiences with scanning electron and atomic force microscopes.

The initial discussions with Dr. Christian Flindt and Dr. Dania Kambly were the ones which had sown the seeds for this work and I'm very indebted to these discussions.

Mr. Ronny Heuther and Mr. Manfred Marquardt were the ones I had to lean upon the most for my requirements with electrical and mechanical workshop requirements. Ronny had been the best to offer his skills in many places with many nuanced propositions with activities in the labs and I

deeply appreciate each of his efforts. I'd tremendously appreciated Manfred who had been on the verge of his retirement and could offer me plenty of patience to guide me as slowly as possible in Deutsch while working at the mechanical workshop during the initial years. I appreciate Mr. Joachim Paul to offer me to work unhindered in my initial period to make use of pool of Linux computers and Matlab.

I'd spent lot of time with Dr. Eddy Patrick Rugeramigabo at the MBE and I've always appreciated his pleasantness to work with and, I wish him lots best wishes for his future ventures with MBE again.

Ms. Yvonne Griep had been a wonderful person to discuss many things outside of science and she along with her colleague Ms. Florin Reichers were very wonderful in helping out with administrative needs required of me. Ms. Birgit Ohlendorf who had been associated with Quest school since its inception, has been a wonderful force for many of the students and colleagues and so had been for me with her infallible and pleasant support at all times. Ms. Griep and Ms. Ohlendorf had been wonderful people emotionally in this aspect for me. I would also like to thank Ms. Brigitte Weskamp from the Deans office for being very helpful and kind whenever there was an important administrative need.

For longer part of my years at work, I'd spent time with my good friend and office mate Dr. Alexie Agafonov and I'd the best opportunity to learn lot about European history than any science, with his very good memory at any point of time. Mr. Cay Kalmbach, Ms. Aida Hodaei, Mr. Thomas Jost, Mr. Felix Kraupner, Mr. Nils Schanhorst (for some wonderful photography wanders), Mr. Maxim (for very short time though) were few of the colleagues with who I'd cherished the office space and had good, fun and many purposeful scientific and non-scientific exchanges during the last few years.

I'm thankful to Dr. Lukas Fricke, Dr. Peter Eldridge, Dr. Dave English, Dr. Oliver Geberding, Dr. Joerg Michael Meyer, Dr. Henrik Schmidt, Dr. Hauke Horn, Dr. Thomas Luedke, Dr. Patrick Barthold, Dr. Niels Maire, Dr. Alexander Muehle, Dr. George Mueller, Dr. Stefan Oertel, Dr. Stefannie Dortmann, Dr. Lina Bockhorn, Dr. Monika Kotzian (also for helping with my latex needs), Dr. Fabian Berski (also for proof-reading my thesis work), Dr. Ramin Dahbashi, Dr. Dimitry Smirnov, Dr. Alexander Heine who were few of my past colleagues with who I could spend considerable time in fun,

non-scientific and scientific discussions and with few of who I continue to treasure good friendships.

I appreciate the company of all current colleagues, in particular Mr. Hendrik Kuhn, Mr. Christopher Belke, Mr. Johannes Rode, Mr. Timo Wagner, Mr. Johannes Bayer, Ms. Julia Wiegand, Mr. Michael Beck, Mr. Jan Geritt Lonnemann and Prof. Dr. Michael Oestreich for some of many wonderful moments in the last years, I wish to thank each of them for their support during my stay. I've always enjoyed the company of Dr. Jens Huebner for his pleasantness and good number of short scientific and non-scientific exchanges throughout the years.

I wish to mention Ms. Klara Wernecke who is currently supporting infrastructure management and Mr. Uwe Grothof, Mr. Jens Wiegmann, Mr. Andreas Wittig with the mechanical workshop and I'm thankful for each of their good persona and dependable help that I'd sought during the last many years.

My stay in Hannover would be incomplete without the support of many other good friendships and I wish to thank with lots warmth, Dr. Balasubramanian Ramani for his support and presence whenever I'd needed him, Dr. Kazik Lakomierz, Mr. Dhanesh Ram, Mr. Chandramouli Kannan, Dr. Arun Naini, Mr. Tulasikopan, Ms. Karunya and Dr. Priyanka Parvathi for all their support whenever I'd needed them. I would very much treasure other good friendships at Hannover, for all their invaluable time and emotional support for me. Further, among many old good friendships the ones of Prof. Dr. N. Lawrence, Prof. Dr. I. Johnson, Prof. Dr. John Bosco Balaguru, Prof. Dr. Selvaraj, Prof. Dr. Srinivasamoorthy and Prof. Dr. Werner Bergholz are also few that I would like to mention in the context of research in Physics in here.

The love and support of parents and brother Ravi had carried me over through many of my adventurous rides of life so far and I'm highly indebted to them. I have cherished and would continue to do so, the innocent lovingness of Karthi and Tishya and the ever present honest support, love and all good-givings of Krishna.

Lebenslauf

Name	Nandhavel Sethubalasubramanian
04.1996	All India Senior School Certificate Exam (Class 12)
06.1996 - 04.1999	Bachelor of Science (Physics), Bharatidasan University, India
06.1999 - 04.2001	Master of Science (Physics), Bharatidasan University, India Master thesis: *Detection and sizing of defects using ultrasound and, 2/3 dimensional imaging of defects using a computer*, in collaboration with Welding Research Institute, Trichy, India
09.2004 - 01.2007	Master of Science (Electrical Engineering), Jacobs University, Bremen, Germany Master thesis: *Exploration and design of low power shufflers using data-path generator*, in collaboration with IMEC, Leuven (Belgium) and RWTH, Aachen (Germany)
since 03.2009	Working towards doctoral dissertation Department of Nanostructures, Institut für Festkörperphysik, Leibniz Universität Hannover Supervisor: Prof. Dr. Rolf J. Haug

Publications

- *Factorial cumulants in conditional tunneling regime in a single quantum dot*, in preparation
- *Waiting time distributions in conditional tunneling regime in a single quantum dot*, in preparation

Related work

- *High-order cumulants in the counting statistics of asymmetric quantum dots*, C. Fricke, F. Hohls, N. Sethubalasubramanian, L. Fricke and R. J. Haug, Appl. Phys. Lett., **96**, 202103 (2010)